Unterschrift BetreuerIn

TECHNISCHE UNIVERSITÄT WIEN

DIPLOMARBEIT

Experimental Characterisation of a High-Temperature Heat Pump with Ejector

ausgeführt am Institut für Angewandte Physik
der Technischen Universität Wien
und am
Austrian Institute of Technology GmbH

unter der Anleitung von
Ao.Univ.Prof. Dipl.-Ing. Dr.techn. Martin Gröschl
Priv.-Doz. Dipl.-Ing. Dr.techn. Christoph Reichl
Univ.Lektor Dipl.-Ing. Dr.techn. Michael Lauermann

durch

Leo Stöger

[redacted]

August 27, 2024

Unterschrift StudentIn

TECHNISCHE UNIVERSITÄT WIEN

Ich habe zur Kenntnis genommen, dass ich zur Drucklegung meiner Arbeit unter der Bezeichnung

Diplomarbeit

nur mit Bewilligung der Prüfungskommission berechtigt bin.

Ich erkläre weiters an Eides statt, dass ich meine Diplomarbeit nach den anerkannten Grundsätzen für wissenschaftliche Abhandlungen selbständig ausgeführt habe und alle verwendeten Hilfsmittel, insbesondere die zugrunde gelegte Literatur genannt habe.

Weiters erkläre ich, dass ich dieses Diplomarbeitsthema bisher weder im In- noch Ausland (einer Beurteilerin/einem Beurteiler zur Begutachtung) in irgendeiner Form als Prüfungsarbeit vorgelegt habe und dass diese Arbeit mit der vom Begutachter beurteilten Arbeit übereinstimmt.

Wien, am 27.8.2024 _____

Danksagung

Zuerst gebührt mein Dank Ao.Univ.Prof. Dipl.-Ing. Dr.techn. Martin Gröschl, meinem Betreuer von der *TU Wien*, für seine Unterstützung und Begleitung während dieser Diplomarbeit.

Bedanken möchte ich mich auch bei meinen Eltern, die mir mein Studium ermöglicht und mich immer liebevoll unterstützt haben und bei meiner Schwester Marlene. Ganz besonders "Danke" sagen möchte ich auch meiner wunderbaren Ehefrau Kathi - für alles!

Im Rahmen dieser Diplomarbeit durfte ich die Abteilung für nachhaltige thermische Energiesysteme am Austrian Institute of Technolgy (*AIT*) kennenlernen. Ich habe das freundliche Arbeitsumfeld sehr genossen und möchte mich herzlich bei allen Kolleginnen und Kollegen dafür bedanken, wie warmherzig ich aufgenommen und bei meiner Arbeit unterstützt wurde!

"Danke" sagen möchte auch insbesonders meinem Kollegen Stephan, der mir viel beigebracht hat und mit dem ich Zusammenarbeit sehr genossen habe! Danke auch an Verena, Manuel, Julian und Michi für Eure Unterstützung und die spannenden Gespräche. Danke an Sebastian, Micha und Lorea für die gemütliche Atmosphäre im Büro und beim Mittagessen!

Christopher Illich von *OCHSNER*, der die Wärmepumpe am Prüfstand mit beeindruckender Erfahrung und Souveränität betreut hat und mir gleichzeitig mit Rat und Tat bei der Datenerfassung zur Seite gestanden ist, möchte ich auch ein großes "Dankeschön" für seine Unterstützung aussprechen!

Abschließend möchte ich mich bei Dipl.-Ing. Dr.techn. Christoph Reichl bedanken, der diese Diplomarbeit inhaltlich als mein Betreuer vom *AIT* begleitet hat und der mich auch persönlich wie ein Mentor unterstützt hat und mir bei allen schwierigen Fragen stets zur Seite gestanden ist!

Kurzfassung

Wärmepumpen bieten eine äußerst effiziente und umweltfreundliche Alternative zu fossilen Brennstoffen wie Kohle und Gas, indem sie Umgebungswärme aus Luft, Wasser oder Boden unter minimalem Einsatz von Strom nutzen. Jedoch tritt bei herkömmlichen Expansionsventilen in Wärmepumpen ein irreversibler Verlustprozess auf. Der Ejektor ist ein innovatives Bauteil, das in den Kältekreislauf eingefügt werden kann, um diese Verluste signifikant zu verringern und die Effizienz der Wärmepumpen im Vergleich zu konventionellen Systemen um bis zu 27 % zu steigern.

Üblicherweise ist der Ejektor ein starres Bauteil ohne bewegliche Teile, das aus drei Öffnungen besteht – einer Saugdüse, einer Antriebsdüse und einem Auslass. Der Hochdruckantriebsstrom induziert einen Saugstrom von der Niederdruckseite, was zu einem höheren Druck am Auslass des Ejektors beziehungsweise am Einlass des Verdichters führt und den elektrischen Strombedarf des Verdichters reduziert.

Im Rahmen des Forschungsprojekts "*ETHP – Ejektortechnologie für Wärmepumpen*" wurde eine industrielle Hochtemperaturwärmepumpe mit einem Ejektor entwickelt. Das System wurde für eine Quellentemperatur von etwa 45 °C und eine Senketemperatur von rund 130 °C optimiert, mit einem simulierten Leistungskoeffizienten von 2.04 und einer Heizleistung von etwa 60 kW. Die Wärmepumpe und der Ejektor wurden hergestellt und im Betrieb getestet.

Diese Diplomarbeit beschäftigt sich hauptsächlich mit dem experimentellen Teil des *ETHP*-Projekts, insbesondere mit der Sensorik und dem Messsystem zur Datenerfassung und -analyse. Über 30 Messsensoren wurden in den Kältekreis eingebaut, um Druck-, Temperatur- und Massenstromwerte an verschiedenen Stellen zu ermitteln. Ein Schaltschrank wurde konstruiert, um die Messsensoren mit einem Computer zu verbinden. Die Messdaten wurden sowohl in Echtzeit als auch nachträglich ausgewertet und mit einem besonderen Fokus auf den Einfluss des Ejektors visualisiert.

Während der Messungen traten mehrere Herausforderungen auf, wie ein zu geringer Kältemittelmassenstrom, mangelnde Unterkühlung und hohe Wärmeverluste, die dazu führten, dass der Auslegungspunkt der Wärmepumpe noch nicht erreicht werden konnte. Diese Diplomarbeit liefert konkrete Adaptionsvorschläge für die nächsten Messungen und trägt durch die Analyse der experimentellen Daten zu einem verbesserten Verständnis industrieller Hochtemperaturwärmepumpen mit Ejektoren bei.

Abstract

Heat pumps offer a highly efficient and environmentally-friendly alternative to fossil fuels like coal and gas by utilising ambient heat from air, water or ground with minimal use of electricity. However, in the expansion valves used in traditional heat pumps an irreversible dissipation process occurs. An innovative component inserted into the refrigeration circuit, the ejector, has the potential to decrease these losses significantly and improve the Coefficient of Performance of heat pumps by up to 27 % in comparison to conventional systems.

An ejector normally is a passive component without moving parts that consists of three openings – a suction nozzle, a motive nozzle and an outlet. The high-pressure motive flow induces a suction flow from the low-pressure side, resulting in a higher pressure at the compressor inlet. This process reduces the electrical power required for compressor operation.

Within the research project "*ETHP – Ejector Technology for Heat Pumps*", an industrial high-temperature heat pump featuring an ejector was designed. The system was optimised for a source temperature of approximately 45 °C and a sink temperature of around 130 °C with a simulated Coefficient of Performance of 2.04 and a heating capacity of about 60 kW. The heat pump and the ejector were manufactured and put into operation.

This diploma thesis mostly deals with the experimental part of the *ETHP* project, primarily focusing on the sensor technology and the measurement system for data acquisition and data analysis. Over 30 measurement sensors were installed to gather data on pressure, temperature gradients, and refrigerant mass flow at various points within the refrigerant circuit. An electrical cabinet was designed to connect the measurement sensors to a computer. The collected data were analysed and visualised in real-time and during post-processing, focusing particularly on the impact of the ejector.

Several challenges were encountered during the measurements, such as insufficient mass flow, a lack of subcooling, and high heat losses, which led to the design conditions of the heat pump not yet being reached. This diploma thesis provides crucial suggestions for improvements for the next measurements and contributes to an enhanced understanding of industrial high-temperature heat pumps with ejectors through the analysis of experimental data.

Nomenclature

Abbreviations

3WV	Three-Way Valve	
AIT	Austrian Institute of Technology	
Comp.	Compressor	
Cond.	Condenser	
const.	Constant	
COP	Coefficient of Performance	1
corr.	Corresponding to	
Eq.	Equation	
ETHP	Ejector Technology for Heat Pumps (FFG Project)	
FFG	Austrian Research Promotion Agency	
Fig.	Figure	
HP	High-Pressure Side	
IHX	Internal Heat Exchanger	
LP	Low-Pressure Side	
OCH	OCHSNER Energietechnik GmbH	
Sep.	Separator	

Greek Symbols

Δ	Delta	
ϵ	Emissivity	1
η	(Ejector) Efficiency	1
κ	Adiabatic Coefficient	1
Π_s	Suction Pressure Ratio	1
ψ	Entrainment Ratio	1
ρ	Density	$\mathrm{kg\,m^{-3}}$

Latin Symbols

$\dot{m}$, F	Mass Flow Rate	$\mathrm{kg\,s^{-1}}$
$\dot{Q}$	Heat Flow Rate	W
$\dot{V}$	Volume Flow Rate	$m^3\,s^{-1}$
A	Area	$\mathrm{m^2}$
C_p	Specific Heat Capacity at Constant Pressure	$\mathrm{J\,kg^{-1}}\,K^{-1}$
C_v	Specific Heat Capacity at Constant Volume	$\mathrm{J\,kg^{-1}}\,K^{-1}$
h	Specific Enthalpy	$\mathrm{J\,kg^{-1}}$
h_t	Heat Transfer Coefficient	$\mathrm{W\,m^{-2}}\,K^{-1}$
L	Length	m
m	Mass	kg
n	Amount of Substance	mol
p, P	Pressure	Pa or bar
Q	Heat	J or Wh
r	Radius	m
S	Entropy	$\mathrm{J\,K^{-1}}$
T	Temperature	K
U	Internal Energy	J
V	Volume	$\mathrm{m^3}$
v	Velocity	$\mathrm{m\,s^{-1}}$
W	Work	J or Wh
z	Height	m
E	Energy	J
s	Current	mA
x	Vapour Quality	1

Subscripts

cal	Calibrated
comp	Compressor
con	Condenser
conv	Convection
el	Electrical
eva	Evaporator
in	Inflow
max	Maximum
meas	Measurement
min	Minimum
mot	Motive
oil	Oil
out	Outflow
rad	Radiation
rec	Recovered
refr	Refrigerant
rel	Relative
suc	Suction
tot	Total
water	Water

Contents

1 Introduction

In 2020, the European Commission adopted a legislative proposal for a European climate law that aims to achieve net-zero greenhouse gas emissions by 2050, with the objective of making Europe the first climate-neutral continent (Erbach, 2021).

More than a fourth of the energy consumption in the EU was required by the manufacturing industry in 2020 (Bundesministerium für Klimaschutz, 2022). In industrial processes, substantial amounts of waste heat are generated and often discarded rather than energetically utilised. Using heat pumps to elevate the temperature of this waste heat to a usable level for further processes can make a significant contribution to reducing fossil fuel consumption, energy consumption in general and CO_2 emissions (Rieberer et al., 2015).

Throttling devices like expansion valves, which expand the refrigerant in heat pumps from a higher condensing pressure to a lower evaporation pressure, lead to irreversible energy dissipation. By harnessing the kinetic energy released during the pressure reduction as the fluid moves from the high-pressure to the low-pressure side, the electric power consumption of the compressor can be lowered and thus the efficiency of the heat pump increased (Elbel and Lawrence, 2016).

This can be achieved by inserting a component called ejector, which was first patented by Gay in 1931, into the refrigerant circuit (Gay, 1931). High-pressure refrigerant enters the motive nozzle of the ejector and is converted into a high-velocity jet. This creates a low-pressure zone, where refrigerant from the suction nozzle is drawn into the ejector and mixes with the motive flow. This mixture is then slowed down in a diffuser, converting the kinetic energy back into pressure energy for discharge at an intermediate pressure level (Besagni et al., 2016).

For instance, Nakagawa et al. (2011) found that a CO_2 refrigeration system with an ejector and an internal heat exchanger (IHX) lead to improvements of the Coefficient of Performance (COP) of up to 27% in comparison to similar conventional systems (Nakagawa et al., 2011).

The research project *ETHP* (Ejector Technology for Heat Pumps) aims to pave the way towards a decarbonised world by establishing ejector technology for high and very high-temperature heat pumps (ETHP, 2022). The project is sponsored by the Austrian Research Promotion Agency (*FFG*) and is primarily carried out by the Austrian Institute of Technology (*AIT*) and OCHSNER Energietechnik GmbH (*OCH*).

Within the *ETHP* project, various ejector geometries were simulated and compared until an optimal ejector design with a variable inner geometry was identified. Then,

a refrigerant circuit featuring the ejector was planned and optimized. A prototype of this industrial high-temperature ejector heat pump with the refrigerant R1233zd(e)[1] was manufactured and put into operation.

While the *ETHP* project commenced in January 2022 and is planned to continue at least until the end of 2024, this diploma thesis focuses on the experimental part of the project, that took place between mid of November 2023 to mid of July 2024.

Within this time span, the measurement system for data acquisition was set up and the first measurements were carried out on the prototype of the heat pump. Finally, due to challenges and difficulties encountered during these measurements, an intensive search for sources of errors was conducted using the acquired measurement data to identify solutions for improvement in the next measurement campaign.

After this introduction, the next chapter (Chapter 2) briefly discusses the principles of thermodynamics and provides an overview of the basics regarding heat pump and ejector technology. In Chapter 3, the experimental setup is introduced, including the design of the refrigerant circuit, the measurement system and the control cabinet, as well as the methodology for real-time visualisation of the measurement data using *LabVIEW*.

Chapter 4 highlights important experimental results from the first measurement campaign. A comparison between the simulated design point of the heat pump and the measured operating points is presented in Chapter 5. Finally, Chapter 6 summarises the results and analyses how the operation of the heat pump could be improved for the next measurement period both through mechanical modifications to the heat pump and improvements regarding specific control parameters of heat pump and test rig.

[1] R1233zd(e) is a refrigerant with a low global warming potential and a high energy efficiency, commonly used in refrigeration and air conditioning systems as a replacement for ozone-depleting substances (Arpagaus and Bertsch, 2020).

2 Theoretical Background

In this chapter, the theoretical background is discussed, starting with fundamental thermodynamic principles, including state variables, changes of state, the laws of thermodynamics, and thermodynamic cycles. The operating principle of a heat pump is explained, detailing the structure and function of a heat pump and giving a brief comparison to high-temperature heat pumps. Finally, the operating principle of an ejector is explored, including its structure, mechanism, global parameters, and how the ejector can be integrated into a heat pump system.

2.1 Thermodynamic Principles

This section gives a brief theoretical introduction to the field of thermodynamics and is conceptually based on the books *Experimentalphysik 1: Mechanik und Wärme* (Demtröder, 2015) and *Thermodynamik: Grundlagen und technische Anwendungen Band 1: Einstoffsysteme* (Stephan et al., 2013).

2.1.1 State Variables and Changes of State

A state variable is a physical quantity that describes the current state of a thermodynamic system. It is independent of the way in which this state was reached. Examples for state variables are the volume V, the pressure p, the temperature T as well as the total energy E in the system, the entropy S or the enthalpy H (Demtröder, 2015).

State Variables that do not depend on the size of the system, like p or T, are called intensive, while extensive state variables, like V or E, increase proportionally to the system size. Therefore, intensive variables provide information about the intrinsic state of the system, while extensive variables reflect the overall size or amount of material present in the system (Stephan et al., 2013).

Thermodynamic processes, characterised by changes in state variables, exhibit specific conditions:

- Isothermal changes of state occur when a system undergoes changes while maintaining a constant temperature, allowing for the exchange of heat with its surroundings (Demtröder, 2015).

- Isobaric processes involve changes at a constant pressure (Demtröder, 2015).

- Isochoric changes of state occur at a constant volume (Demtröder, 2015).
- Isenthalp and isentropic processes are characterised by the enthalpy or the entropy of the system remaining constant (Stephan et al., 2013).
- In adiabatic processes no heat transfer to or from the system occurs (Demtröder, 2015).

2.1.2 The Laws of Thermodynamics

The fundamental principles of thermodynamics, known as the laws of thermodynamics, are empirical observations that cannot be mathematically proven but are derived from extensive experimental evidence (Demtröder, 2015).

The **Zeroth Law of Thermodynamics** states that if two systems are each in thermal equilibrium with a third system, then they are also in thermal equilibrium with each other (Stephan et al., 2013).

The **First Law of Thermodynamics** is equal to the law of energy conservation. Energy cannot be created or destroyed in an isolated system (Stephan et al., 2013). Mathematically, this can be expressed as shown in Eq. 1: The sum of the heat energy supplied to a system ΔQ from outside and the work supplied ΔW is equal to the increase in the system's internal energy ΔU (Demtröder, 2015).

$$\Delta U = \Delta Q + \Delta W \tag{1}$$

The arrow of time is dictated by the **Second Law of Thermodynamics**, which states that natural processes proceed towards increasing entropy. The total entropy S of an isolated system always increases over time, or at best remains constant, in any spontaneous process (see Eq. 2). For a reversible process, the equality holds, whereas in an irreversible process, entropy increases (Stephan et al., 2013).

$$\Delta S \geq 0 \tag{2}$$

An alternative formulation of the Second Law of Thermodynamics is that heat naturally flows only from a warmer body to a colder one, never in the opposite direction (Demtröder, 2015).

For completeness, the Nernst heat theorem (see Eq. 3), also known as the **Third Law of Thermodynamics**, states that the entropy (of a pure, perfect crystalline substance) approaches zero as the temperature approaches absolute zero (Stephan et al., 2013).

$$\lim_{T \to 0\,\mathrm{K}} S = 0 \tag{3}$$

2.1.3 Thermodynamic Cycles

In cyclic processes, a working fluid is continuously circulated within a machine, exchanging heat and work with the environment (Grassi, 2018). Three types of thermodynamic cycles are distinguished depending on their purpose:

- In a **heat engine**, the desired output is work. To generate this work, heat is supplied from a heat source at a higher temperature and discharged to a heat sink at a lower temperature (Grassi, 2018).

- In the case of a **heat pump**, heat is extracted from the heat source at a lower temperature and delivered to the heat sink at a higher temperature, further cooling the source and heating up the sink. To achieve this, work is required as input to the system (Demtröder, 2015).

- In **refrigerators**, a process very similar to a heat pump occurs, but instead of heating up the sink the goal is to cool down the source (Stephan et al., 2013).

In 1824, Sadi Carnot formulated a theoretical, reversible thermodynamic cycle, the Carnot cycle, in which an ideal gas undergoes two isothermal and two adiabatic processes through expansion and subsequent compression, ultimately returning to its initial state (see Fig. 1). This cycle defines the maximum possible efficiency of a heat engine (Demtröder, 2015).

1. **Isothermal expansion**

   At a constant temperature T_1 ($\Delta U_1 = 0$), an expansion from V_1 to V_2 occurs as the system receives the heat quantity ΔQ_1 from a heat reservoir. The work done by the gas during its volume change is given by $dW = -pdV$ ($\Delta W_1 < 0, \Delta Q_1 > 0$). Using the ideal gas law ($p = \frac{n\,\mathrm{R}\,T}{V}$[2]) and the First Law of Thermodynamics (see Eq. 1), we obtain Eq. 4 (Demtröder, 2015).

[2] R is the universal gas constant with a value of $8.314\,\mathrm{J/(mol\,K)}$.

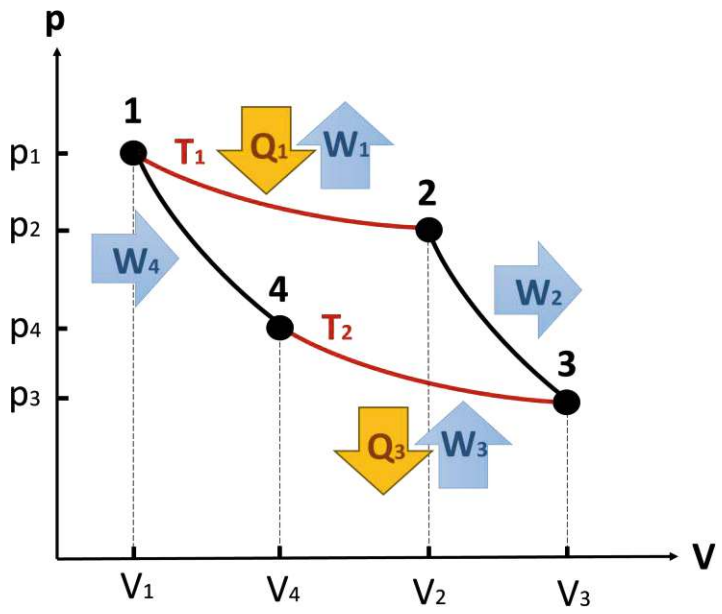

Figure 1: The Carnot cycle consists of four steps: 1→2 isothermal expansion, 2→3 adiabatic expansion, 3→4 isothermal compression and 4→1 adiabatic compression. (Created by the author based on Demtröder (2015).)

$$\Delta Q_1 = -\Delta W_1 = \int_{V_1}^{V_2} p dV = \int_{V_1}^{V_2} \frac{n\,\mathrm{R}\,T_1}{V} dV = n\,\mathrm{R}\,T_1\,ln(\frac{V_2}{V_1}) \tag{4}$$

2. **Adiabatic expansion**

Next, the gas expands adiabatically ($\Delta Q = 0$) from volume V_2 to V_3 to the temperature T_2 (with $T_2 < T_1$). The gas performs work on its surrounding through the expansion ($\Delta W_2 < 0, \Delta U_2 < 0$). Eq. 5 also introduces the adiabatic index κ, which is defined as the ratio of the specific heats at constant pressure C_p to constant volume C_V (Demtröder, 2015).

$$\begin{gathered} \Delta Q_2 = 0 \rightarrow \Delta U_2 = \Delta W_2 = U(T_2) - U(T_1) \\ T_1\,V_2^{\kappa-1} = T_2\,V_3^{\kappa-1} \end{gathered} \tag{5}$$

3. **Isothermal compression**

   Isothermally (at temperature T_2), the gas is compressed from V_3 to V_4, releasing the heat ΔQ_3 ($\Delta W_3 > 0, \Delta Q_3 < 0$) (Demtröder, 2015).

$$\Delta Q_3 = -\Delta W_3 = \int_{V_3}^{V_4} p dV = \int_{V_3}^{V_4} \frac{n\,\mathrm{R}\,T_2}{V} dV = n\,\mathrm{R}\,T_2\,ln(\frac{V_4}{V_3}) \tag{6}$$

4. **Adiabatic compression**

   As a final step, an adiabatic compression ($\Delta Q_4 = 0$) decreases the volume from V_4 to V_1 and increases the temperature from T_2 to T_1 ($\Delta W_4 > 0, \Delta U_4 > 0$) so that the gas is again in its initial state and the cycle can be repeated (Demtröder, 2015).

$$\begin{gathered} \Delta Q_4 = 0 \rightarrow \Delta U_4 = \Delta W_4 = U(T_1) - U(T_2) = -\Delta W_2 \\ T_1\,V_1^{\kappa-1} = T_2\,V_4^{\kappa-1} \end{gathered} \tag{7}$$

The work input into the system in the fourth step equals the work done by the system in the second step ($\Delta W_2 = -\Delta W_4$). Therefore, the net amount of work ΔW_{tot} only stems from the isothermal steps (see Eq. 8) (Demtröder, 2015).

$$\Delta W_{tot} = \Delta W_1 + \Delta W_3 = n\,\mathrm{R}\,(T_1\,ln(\frac{V_1}{V_2}) + T_2\,ln(\frac{V_3}{V_4})) \tag{8}$$

By dividing the relation of volumes and temperatures during the adiabatic processes, another relation can be established (see Eq. 9) (Demtröder, 2015).

$$\begin{gathered} \frac{V_2}{V_1} = \frac{V_3}{V_4} \rightarrow ln(\frac{V_1}{V_2}) = -ln(\frac{V_3}{V_4}) \\ \rightarrow \Delta W_{\mathrm{tot}} = n\,\mathrm{R}\,ln(\frac{V_2}{V_1})\,(T_2 - T_1) \end{gathered} \tag{9}$$

The efficiency of the Carnot cycle η is expressed as the absolute amount of the work performed ($\Delta W_{\mathrm{tot}} < 0$) divided by the heat energy absorbed during the first step (see Eq. 10) (Demtröder, 2015).

$$\eta = |\frac{\Delta W_{\text{tot}}}{\Delta Q_1}| = \frac{n\,\mathrm{R}\,ln(\frac{V_2}{V_1})\,(T_1 - T_2)}{n\,\mathrm{R}\,ln(\frac{V_2}{V_1})\,T_1} = \frac{T_1 - T_2}{T_1} \tag{10}$$

To conclude, during the Carnot cycle only the fraction $\eta < 1$ of the absorbed heat energy can be converted into work (exergy), while the fraction $1-\eta$ is released as heat to a lower temperature reservoir (anergy). In fact, there is no periodically operating heat engine with an efficiency higher than that of the Carnot cycle (Demtröder, 2015).

2.2 Operating Principle of a Heat Pump

If the Carnot cycle is operated in the other direction, it represents the idealised case of a heat pump or a refrigerator. Using the work ΔW_{tot}, the heat ΔQ_3 is absorbed from the colder reservoir at T_2 and ΔQ_1 is emitted to the warmer reservoir at T_1 (Demtröder, 2015).

The efficiency of a heat pump or refrigerator is called COP and calculated depending on whether the desired output is heating the warmer reservoir (heat pump) or cooling the colder reservoir (refrigerator). For a heat pump, the COP (or COPh) therefore is the ratio of heat output to the work input[3]. In comparison, for refrigerators the COP is calculated by dividing the amount of heat absorbed from the colder reservoir by the work input (Grassi, 2018).

2.2.1 Structure and Function

The colder reservoir, from which heat is extracted, is referred to as the heat source, while the warmer reservoir, to which heat is delivered, is known as the heat sink (Grassi, 2018).

A compression heat pump typically consists of four main components between which the refrigerant circulates, alternately evaporating and condensing (see Fig. 2):

- $A \rightarrow B$**:** Gaseous refrigerant enters the **compressor**. Using the electrical energy W_{in}, the compressor raises the refrigerants pressure and temperature, which also increases its condensing temperature (Demtröder, 2015).

- $B \rightarrow C$**:** In the **condenser**, which is a heat exchanger that is in thermal contact with both the refrigerant and the heat sink, the refrigerant condenses. Thereby

[3] In the case of the Carnot cycle, this leads to $\text{COPh} = |\frac{\Delta Q_1}{\Delta W_{\text{tot}}}| = \frac{T_1}{T_1 - T_2} = \frac{1}{\eta} > 1$ (Demtröder, 2015).

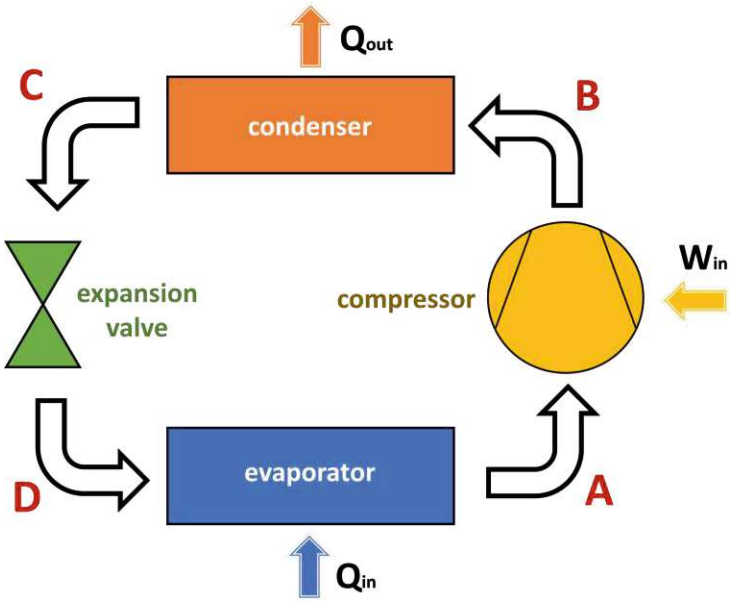

Figure 2: Refrigeration circuit of a traditional compression heat pump consisting of a compressor, a condenser, an expansion valve and an evaporator. (Created by the author based on Demtröder (2015).)

it releases heat, which is transferred to the sink, increasing the sink's temperature. (Grassi, 2018).

- $C \rightarrow D$**:** The **expansion valve** irreversibly lowers the pressure of the refrigerant, thus decreasing its evaporating temperature (Grassi, 2018).

- $D \rightarrow A$**:** The **evaporator** causes the refrigerant to evaporate by retrieving the heat energy Q_{in} from the source and supplying it to the refrigerant (Demtröder, 2015).

The phase changes of the refrigerant during the refrigerant cycle of a compression heat pump can be visualised using a pressure enthalpy diagram (see Fig. 3). Within the saturation curve, the refrigerant exists in a two-phase state. To the left of this curve, the refrigerant is in the liquid state only, while to the right, only gaseous refrigerant is present (Grassi, 2018).

The temperature difference between the actual temperature at the inlet of the compressor and the saturation temperature that corresponds to the pressure of the refrigerant upstream of the compressor is called "suction gas superheating" (see Fig. 3). It ensures that the refrigerant entering the compressor is fully vaporised, preventing damage to the

compressor (Arpagaus, 2017).

The term "hot gas superheating" describes the temperature difference between the condensing temperature and the temperature at the compressor outlet. The temperature difference between the condensing temperature and the temperature at the outlet of the condenser is called "subcooling" (Arpagaus, 2017). Additional subcooling prior to expansion near the evaporation temperature results in a lower vapour content downstream of the expansion valve. This reduces the irreversibility during the expansion and, thus, increases the efficiency of the refrigeration cycle (Rieberer et al., 2015).

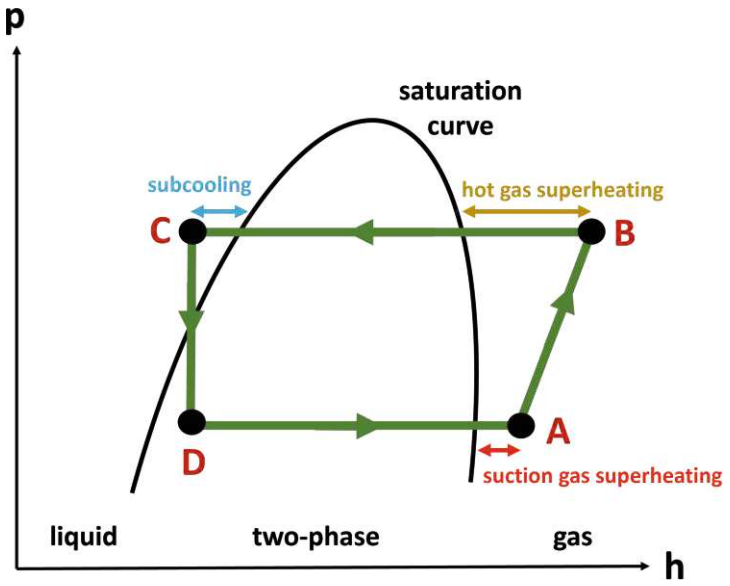

Figure 3: Pressure enthalpy diagram of a traditional heat pump: $A \rightarrow B$ compression, $B \rightarrow C$ condensation, $C \rightarrow D$ expansion and $D \rightarrow A$ evaporation. The saturation curve provides insight into whether the refrigerant is in a liquid, gaseous or two-phase state. (Created by the author based on Grassi (2018).)

2.2.2 Types of Heat Pumps

Heat pumps are well-established in the building sector and, with the advent of new materials and refrigerants, are also becoming increasingly common in industrial applications. Depending on the heat source (air, water or ground) and sink (air or water), different types of heat pumps can be distinguished as shown in Table 1 (Grassi, 2018). In the case of air-water heat pumps, for instance, energy is extracted from outdoor or waste air in order to heat up water. In residential applications, this can be achieved either using a

split system, which consists of a separate outdoor and an indoor unit connected through pipes, or a compact system (Chlubny, 2004).

Table 1: Types of heat pumps depending on heat source and sink (Grassi, 2018).

Heat source	**Heat sink**	**Heat pump type name**
Air	Air	Air-Air
Air	Water	Air-Water
Water	Air	Water-Air
Water	Water	Water-Water
Ground	Water	Geothermal

Geothermal heat pumps extract thermal energy from the ground. With increasing depth below the surface, both the daily and annual variations of the ground temperature decrease strongly in comparison to the ambient air temperature range (Self et al., 2013). Below 10 m, ground temperatures are relatively constant, despite various meteorological factors (like incoming solar radiation, snow cover, air temperature, precipitation and thermal properties of the soil) affecting the surface temperature (Hanova and Dowlatabadi, 2007).

Geothermal heat exchangers can be installed vertically (borehole) or horizontally. Boreholes typically consist of a U-shaped tube through which the heat transfer fluid circulates. It is installed inside a vertical well with a diameter of approximately 20 cm to 30 cm and depths ranging from 80 m to 200 m. The horizontal systems consist of a network of pipes buried at depths between 70 cm and 200 cm, with the size of the covered area strongly depending on the required heating or cooling capacity (Grassi, 2018). Earth baskets can provide an intermediate solution (Kling et al., 2022).

2.2.3 Comparison to High-Temperature Heat Pumps

Rieberer et al. (2015) frequently discuss high-temperature heat pumps in the context of industrial applications, which typically aim at harnessing waste heat for internal process heat supply. This is due to the fact that sink and source temperature levels are considerably higher in industrial settings in comparison to residential purposes (Arpagaus, 2017).

Although the terminology regarding the temperature level of high-temperature heat pumps is inconsistent in literature, it often refers to heat pumps that generate heat in the range from 60 °C to 100 °C (Reißner, 2015). Above 100 °C, the term "very high-temperature heat pump" can be used (Bobelin et al., 2012). Although the heat pump addressed in this thesis is designed to operate with a sink temperature above 100 °C, it is still referred to as high-temperature heat pump to be consistent with the established

nomenclature of this research project.

The utilisation of waste heat helps to both save energy, which enhances the efficiency of industrial processes, and reduce CO_2 emissions (Bobelin et al., 2012). High-temperature heat pumps find application in various industrial sectors such as the paper industry, industrial drying processes, the metal industry, automotive manufacturing, and the food, feed, and plastics industries (Arpagaus, 2017).

For instance, industrial waste heat can be used for process steam generation in the paper industry. Thus, per ton of paper, $3\,m^3$ of heated water at $60\,°C$ (heat source) are used to produce low-pressure steam at $130\,°C$ (heat sink) with a COP of 2.6. Per ton of paper, this leads to a reduction of costs by 40 cents (43 %) and CO_2 emissions by 2 kg (21 %) (Fleckl et al., 2015).

2.3 Operating Principle of an Ejector

The physical process that occurs in the expansion valve of a heat pump causes irreversible energy dissipation. Inserting an ejector into the refrigerant circuit can help to instead utilise the kinetic energy of the refrigerant released during the pressure drop, thus increasing the efficiency of the heat pump (Elbel and Lawrence, 2016).

2.3.1 Structure and Mechanism

An ejector is a static component that consists of a motive nozzle, a suction nozzle and an outlet (see Fig. 4a). Refrigerant enters the ejector through motive and suction nozzle, comes together in the mixing zone and leaves the ejector at the outlet downstream of the diffuser (Schröder, 2020).

A better understanding of the working principle of an ejector is provided by the Bernoulli equation[4] (see Eq. 11), which states that along a streamline of steady flow of an incompressible, inviscid (no friction) fluid the sum of the piezometric pressure $p + \rho\, g\, z$ and the kinetic pressure $\frac{\rho\, v^2}{2}$ is constant (Crowe et al., 2009).

$$p + \rho\, \mathrm{g}\, z + \frac{\rho\, v^2}{2} = \text{const.} \tag{11}$$

[4]When flow velocities are negligible ($v = 0$), the Bernoulli equation simplifies to the hydrostatic equation $p + \rho\, \mathrm{g}\, z = \text{const.}$, with pressure p, density ρ, the gravitational constant $\mathrm{g} = 9.81\,\mathrm{m/s^2}$, and elevation z (Crowe et al., 2009).

Considering a pipe at a constant height ($\Delta z = 0$) through which an ideal liquid flows, Bernoulli's equation implies that at a wider section, where the fluid moves slower due to the conservation of mass flow, the pressure of the fluid increases. In contrast, at a narrower section where the fluid speeds up the pressure drops, as any gain in velocity is accompanied by a corresponding loss of pressure (Faulkner and Ytreberg, 2011).

In the ejector discussed in this thesis, high-pressure liquid refrigerant enters the motive nozzle (1) (see Fig. 4b and 4c). Then, a converging-diverging section (*Laval*-nozzle[5]) causes the refrigerant's velocity to increase to supersonic speeds and the pressure to decrease, according to Bernoulli's equation (Besagni et al., 2016).

The low pressure in the mixing zone (3) draws the gaseous low-pressure refrigerant from the suction nozzle (2) into the ejector, where it mixes with the motive flow. Along the widening cross-section of the diffuser (5), the speed of the two-phase mixture then decreases, thus increasing the pressure at the outlet of the ejector (6) (Besagni et al., 2016).

Simulation results of the Mach number, which is a dimensionless measure of the speed of the refrigerant relative to the speed of sound in the surrounding medium, as well as the vapour quality along the axis of the ejector are shown in Fig. 5. At the diverging part of the Laval-nozzle, the fluid reaches supersonic conditions (Schieder, 2023).

Although an ejector normally is a component without any moving parts, the ejector discussed in this thesis was designed with a bypass (4), which can be opened to provide relief at high mass flow rates. The purple arrows in Fig. 4b and 4c visualise the bypass and how a portion of the suction flow can be diverted so that it only mixes with the motive flow at the end of the mixing zone. The bypass should only be operated in either the fully closed or fully opened position.

[5]In a supersonic flow, unlike in the subsonic range, when the cross-sectional area increases, the pressure decreases and the velocity increases. Therefore, to enable the continuous acceleration from subsonic to supersonic speeds, the flow tube must first contract and then expand after passing through the sonic point (Oertel, 2012).

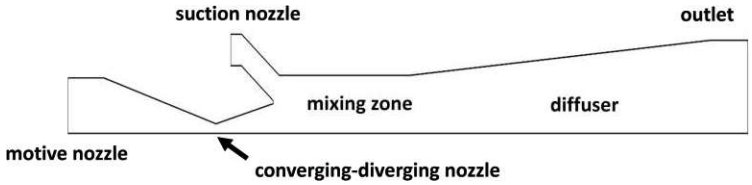

(a) Simplified schematic

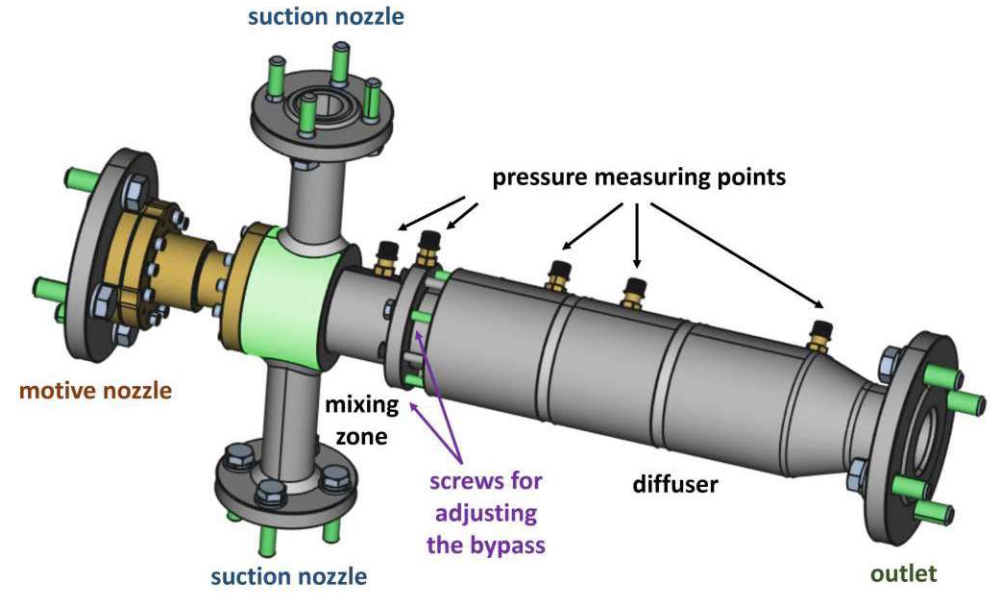

(b) External view

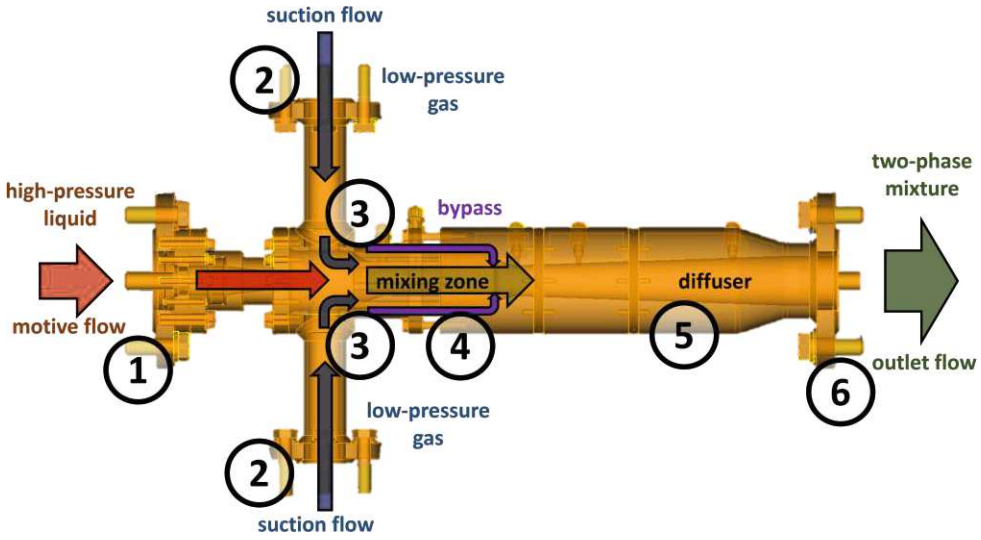

(c) Internal view

Figure 4: The high-pressure motive flow entrains the lower-pressure suction flow, mixing them to create a combined flow at an intermediate pressure level. (Created by the author based on the ejector design from *AIT*.)

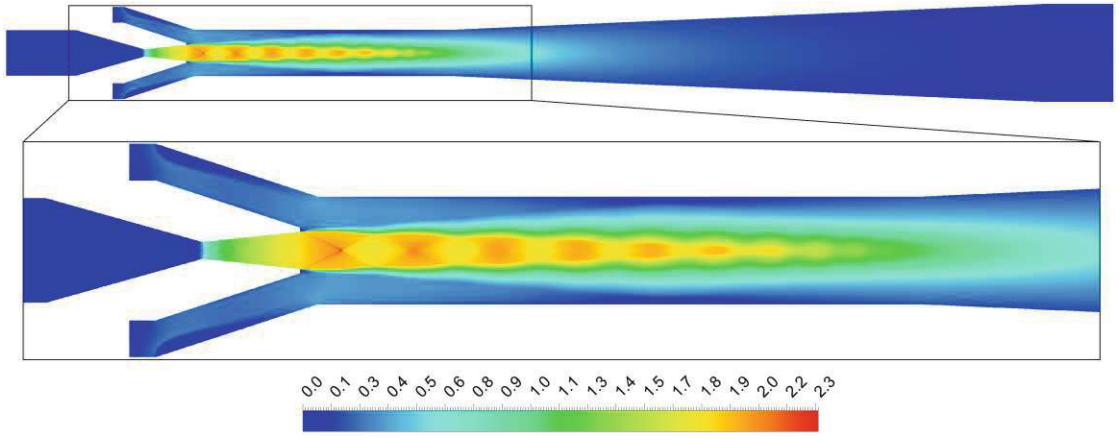

(a) Mach number

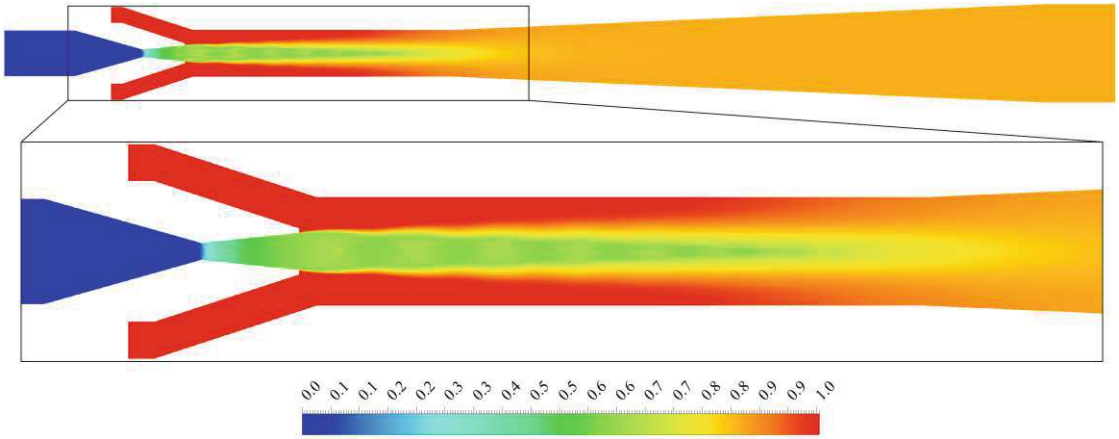

(b) Vapour quality

Figure 5: Simulated contour plots of the Mach number and the vapour quality of the refrigerant along the axis of the ejector. In the converging-diverging nozzle, the liquid refrigerant reached sonic conditions and partly evaporates. (Created by Schieder (2023).)

2.3.2 Global Ejector Parameters

The performance of an ejector can be described using two parameters. The mass entrainment ratio ψ is defined as the ratio of suction mass flow rate to motive mass flow rate[6], indicating the ejector's ability to carry along mass (see Eq. 12). The suction pressure ratio Π_s measures the pressure lift capability of the ejector and is given by the ratio of ejector's outlet pressure to the pressure at the suction nozzle (see Eq. 13) (Elbel and Lawrence, 2016).

$$\psi = \frac{\dot{m}_{\text{suc}}}{\dot{m}_{\text{mot}}} \tag{12}$$

$$\Pi_s = \frac{p_{\text{out}}}{p_{\text{suc}}} \tag{13}$$

A different method quantifies an ejector's performance using only a single parameter, the ejector efficiency, by comparing the amount of expansion work rate recovered by the ejector with the maximum possible expansion work rate recovery potential (see Eq. 14) (Elbel and Hrnjak, 2008).

$$\eta = \frac{\dot{W}_{\text{rec}}}{\dot{W}_{\text{rec,max}}} = \psi \frac{h(p_{\text{out}}, S_{\text{suc}}) - h(p_{\text{suc}}, S_{\text{suc}})}{h(p_{\text{mot}}, S_{\text{mot}}) - h(p_{\text{out}}, S_{\text{mot}})} \tag{14}$$

2.3.3 Integration of the Ejector in Heat Pump Systems

Fig. 6 shows a simplified schematic of how the ejector is integrated into the refrigerant circuit of the heat pump discussed in this thesis. Ejector and separator divide the refrigeration cycle into the condensing and the evaporating circuit.

Liquid high-pressure motive flow from the condenser (**C**) causes the gaseous low-pressure suction flow from the evaporator (**G**) to be sucked into the ejector. The two-phase mixture is separated in the separator (**D**) and the gaseous part (**A**) enters the compressor (**B**) while the liquid part (**E**) is expanded in the expansion valve (**F**).

In the pressure enthalpy diagram in Fig. 7, the pressure lift performed by the ejector is visible. Because of the higher pressure at the compressor inlet, less electrical power is needed to compress the refrigerant to the condensing pressure.

[6]The motive mass flow rate $\dot{m}_{\text{mot}}$ is equal to the mass flow rate in the condensing circuit $\dot{m}_{\text{con}}$, while the suction mass flow rate $\dot{m}_{\text{suc}}$ corresponds to the mass flow rate in the evaporating circuit $\dot{m}_{\text{eva}}$.

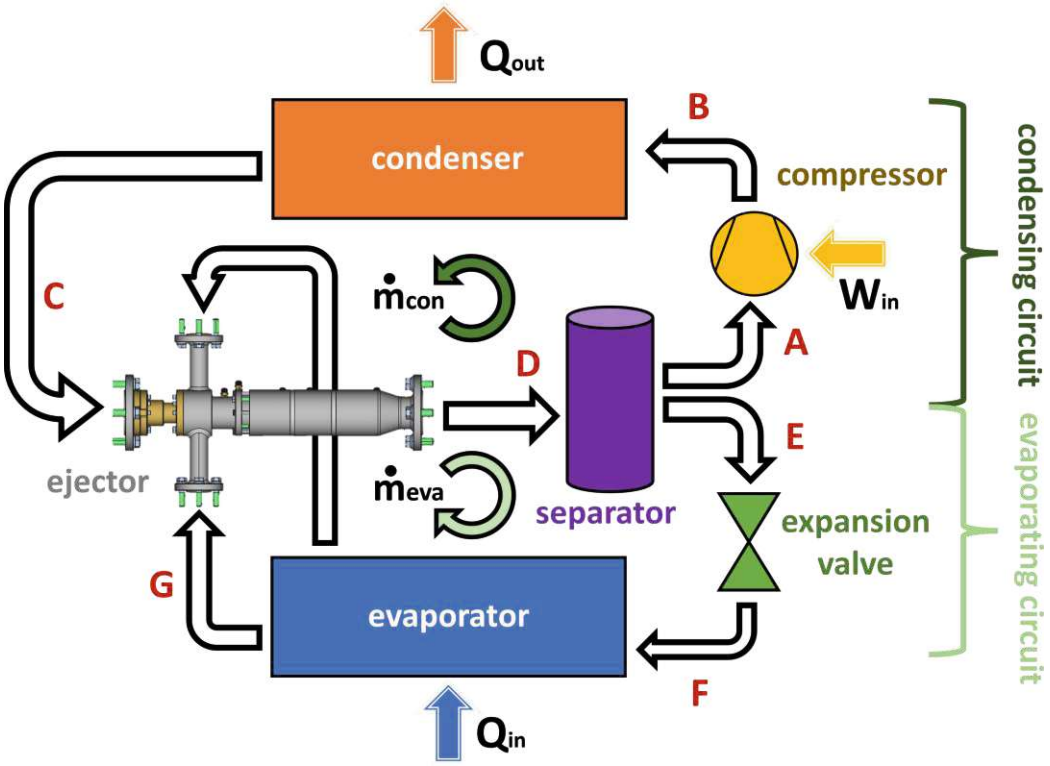

Figure 6: Integration of the ejector into the refrigerant circuit. (Created by the author based on the heat pump design planned by the *ETHP* research group.)

The ejector discussed in this diploma thesis, was designed by Schieder (2023) using numerical fluid dynamics. During the simulations, it was discovered that slight variations in operating conditions and internal geometry significantly impact the ejector's performance, which necessitates the validation of the simulation results via experiments (Schieder, 2023).

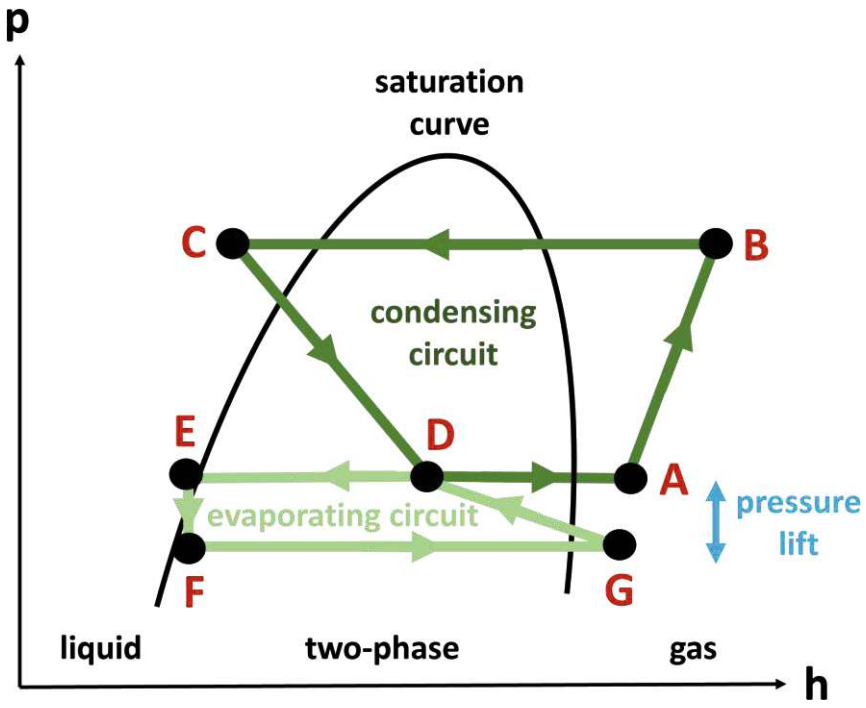

Figure 7: Pressure enthalpy diagram of a simplified ejector heat pump: $A \rightarrow B$ compression, $B \rightarrow C$ condensation, $C \rightarrow D$ ejector motive flow, $D \rightarrow E$ separation (liquid), $E \rightarrow F$ expansion, $F \rightarrow G$ evaporation, $G \rightarrow D$ ejector suction flow and $D \rightarrow A$ separation (gaseous). (Created by the author based on the simulation results of the *ETHP* research group.)

3 Experimental Setup

This chapter first describes the design of the heat pump. Then, the *AIT* measurement system is introduced, as well as the sensors used to acquire the measurement data and the method of data acquisition utilising *ICP DAS* data modules housed in a control cabinet.

After a detailed examination of the refrigeration cycle of the heat pump and a brief overview regarding the test rig for controlling the heat pump, real-time visualisation of the data using *LabVIEW* is discussed, followed by a description of the data analysis methodology for post-processing facilitated through *Jupyter Notebooks*.

3.1 Design of the Heat Pump

The prototype of an industrial high-temperature ejector heat pump this diploma thesis focuses on was assembled by *OCH* in St. Peter in der Au (3352 Austria) and tested at the *OCH* test stand in Haag (3350 Austria).

In co-operation and consultation with the *AIT*, a drawing of the heat pump was created by *OCH* (see Fig. 8). Based on this model, the production department of *OCH* built the heat pump and transferred it to the test stand (see Fig. 9), where the *AIT* measurement system was connected to the heat pump and put into operation.

For transport and stability, the heat pump was attached to a metal frame, where also some sensors as well as both the *AIT* and the *OCH* control cabinets were mounted onto. The compressor *RS3-H040* was purchased from *SRMTEC*, the condenser *CB2115018NS* from *Provides*, the evaporator[7] *EV21200077N3* also from *Provides* and the separator *SL-28-219X543-ODS54* from *Frigomec*. The custom-made ejector was manufactured by *TBTECHNOLOGY* in Poland based on the simulation results and design developed during the *ETHP* project.

[7]The condenser and evaporator are both shell-and-tube heat exchangers. In the condenser, the refrigerant flows through the shell side, whereas in the evaporator, it flows through the tubes.

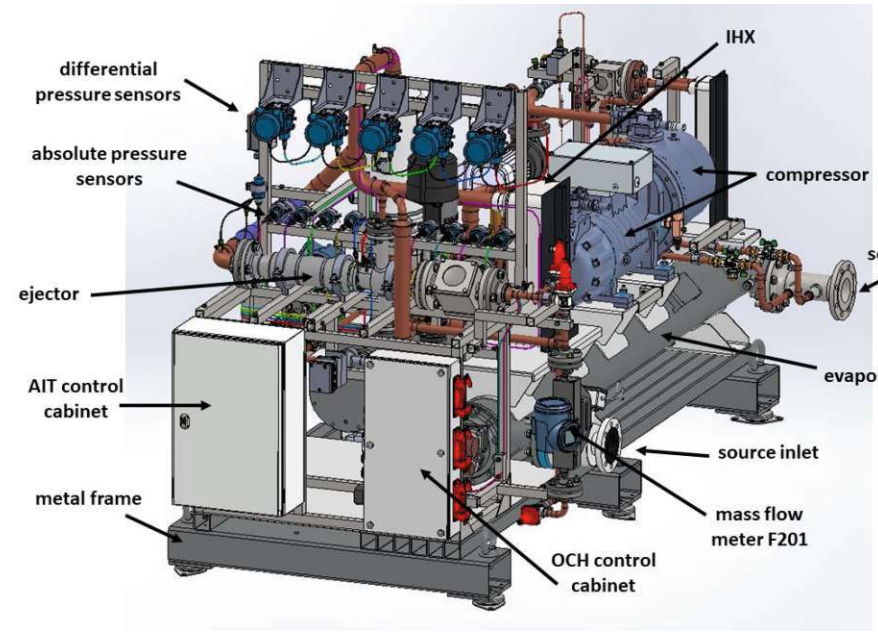

(a)

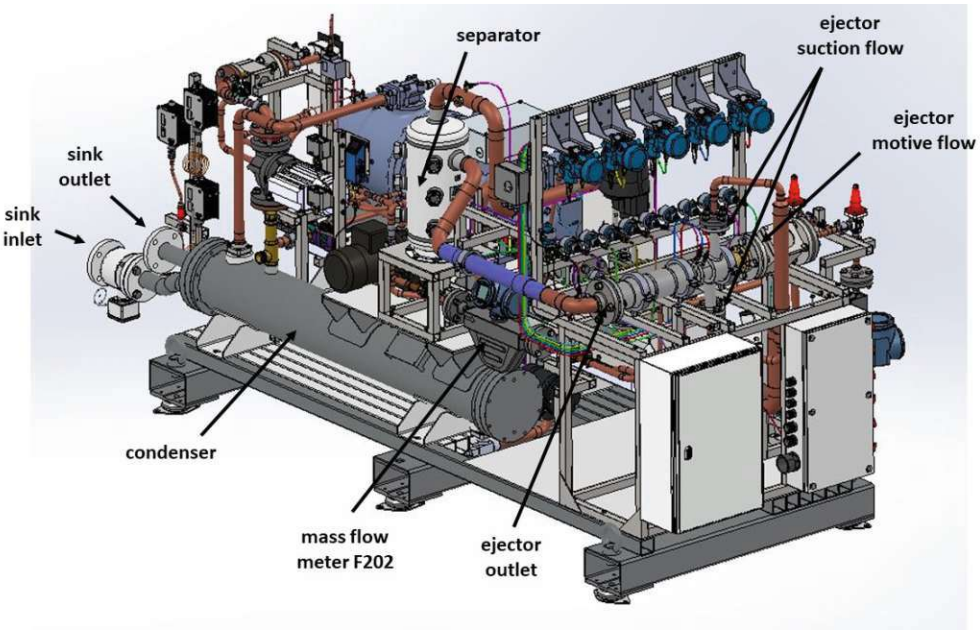

(b)

Figure 8: Drawing of the heat pump from different perspectives. (Created by *OCH*.)

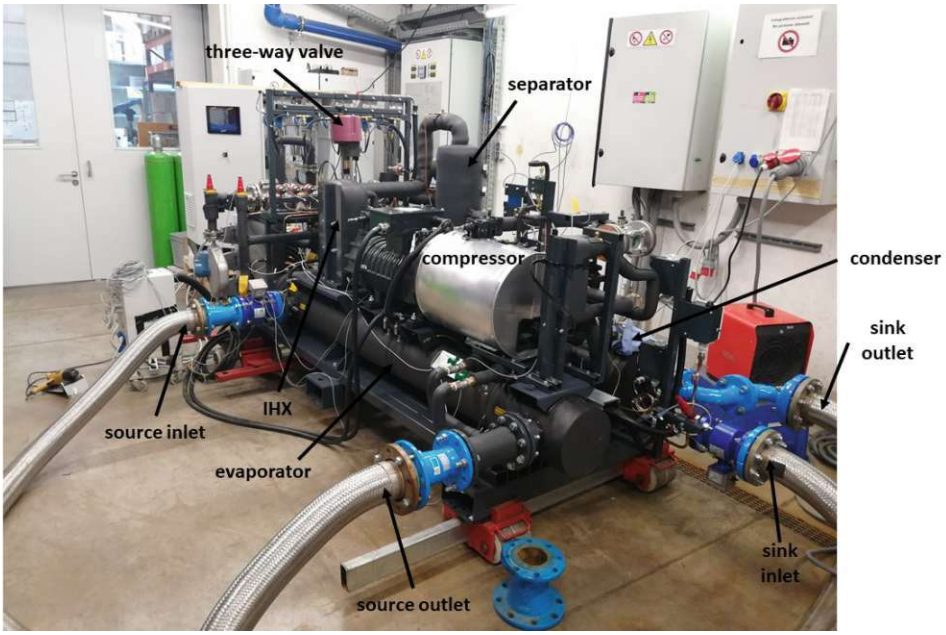

(a)

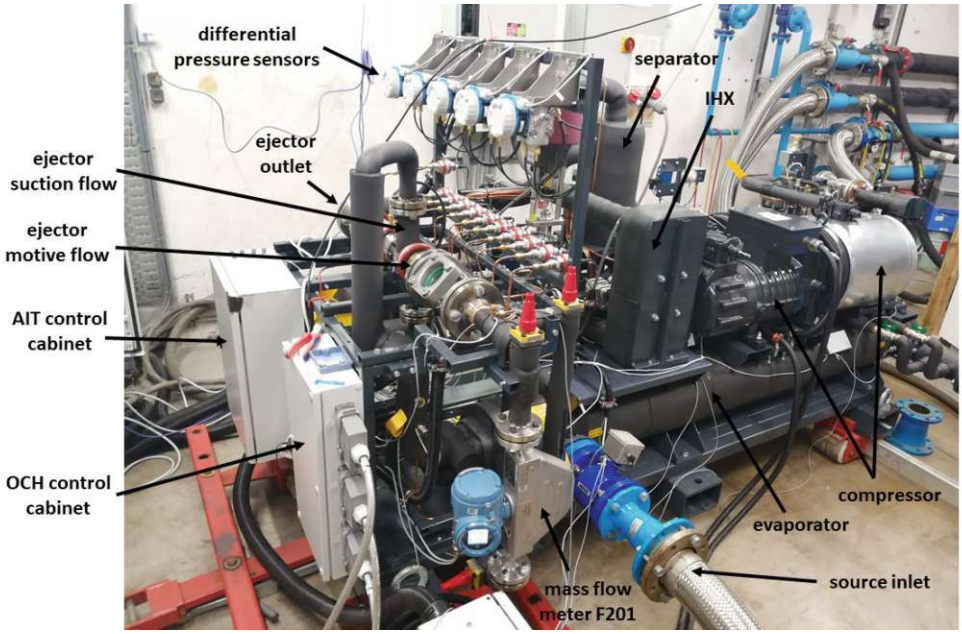

(b)

Figure 9: Heat pump on the test stand from different perspectives. (Pictures taken by the author)

3.2 Measurement System for Data Acquisition

Two independent measurement systems - one from *AIT* and the other one from *OCH* - were used to measure and monitor the heat pump.

The *OCH* system operates and controls the heat pump and the test stand, while the external measurement system from *AIT* does not interfere with the control of the heat pump (see Fig. 10). Both systems collect measurement data, such as temperatures, pressures, and mass or volume flow rates, from various locations in the refrigerant circuit.

During post-processing, the data from *OCH* and *AIT* are synchronised in order to validate the simulation data with regard to design point, compressor operating envelope and the performance of heat pump and ejector. In addition, the *AIT* measurement system facilitates real-time monitoring and visualisation of the measurement data in *LabVIEW*.

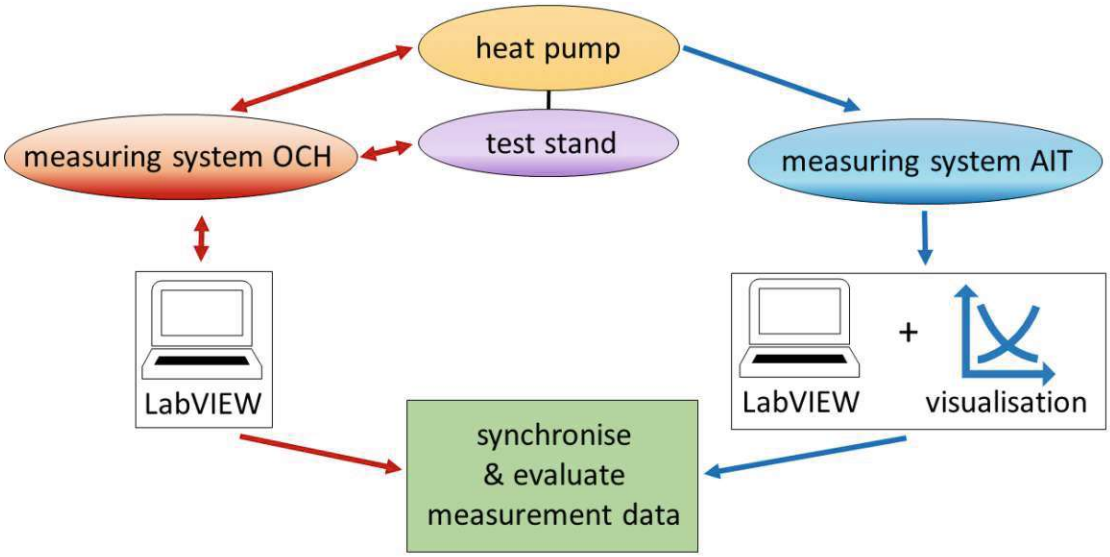

Figure 10: The heat pump is monitored by two measurement systems. The *OCH* system mainly controls the heat pump and the test rig, while the *AIT* system acquires data for real-time visualisation in *LabVIEW* and post-analysis. (Created by the author.)

Fig. 11 shows the flowchart of the heat pump. The measuring points in turquoise are integrated into the *AIT* measurement system, while the red measuring points from *OCH* are used to control the heat pump and the test stand. The refrigeration cycle is explained in more detail in subsection 3.5.

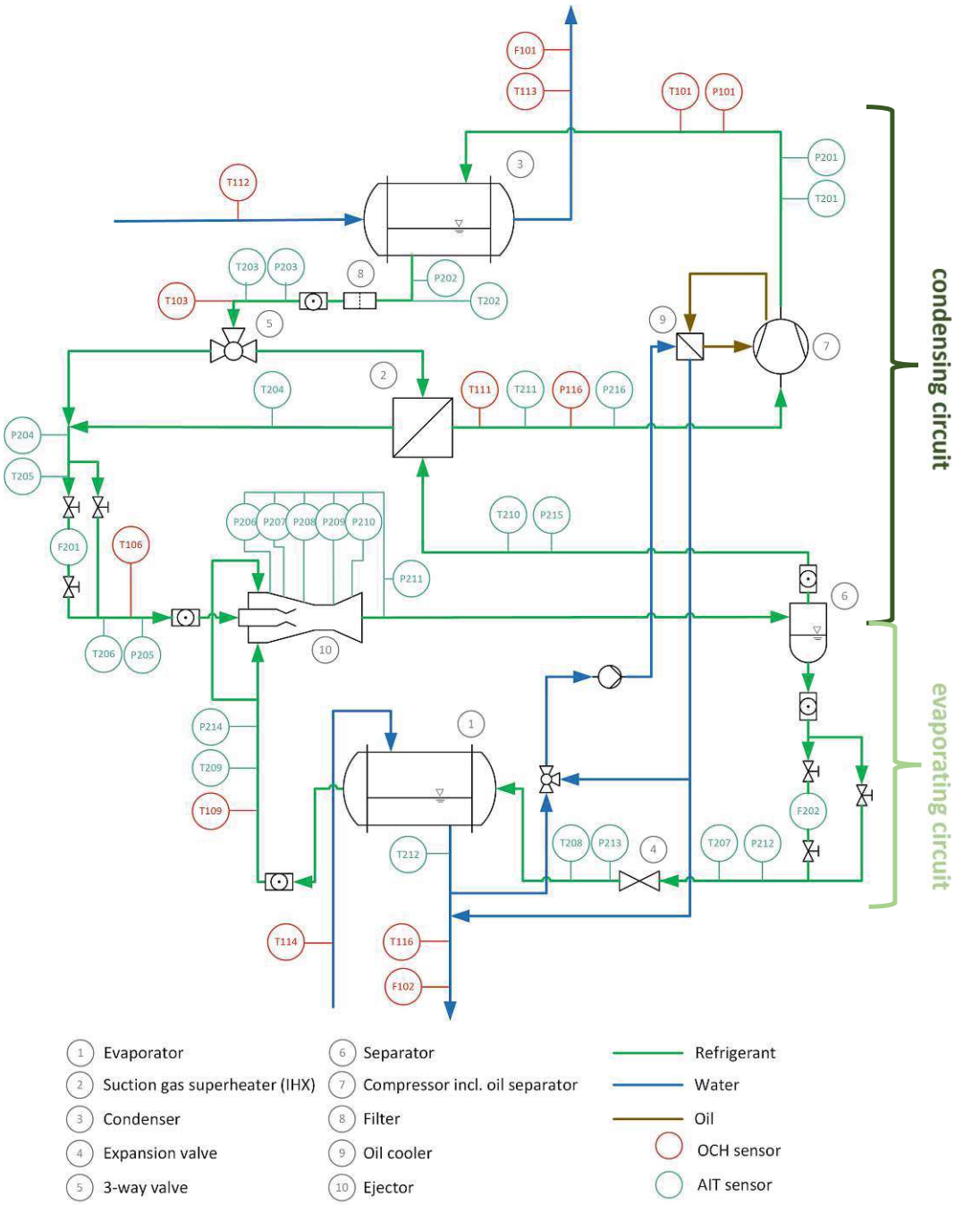

Figure 11: Flowchart of the heat pump. The red measuring points belong to the *OCH* measuring system, the turquoise ones to the *AIT* system. They are combined for analysis and post-processing. (Created by *AIT* and the author.)

3.3 Sensors

The *AIT* measurement concept comprises twelve temperature sensors, sixteen pressure sensors and two mass flow sensors (see Fig. 11). Each sensor is assigned an abbreviation: sensors beginning with the letter T are temperature sensors, those beginning with P are pressure sensors and those beginning with F are mass flow sensors. If the first number of the sensor is 2, the sensor is part of the measurement system from *AIT*. If it is 1, the sensor is integrated in the *OCH* measurement system. The last two digits number the sensors in sequence. The focus of this subsection lies on the sensors that were monitored by the *AIT*.

3.3.1 Temperature Sensors (T201-T212)

At twelve selected locations within the refrigeration circuit of the heat pump, the temperature was measured with the pipe contact sensors *TR4TP-1001* from *SONTEC* (see Fig. 12a). These *PT*1000 temperature sensors use silicone as cable material and a cable length of 10 m. They are suitable for a measurement range from −30 °C to 150 °C. Their data sheet can be found project documentation at *AIT*.

Before the measurements, the twelve temperature sensors, along with three additional backup temperature sensors, were calibrated in the calibration oven *PTC-155 Professional Temperature Calibrator* by *JOFRA* and *AMETEK* (see Fig. 13a). This calibration oven has an adjustable temperature range of −25 °C to 155 °C with an accuracy of ± 0.06 °C and a stability of ± 0.01 °C. Its data sheet is included in the project documentation at *AIT*.

Per calibration run, two sensors were put into the oven together with a pre-calibrated reference sensor (see Fig. 13b). The oven was heated up from −10 °C to 150 °C in steps of 10 °C and then cooled down to −10 °C again (see Fig. 13c). In this way, the temperature behaviour of all sensors was checked with regard to both heating up and cooling down.

Each specified oven temperature was maintained for 2 min such that the temperature fluctuations measured by the reference sensor were within a range of ± 0.01 °C at most. This ensured that the temperature sensors to be calibrated reached a stationary value at each specified oven temperature.

For each stationary temperature, by comparison with the temperature measured by the reference sensor the offset of the temperature sensors were determined. Using a second degree polynomial fit function, the calibration coefficients a_2, a_1 and d were calculated in *Microsoft Excel* for each sensor.

(a) Temperature sensor

(b) Absolute pressure sensor

(c) Differential pressure sensor

(d) Mass flow sensor

Figure 12: Temperature, pressure and mass flow rate sensors are used to acquire the desired measurement data in the refrigeration circuit. (Pictures taken by the author.)

(a) Control panel of the calibration oven

(b) Temperature sensors and reference sensor inside the calibration oven

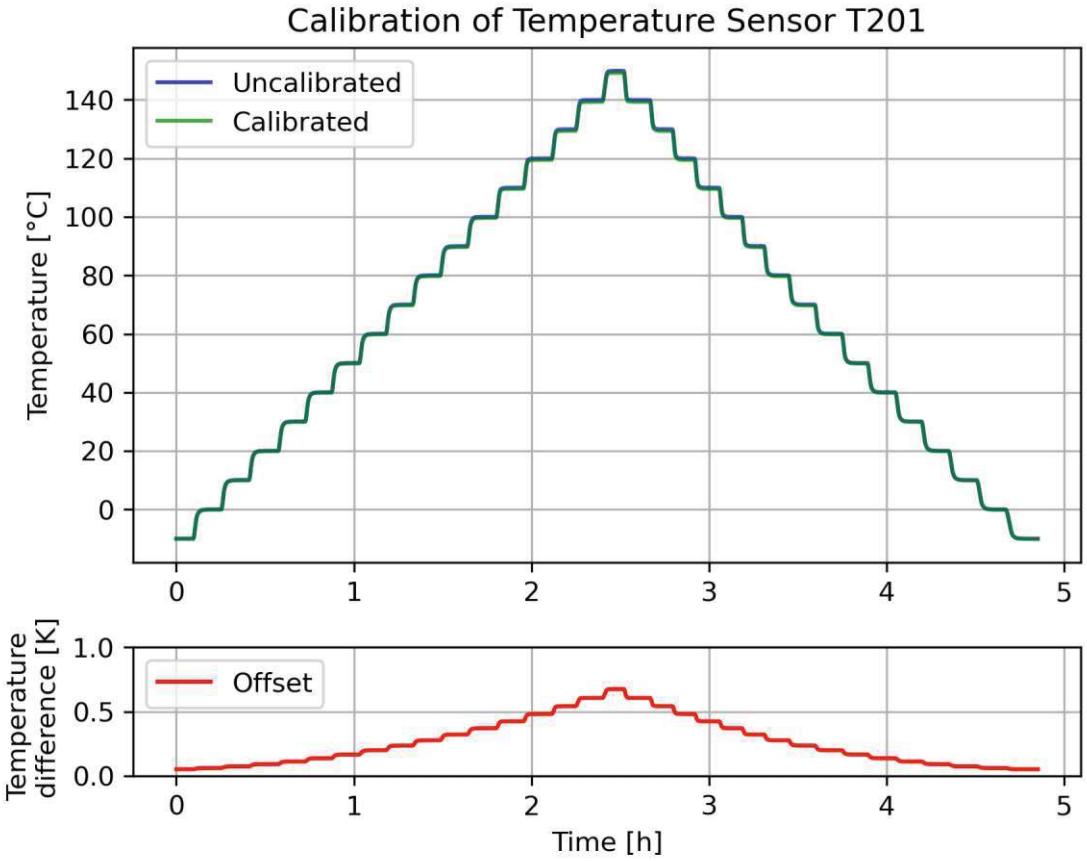

(c) Temperature curve of sensor T201 for calibration

Figure 13: Temperature calibration. (Pictures taken/created by the author.)

To receive the calibrated temperature value T_{cal} for a sensor measuring the temperature T_{meas}, these calibration coefficients are used according to Eq. 15.

$$T_{\mathrm{cal}} = a_2\, T_{\mathrm{meas}}^2 + a_1\, T_{\mathrm{meas}} + d \tag{15}$$

The temperature calibration data and the calculated calibration coefficients are shown in the Appendix. The process of identifying the stationary temperatures was automatised with a *Jupyter Notebook*, which can be found in the project documentation at *AIT*.

3.3.2 Pressure Sensors (P201-P216)

Eleven *Cerabar PMC21* absolute pressure sensors (P201 to P205 and P211 to P216, see Fig. 12b) as well as five *Deltabar M PMD55* differential pressure sensors (P206 to P210, see Fig. 12c) were purchased from *Endress+Hauser* to acquire pressure data at sixteen different locations in the refrigerant circuit.

As shown in Table 2, P201 to P205 have a measuring range from 0 bar to 40 bar, while P211 to P216 have a measuring range from 0 bar to 10 bar, both with a reference accuracy of up to 0.3 %. The differential pressure sensors P206 to P208 are capable of measuring pressure differences of up to ± 3 bar, while P209 and P210 are suitable only for up to ± 1 bar, both with a reference accuracy of 0.1 %. More specifications can be found in the data sheets in the project documentation at *AIT*.

The sensors each supply a current s of $s_{\min} = 4\,\mathrm{mA}$ to $s_{\max} = 20\,\mathrm{mA}$, which needs to be converted to the corresponding pressure value p in bar according to Eq. 16, with k and d being the two linear conversion coefficients and $p_{\max}$ and $p_{\min}$ being the upper and the lower pressure measuring limit. In Fig. 16, the current to pressure conversion function is shown for the sensors P201 to P206, where $p_{\min} = 0\,\mathrm{bar}$ and $p_{\max} = 40\,\mathrm{bar}$, leading to $k = 2.5\,\mathrm{bar/mA}$ and $d = -10\,\mathrm{bar}$.

$$p = k\,s + d, \qquad k = \frac{p_{\max} - p_{\min}}{s_{\max} - s_{\min}}, \qquad d = p_{\max} - k\,s_{\max} \tag{16}$$

3.3.3 Mass Flow Sensors (F201 and F202)

Two *Micro Motion F-Series F050* from *Emerson* (see Fig. 12d) are used to measure the mass flow rate in the refrigeration circuit with a measurement uncertainty of ± 0.2 %. F201 measures the mass flow rate in the condensing circuit, while F202 measures the

Table 2: Sensor specifications and conversion coefficients. (Created by the author.)

sensor name	measuring range [bar]	reference accuracy [%]	p_{min} [bar]	p_{max} [bar]	k [bar/mA]	d [bar]
P201-P205	0-40	0.3	0	40	2.5	-10.0
P206-P208	± 3	0.1	0	3	0.1875	-0.75
P209-P210	± 1	0.1	0	1	0.0625	-0.25
P211-P216	0-10	0.3	0	10	0.625	-2.5

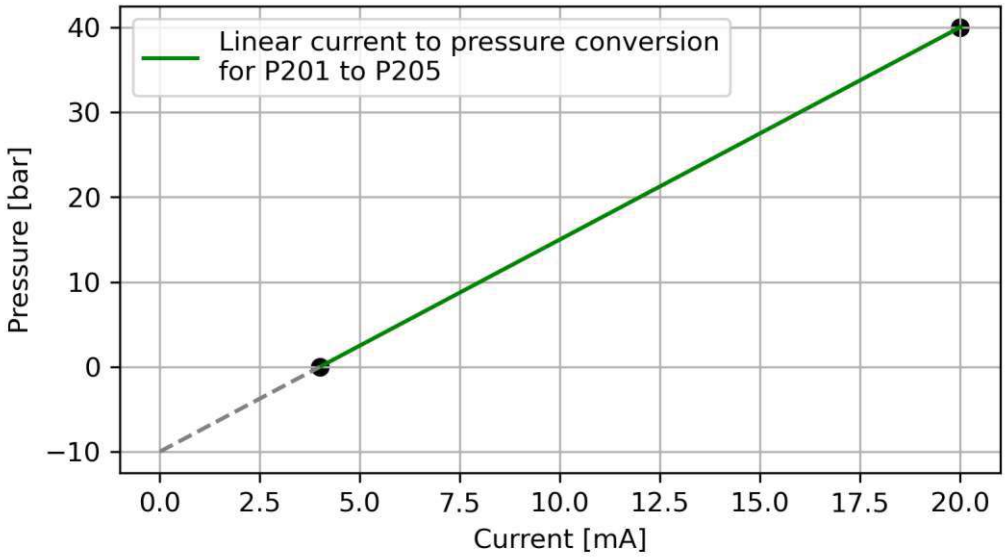

Figure 14: Linear current to pressure conversion based on the measuring range of the absolute pressure sensors P201 to P205. A current of 4 mA corresponds to a pressure of 0 bar, while the maximum value of 20 mA indicates a pressure of 40 bar. (Created by the author).

mass flow rate in the evaporator circuit. As these mass flow sensors cause a pressure drop in the refrigeration circuit, it is possible to route the refrigerant past the mass flow sensors using three-way valves in order to determine the performance of the heat pump without the pressure drop.

Similar to the process of current to pressure conversion, the electrical current of the mass flow sensors (4 mA to 20 mA) also has to be converted to a mass flow rate. With the measuring range of 0 kg/s to 1.13 kg/s, the conversion coefficients are approximately $k = 0.07\,\mathrm{kg/(s\,mA)}$ and $d = -0.28\,\mathrm{kg/s}$[8].

[8]In fact, s_{min} was found not to be exactly 4 mA, but instead 3.999 mA for F201 and 3.802 mA for F202. Thus, for F201 $k = 0.070\,62\,\mathrm{kg/(s\,mA)}$ and $d = -0.2624\,\mathrm{kg/s}$ and for F202 $k = 0.069\,76\,\mathrm{kg/(s\,mA)}$ and $d = -0.2652\,\mathrm{kg/s}$.

In the data sheets in the project documentation at *AIT*, F201 corresponds to "*Messstelle 1*" and F202 corresponds to "*Messstelle 2*".

3.4 Control Cabinet

All *AIT* sensor cables come together in the control cabinet. Its external dimensions are 60x40x20 cm and inside of it eight data modules are mounted onto top-hat rails (see Fig. 15).

A bus system from *ICP DAS* is used for the measurement data acquisition. This system offers separate modules for different measured variables. *Series 7033* modules are used to measure the temperature and Series *7017* for pressure and mass flow rate measurements. In addition, an interface module Series *7561* is required to establish the connection to the computer and *LabVIEW*.

For simplified cabling, the data lines of the sensors are collected on a terminal strip inside the control cabinet (see Fig. 16c). From there, the top four data modules ICP1 to ICP4 receive the data from the twelve temperature sensors T201 to T212. The two left-hand data modules in the bottom row, ICP5 and ICP6, get the signals from the pressure sensors and ICP7 (the second data module from the right in the bottom row) receives the signal from the two mass flow sensors. The data from these seven modules converge at the eighth module at the bottom right and are transmitted to the computer via the USB connection (see wiring diagram in Fig. 16).

The data modules as well as the pressure sensors require a power supply of 24 V, which is provided by the power transformer next to the eighth data module. Fig. 16b shows a detailed view of the cabling of the temperature, pressure and mass flow sensors. The cables connecting the data modules to the terminal strip are permanently wired, whilst the sensor cables between the terminal strip and the sensors are only wired for the measurements and are otherwise detached so that the control cabinet can be moved around more easily.

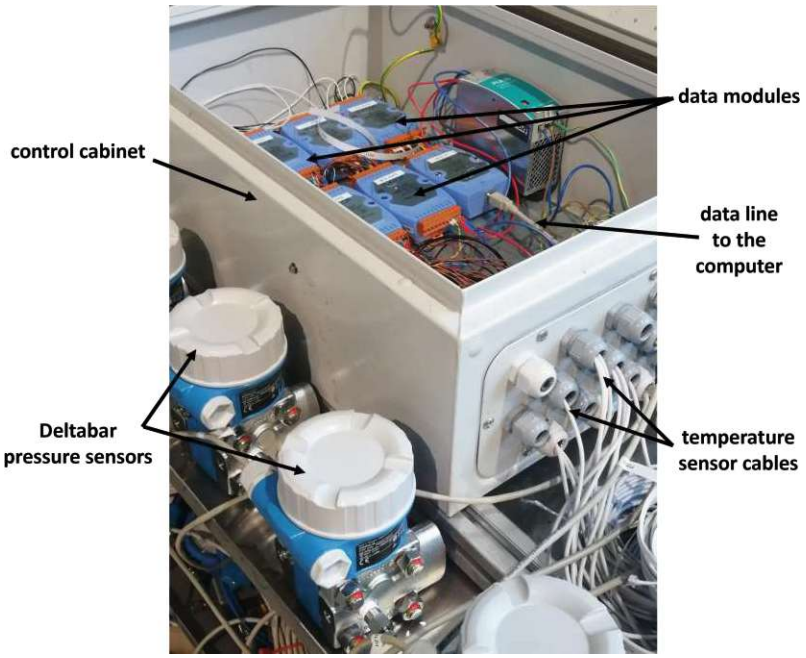

(a) Outside

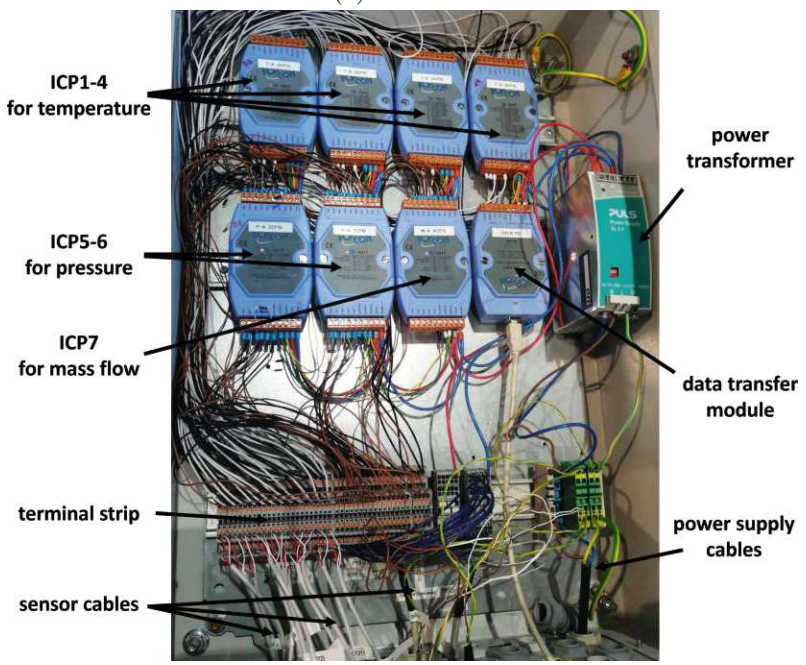

(b) Inside

Figure 15: The control cabinet houses the *ICP DAS* data modules. These pictures were taken by the author during the test and calibration phase. Here, only the temperature and differential pressure sensors are connected to the data modules.

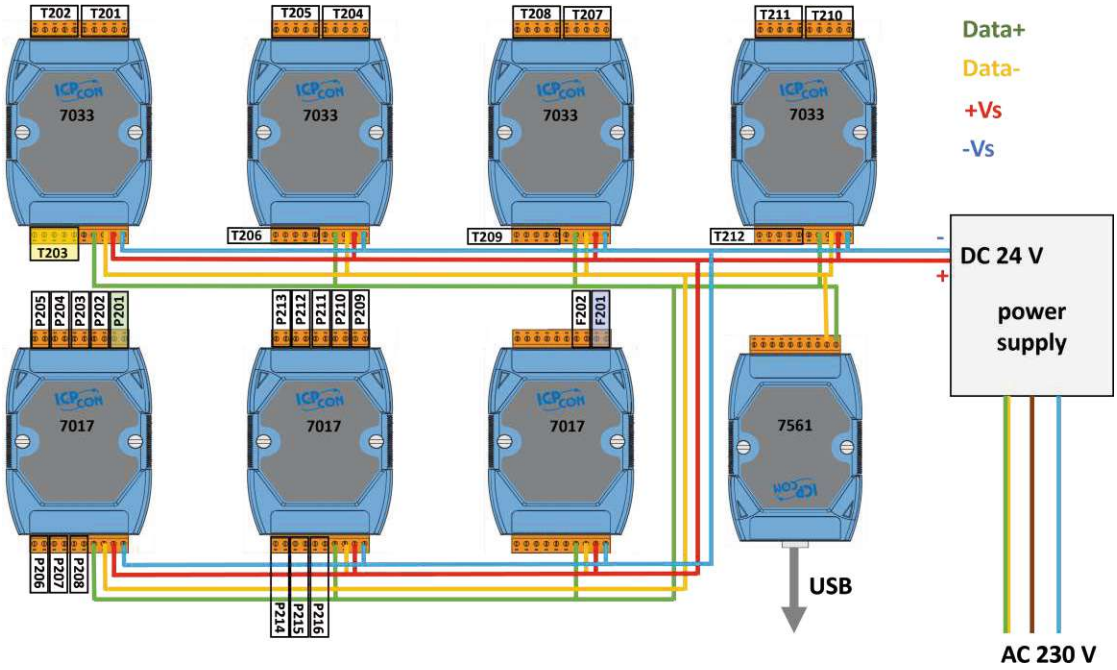

(a) Schematic overview of the cabling in the control cabinet

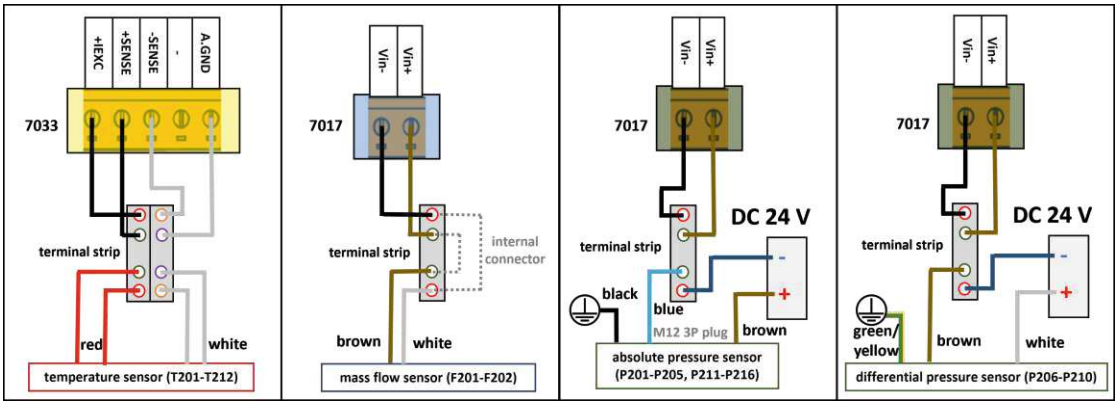

(b) Detailed view of the cabling of the individual sensor types

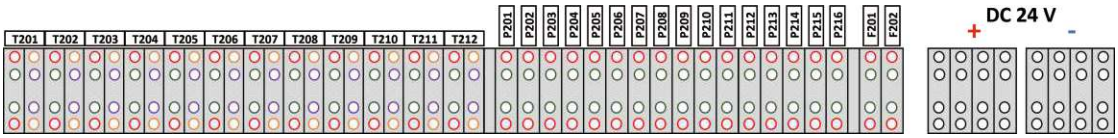

(c) Arrangement of the sensors on the terminal strip

Figure 16: Wiring diagram of the electrical cables inside the control cabinet for connecting the data modules. The data lines from the terminal strip to the data modules are permanently wired, while the sensors are only connected to the terminal strip for measurements so that the control cabinet can otherwise be transported and stored independently of the sensors. (Created by the author.)

3.5 Working Principle of the Refrigerant Circuit

On the basis of the pressure enthalpy diagram in Fig. 17, this subsection describes the working principle of the refrigerant circuit step by step. (A) Gaseous refrigerant from the separator enters the IHX to increase the suction gas superheating (T210, P215). (B) The compressor pressurizes the preheated refrigerant, raising its temperature and converting it from a low-pressure gas (T211, P216) to a high-pressure gas (T201, P201, hot gas superheating).

(C) In the condenser, the high-pressure gas condenses into a high-pressure liquid (T202, P202) and releases heat to the sink water. During this process, the enthalpy strongly decreases (subcooling). (D) A filter dryer is located between the condenser and the three-way valve to remove any moisture, dirt, or other contaminants from the refrigerant to ensure the proper functioning and longevity of the heat pump system by preventing potential damage or blockages caused by impurities in the refrigerant (T203, P203).

(E) Then, the three-way valve redirects the flow of the refrigerant either to the IHX or directly to the mass flow meter F201 (T205, P204). (F) To observe the temperature drop at the IHX, temperature sensor T204 is located directly downstream of the IHX, before the two branches separated by the three-way valve are rejoined. The point (F2) was subsequently added to the pressure enthalpy diagram to visualise the pressure drop caused by the mass flow meter F201 (T206, P205).

(G) High-pressure liquid refrigerant enters the ejector's motive nozzle, mixes with the gaseous refrigerant from the evaporator (T209, P214), and exits the ejector as a two-phase mixture at an intermediate pressure level (P211). This point lies within the vapour pressure curve. As the vapour quality at the outlet of the ejector is neither measured nor calculated in real-time, for better visualisation in the pressure enthalpy diagram a vapour quality of $x = 0.677$ was assumed, which corresponds to the results of the simulations that were conducted while designing the heat pump.

The separator ensures that gaseous refrigerant enters the IHX (T210, P215) and subsequently the compressor (A), while liquid refrigerant passes through the mass flow meter F202 (H) (T207, P212).

(I) The expansion valve regulates the inflow into the evaporator and causes an isenthalpic pressure drop (T208, P213). (J) In the evaporator, heat is absorbed from the water-side of the source, causing the refrigerant to evaporate into a low-pressure gas (T209, P214). (K) (=(G)) The fast motive flow from (F2) causes the gaseous refrigerant from the evaporator to be sucked into the ejector. Subsequently, the two-phase mixture enters the separator (P211), where the gas and liquid components are once again separated and directed towards the condensing (A) (T210, P215) and the evaporating circuit (H) (T207, P212), respectively.

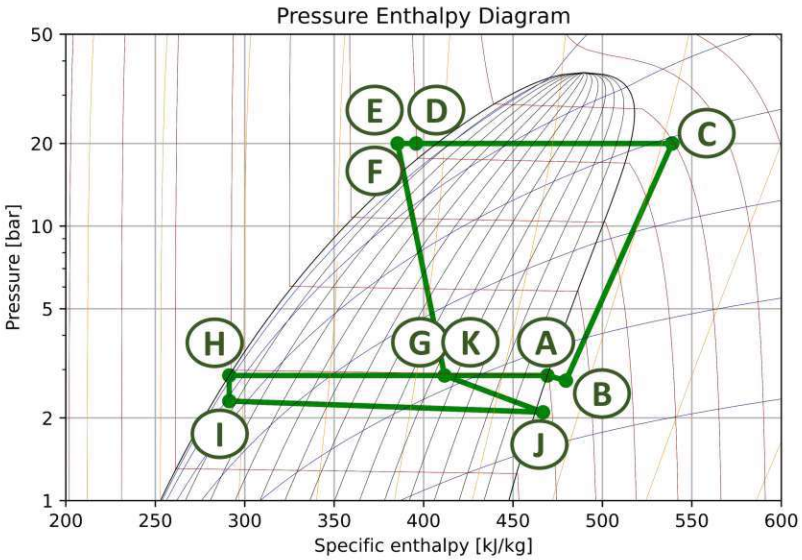

(a) Pressure enthalpy diagram of the heat pump simulated for the design conditions

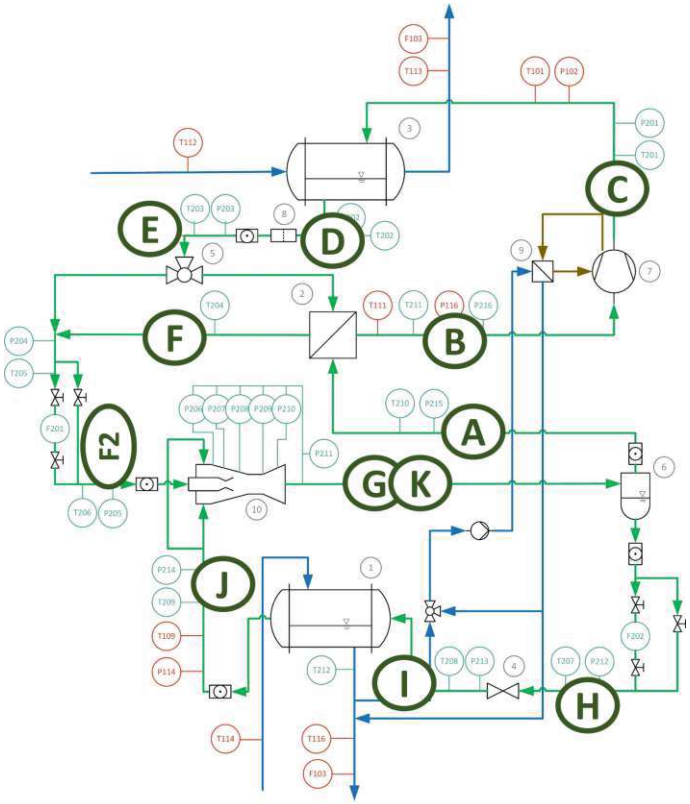

(b) Corresponding points in the flowchart

Figure 17: The refrigerant cycle is visualised with both the flowchart of the heat pump and the simulated pressure enthalpy diagram. (Created by the author.)

3.6 Test Rig for Controlling the Heat Pump

On the hydraulic side of the *OCH* test rig (see Fig. 18), the volume flow rates of the source and sink water are controlled by circulation pumps. A buffer tank is either heated to the desired source temperature with a heating rod or cooled via a plate heat exchanger that is connected to a cooling well. To reach the required sink temperature, the sink water runs in a short circuit and is heated by the heat pump itself[9].

Once the right sink temperature is reached, some water is sent to the buffer tank. At the same time, some water is also introduced from the buffer tank to help maintain a constant temperature at the inlet of the water-side of the sink. The water temperature differences at the evaporator and the condenser are controlled through the volume flow rates and the inlet temperatures.

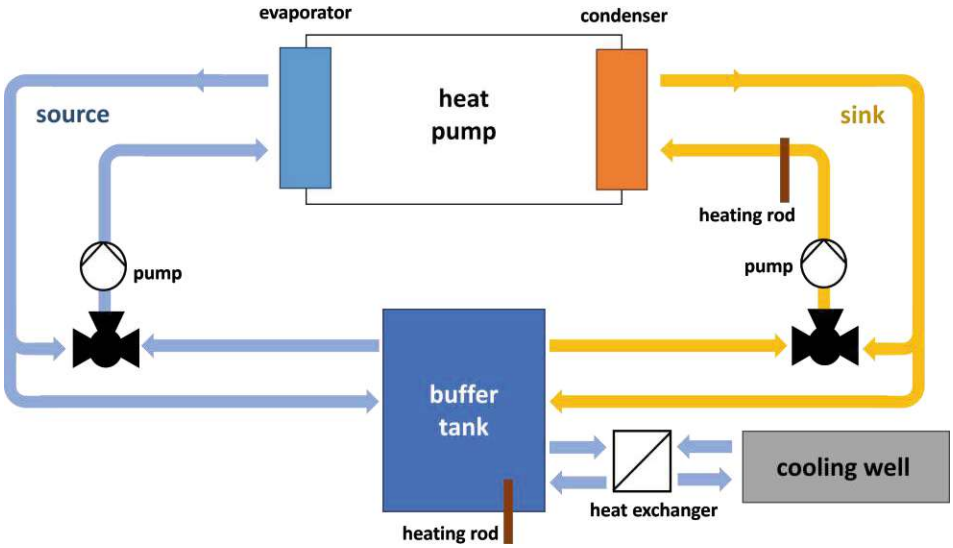

Figure 18: Simplified schematic of the water-side control of the *OCH* test rig. (Created by the author.)

To start the heat pump, first, the buffer tank and the sink are heated up with the heating rods. Simultaneously, heating tapes on the IHX and the separator preheat the refrigerant, ensuring it becomes gaseous before reaching the compressor.

Then, the compressor is switched on and the heat pump itself has to continuously further raise the temperature of the sink water until the desired steady state conditions are reached.

[9] Additionally, for sink temperatures below 100 °C on the water-side, a second heating rod can be used to heat up the sink water more quickly.

During the operation of the heat pump, the following parameters are regulated:

- The three-way valve downstream of the condenser is adjustable from 0 % to 100 % in increments of less than 0.5 % with a 0 to 10 V control signal. At 100 %, everything flows over the branch with the IHX. The valve automatically adjusts based on the specified value of suction gas superheating.

- The expansion valve is also adjustable in increments of less than 0.5 % with a 0 to 10 V control signal. It regulates automatically depending on the specified value of superheating downstream of the evaporator.

- The compressor operates at power levels of 25 %, 50 %, 75 %, or 100 %. However, the power levels below 100 % are normally only used while starting the compressor.

3.7 Real-Time Visualisation in *LabVIEW*

Via an USB connection, the measurement data is transferred from the electrical cabinet to a computer. Then, *LabVIEW* is used to process and save the measurement data and display it graphically. The library *CoolProp* is embedded in the program to calculate thermodynamic state variables like the enthalpy, to create and display the pressure-enthalpy diagram in real-time. The time curves of pressure, temperature and mass flow rate, as well as the compressor envelope, the pressure profile inside the ejector and the ejector efficiency are also displayed graphically on the *LabVIEW* interface.

The *LabVIEW* program can be divided into three parts: 1. user input and start of the program, 2. data acquisition, calibration and logging, and 3. data evaluation and visualisation.

1. User Input and Start of the Program (see Fig. 19)

Before the program is started, the user has to select the correct **COM PORT**, which depends on the device settings of the computer, where it states on which port the data modules are assigned to. The field **Which data?** is used to decide whether the measurement data should be analysed (**get data**-indicator turns green) or whether only pre-stored simulated data should be used for test purposes (**get data**-indicator stays red).

The name of the log file consists of the time and date when the measurements are started as well as the content of the cell **Filename**. When the program is running, the data logging can be activated by clicking on **START/STOP LOG**. Then the **logging active**-indicator turns green. In **stationary for [sec]** a time span can be selected

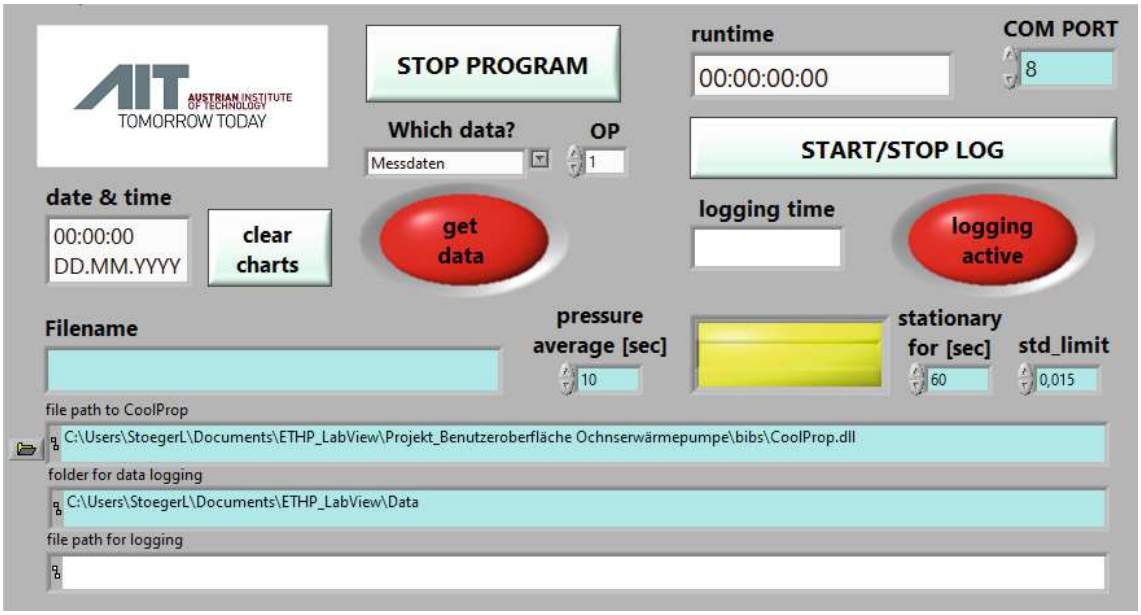

Figure 19: *LabVIEW* control panel to control data storage, identify stationary conditions and specify the main settings. (Created by the author.)

to identify stationary operating conditions: when certain temperature values have a standard deviation of less than specified in **std_limit** within that time span, the yellow indicator turns green and shows "stationary conditions".

In addition, to average out sudden pressure surges and fluctuations of the mass flow rates, the number of seconds in **pressure average [sec]** can be changed to adjust the temporal resolution of the pressure and mass flow rate measurements. When the measurements are finished, the program including the data logging is stopped by clicking on **STOP PROGRAM**.

2. Data Acquisition, Calibration and Logging

Every second, the *LabVIEW* program retrieves the measurement data from the data modules. The calibration and conversion coefficients for the respective sensors are implemented in *LabVIEW* so that the calibrated/converted pressure, temperature and mass flow rate values can directly be displayed.

The filling level in the separator as well as the strength of bubble formation (strong, low or no "bubbling") in the sight glasses can be entered in the program (see Fig. 20b), which is only done manually from time to time and might prove useful for evaluation purposes.

For post-processing of the measurement data, both the raw data and the calibrated and converted data are stored in a file, along with the separator filling level, bubbling values and a runtime variable that enables subsequent time calibration and synchronisation to*OCH* data streams.

3. Data Evaluation and Visualisation

The calibrated/converted measurement data are used to calculate the following quantities, which are then displayed in *LabVIEW* in real-time.

- **Pressure Enthalpy Diagram** (see Fig. 21a)
  Using temperature and pressure values as input, the library *CoolProp* (Bell et al., 2014) calculates the enthalpies at various points in the refrigeration circuit. The simulated values for the design point are also stored in the *LabVIEW* program, so that by comparing the current data with the simulation results, direct conclusions can be drawn about the current operation of the heat pump[10].

- **Compressor Envelope** (see Fig. 21b)
  The compressor operating envelope visualises the application limits of a compressor and is specific for each compressor type. Horizontally it is bound by the minimum and maximum suction gas pressure, and vertically as well as diagonally by the maximum and minimum achievable pressure ratios. The bevelled corner in the upper right is restricted due to compressor current absorption (SRM-Technology, 2021).

  In the compressor envelope in Fig. 21b, the operating point is defined by the saturation temperature corresponding to the pressure at the compressor inlet (P216) as the x-value[11], and the saturation temperature corresponding to the pressure downstream of the compressor (P201) as the y-value.

[10] The enthalpy cannot be calculated directly for points within the vapour pressure curve. The simulated vapour content $x = 0.677$ is used here.

[11] Usually the refrigerant's temperature downstream of the evaporator corresponds to the temperature at the inlet of the compressor. However, due to the ejector and separator in the refrigerant circuit of the heat pump discussed in this thesis, these two temperatures differ. Therefore, instead of "evaporating temperature", the term "saturated suction gas temperature" is employed to accurately describe the inlet conditions of the compressor.

- **Global Ejector Characteristics** (see Fig. 21b)
  The operating point of the ejector is shown with the entrainment ratio ψ as x-value and the suction pressure ratio Π_s as y-value, which is calculated according to Eq. 17 and 18.

$$\psi = \frac{\dot{m}_{\text{suc}}}{\dot{m}_{\text{mot}}} = \frac{F202}{F201} \tag{17}$$

$$\Pi_s = \frac{p_{\text{out}}}{p_{\text{suc}}} = \frac{P211}{P214} \tag{18}$$

- **Ejector Efficiency** (see Fig. 21c)
  The efficiency η of the ejector is calculated using *CoolProp* data according to Eq. 19

$$\begin{gathered} \eta = \psi \, \frac{h(p_{\text{out}}, S_{\text{suc}}) - h(p_{\text{suc}}, S_{\text{suc}})}{h(p_{\text{mot}}, S_{\text{mot}}) - h(p_{\text{out}}, S_{\text{mot}})} \\ \text{with} \\ S_{\text{suc}} = S(P214, T209) \quad S_{\text{mot}} = S(P205, T206) \\ p_{\text{suc}} = P214 \quad p_{\text{mot}} = P205 \quad p_{\text{out}} = P211 \end{gathered} \tag{19}$$

- **Estimation of the COPh** (see Fig. 21c)
  The COPh is defined as the ratio of the heating capacity generated E_g divided by the electrical power E_{el} required for the compressor. These quantities were not recorded with the *AIT* measurement system, but the COP was, nevertheless, estimated using the law of energy conservation[12].

  The generated heating capacity E_g equals the thermal energy from the source E_s plus the electrical power E_{el} minus all possible heat losses L. Therefore, if we neglect the losses ($L \approx 0$), $E_{el} \approx E_g - E_s$. The heat transfer in source and sink can be calculated from the product of the enthalpy difference Δh multiplied by the mass flow, see Eq. 20.

$$\begin{gathered} COP = \frac{E_g}{E_{\text{el}}} = \frac{E_g}{E_g - E_s} = \frac{\Delta h_{\text{con}} \, F201}{\Delta h_{con} \, F201 - \Delta h_{\text{eva}} \, F202} \\ \Delta h_{\text{con}} = h(P201, T201) - h(P202, T202) \\ \Delta h_{\text{eva}} = h(P214, T209) - h(P213, T208) \end{gathered} \tag{20}$$

[12] During post-processing only the COP measured by *OCH* was considered. However, this estimate was used to roughly asses the performance of the heat pump in real-time.

When calculated according to Eq. 20, the COP is about a fifth larger than in the simulations, presumably due to the assumption that the heat losses could be neglected. To account for this error, the calculated COP was multiplied by the (manually adjustable) factor of about 0.79 before being displayed in *LabVIEW* for real-time analysis.

- **Suction Gas Superheating** (see Fig. 21c)
  At the inlet of the compressor, the refrigerant should only be present in the gaseous phase. The suction gas superheating measures the temperature difference between the temperature at the inlet of the compressor (T211) and the condensation temperature that corresponds to the pressure at the inlet of the compressor (P216). According to *OCH*, the suction gas superheating should always be larger than 5 K to ensure that only gaseous refrigerant enters the compressor. If the suction gas superheating is smaller than 5 K, the corresponding display element will turn yellow to indicate that the compressor could get damaged.

- **Hot Gas Superheating** (see Fig. 21c)
  By subtracting the temperature downstream of the compressor (T201) from the saturation temperature that corresponds to the pressure at the outlet of the compressor (P201), the value of hot gas superheating can be calculated. If the hot gas superheating is smaller than 5 K, the green indicator will turn yellow, as only gaseous refrigerant should exit the compressor.

- **Condenser Subcooling** (see Fig. 21c)
  The subcooling downstream of the condenser is calculated by subtracting the saturation temperature that corresponds to the pressure at the outlet of the condenser (P202) from the temperature of the refrigerant at the outlet of the condenser (T202).

In addition, the flowchart of the heat pump and time series of the temperatures, pressures and mass flow rates are displayed in the *LabVIEW* environment (see Fig. 20c). Furthermore, the pressure profile inside the ejector is shown (see Fig. 20a), as well as certain error indicators. To compare the current measurement data with the design conditions, various results (COP, suction gas superheating, subcooling) of the simulations at the design conditions are also visualised.

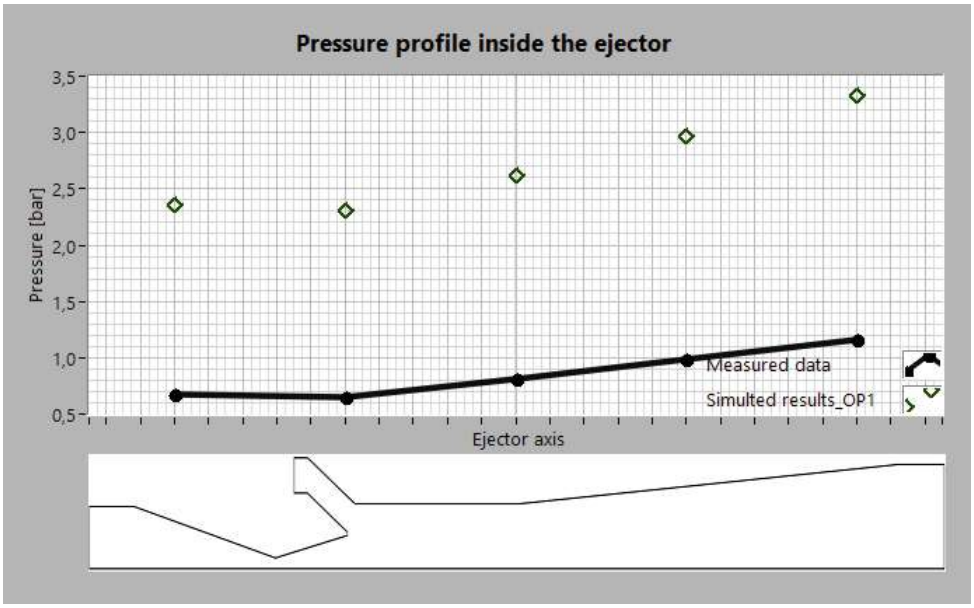

(a) Pressure profile inside the ejector

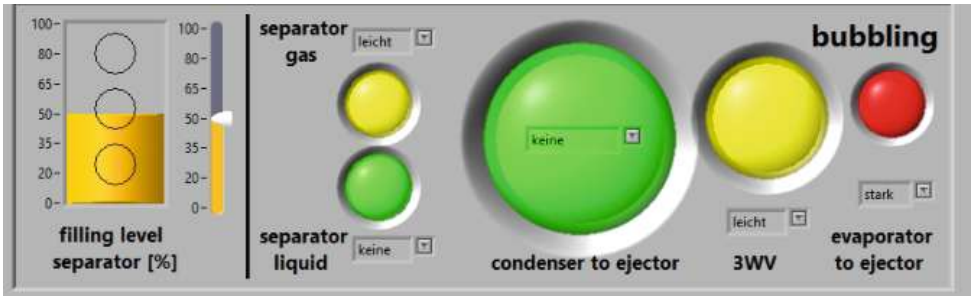

(b) Filling level in the separator and bubbling

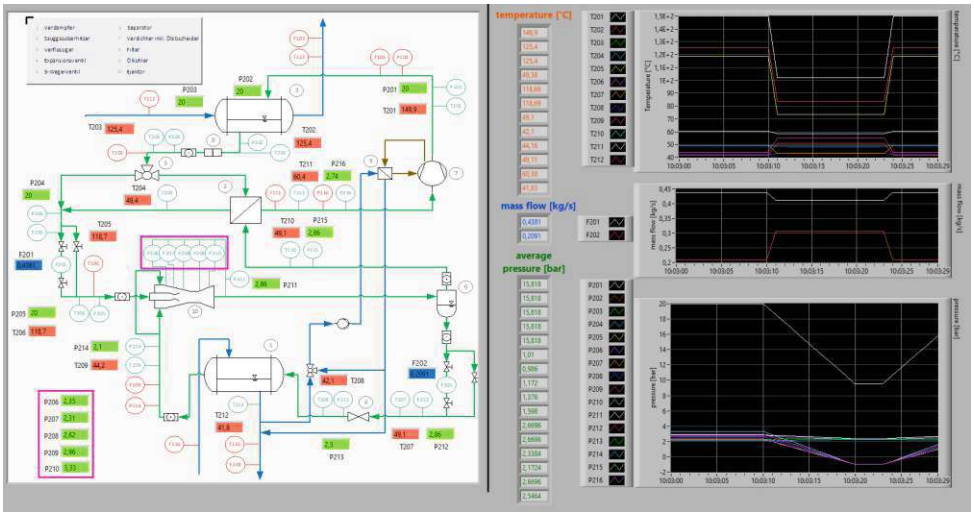

(c) Flowchart and time series of the measured variables

Figure 20: Real-time visualisation in *LabVIEW* (part 1). (Created by the author.)

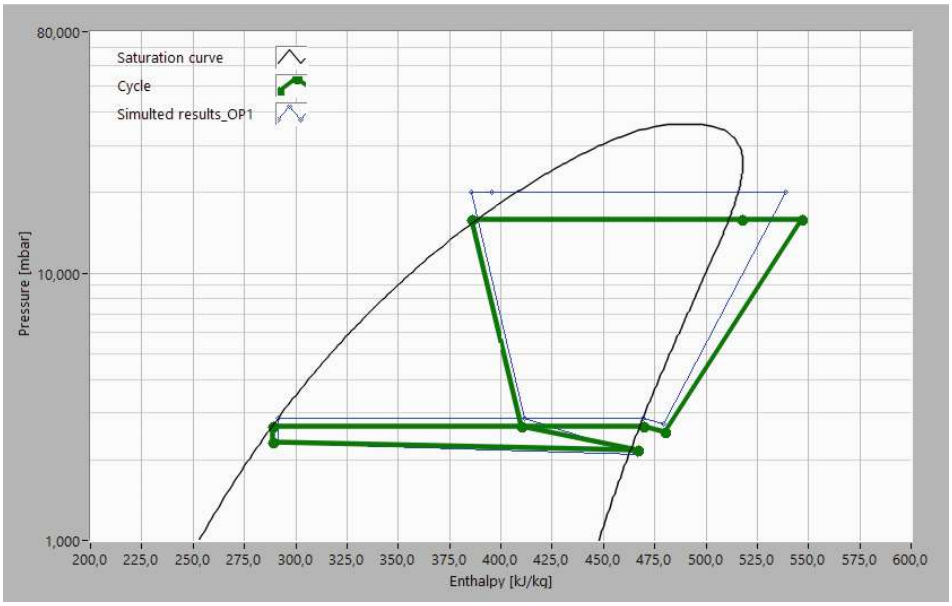

(a) Pressure enthalpy diagram

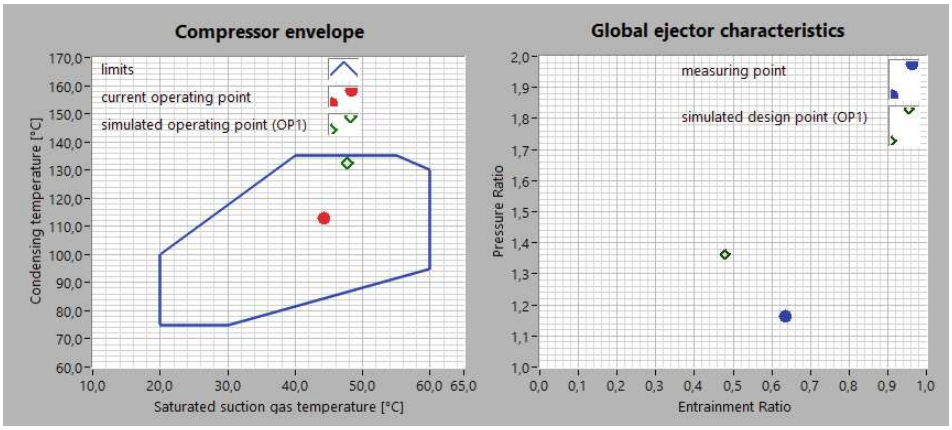

(b) Compressor envelope and global ejector characteristics

(c) Important parameters of the heat pump

Figure 21: Real-time visualisation in *LabVIEW* (part 2). (Created by the author.)

Programming Logic

In *LabVIEW*, the front panel serves as the user interface while the block diagram houses the graphical code that dictates the program's functionality. Code can be outsourced in virtual instruments, so-called SubVIs, and displayed in compact form to provide a better overview.

In the block diagram in Fig. 22, the outer frame is a flat sequence structure. This ensures that the block on the left is executed first, which establishes the connection to the data modules and reads the data from certain input windows on the user interface. Secondly, the block in the middle, which contains a while loop that covers the whole block, is continuously carried out once per second, until the program is stopped. When the button **STOP PROGRAM** is pressed, the third block of the flat sequence structure is executed and the connection to the data modules is terminated.

The most important elements in the block diagram are labelled depending on the part of the program they are used in:

① These elements include user input fields and SubVIs for establishing and terminating the connection to the data modules.

② The measurement data is retrieved from the data modules in the **get data** SubVI and the temperature values are calibrated using the respective calibration coefficients. The pressure and mass flow sensors provide a current from 4 mA to 20 mA, which is converted to a pressure value in bar or a mass flow rate in kg/s. Also, the pressures averaged over the last few seconds are calculated.

③ The third part of the block diagram focuses on real-time visualisation of various properties. Here, for instance, the ejector efficiency or the suction gas superheating are calculated, the flow chart and the pressure enthalpy diagram are displayed and the time series of temperature, pressure and mass flow are shown. In addition, the SubVI **data logging** receives both the raw measurement data as well as the calibrated/converted values together with the entries in the user input fields regarding bubble formation and the filling level in the separator.

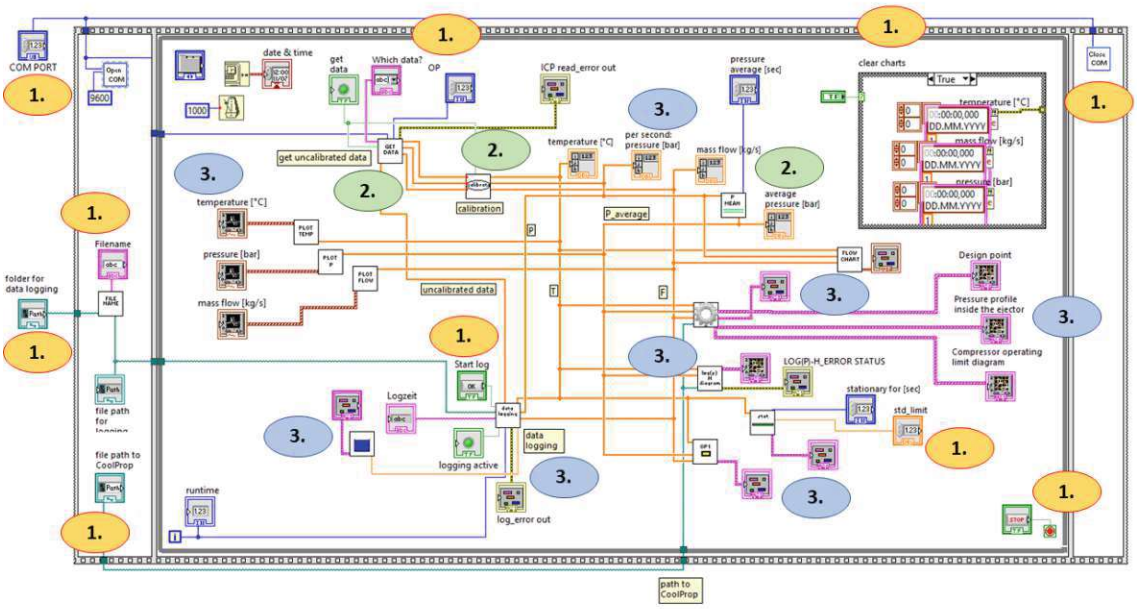

Figure 22: *LabVIEW* block diagram. The different parts are labelled according to the part of the program in which they appear. (Created by the author.)

3.8 Post-Processing of the Measurement Data

The real-time visualisation with *LabVIEW* aims to provide initial insights into the current operating state while the heat pump is running to support the experiments. Detailed data analysis is conducted during post-processing and includes the following steps:

1. The data from *AIT* and *OCH* are synchronised automatically using a *Jupyter Notebook*.

2. For each measurement day, the time where data from both *AIT* and *OCH* is available is considered relevant for post-processing.

3. Graphs depicting the temporal evolution of temperature, pressure, and mass flow values are generated, incorporating data on superheating and subcooling.

4. The performance of the entire heat pump is analysed regarding heating capacity, COP, Carnot-efficiency[13] and the overall energy balance.

5. In the final step, selected components of the heat pump (compressor, condenser, evaporator, IHX and ejector) are examined separately regarding their performance.

More information concerning the numerical setup for post-processing and data analysis can be found in the project documentation at *AIT*.

[13]The Carnot efficiency is the ratio of the measured COP to the maximum theoretically achievable Carnot COP.

4 Experimental Characterisation

At the end of April, 2024, the heat pump had been assembled by *OCH* and was connected to the *OCH* test rig for the first measurement campaign. The main goal of this campaign was to reach the design conditions of the heat pump and ejector to characterise the heat pump's performance and efficiency in steady-state operation.

According to the simulations that were conducted while designing the heat pump, at the design point the heating capacity is expected to be about 60 kW, with a COP of 2.04, 20 bar on the high-pressure side and 2.7 bar at the compressor inlet. The suction gas superheating at the simulated design point is 12.7 K, the hot gas superheating 17.3 K, the temperature at the compressor inlet about 60 °C and downstream of the compressor about 150 °C.

At the design conditions, the mass flow rate in the condensing circuit is 0.438 kg/s and 0.209 kg/s in the evaporating circuit based on the simulations. On the sink side, the water flows into the condenser at 115 °C and out 130 °C. On the source side, the water temperatures are 45.5 °C upstream and 41.8 °C downstream of the evaporator. A more detailed overview of the respective temperatures, pressures and mass flow rates in the refrigerant circuit at design conditions is shown in the Appendix.

A measurement plan was prepared, consisting of three different testing points A, B and C[14] and nine different measurement configurations[15] for each testing point. Unfortunately, the design conditions were not reached during this initial measurement campaign due to various experimental challenges. As a result, the focus shifted away from the planned testing points and measurement configurations. Instead, the new goal became achieving higher temperatures and pressures to approach the design point.

4.1 Measurement Campaign Overview

During the initial weeks of the measurement campaign, no significant measurements could be carried out due to a malfunction in the electrical control of the three-way valve, necessitating its replacement. By May 15, 2024, the heat pump was finally operational with all components functioning correctly, to the best of the assessment at that time.

[14] For all the three testing points, the desired water inlet temperature at the condenser was 115 °C and the outlet temperature 130 °C, to ensure high-temperature operation near the design conditions. The water inlet and outlet temperature at the evaporator was designed differently for each testing point. A: 45 °C in and 40 °C out, B: 50 °C in and 45 °C out and C 40 °C in and 35 °C out

[15] It was planned to vary both the suction gas superheating and the superheating downstream of the evaporator from 4 K to 12 K respectively with a step-size of 4 K to explore various configurations regarding the positioning of the three-way valve and the expansion valve.

Till June 10, 2024, ten days of measurements were conducted as detailed in Table 3, with the compressor operating for approximately 27 hours in total. The refrigerant charge was varied during the first five measurement days. Based on the simulated ideal charge of 36 kg of R1233zd(e), which did not account for factors like piping, the refrigerant charge was gradually increased by *OCH* until a significant jump was made from 49 kg down to 32 kg due to insufficient heating capacity at 49 kg. Subsequently, all further measurements were conducted using only 32 kg.

Table 3: Overview of the relevant days of the measurement campaign. As condenser mass flow, heating capacity and COP vary over time during each of the measurement days, characteristic values were selected of each respective day. (Created by the author.)

Day	**Start**	**End**	**Refr. Charge [kg]**	**F201 [kg/s]**	**Heating Capacity [kW]**	**Carnot Efficiency [%]**	**Characteristics**
15.05. 2024	13:00	16:48	36	0.22	27	21	new control for the three-way valve installed, oil sensor shutdown *OCH* (14:10)
16.05. 2024	15:27	16:54	40	0.24	27	23	need higher T, P and F to reach design conditions
21.05. 2024	14:15	16:51	45	0.22	28	25	error *OCH* data logging (14:17-14:30)
22.05. 2024	14:23	16:59	49	0.29	20	-	manual control of the three-way valve
23.05. 2024	14:09	16:31	32	0.26	26	23	design conditions were not reached
27.05. 2024	13:42	18:12	32	0.23	29	25	design conditions were not reached
05.06. 2024	15:25	17:35	32	0.22	20	18	hot gas shutdown (17:35), first day with new sink insulation
06.06. 2024	13:03	16:39	32	0.25	21	17	highest temperatures and pressures reached
07.06. 2024	11:48	13:00	32	0.21	27	25	data diverge over time, high suction gas superheating
10.06. 2024	14:33	17:21	32	0.23	33	30	manual compr. control (16:15-16:45), high suction gas superheating, only day with open ejector bypass

The heat map in Fig. 23 illustrates the most frequent operating conditions of the compressor during the whole measurement campaign. Most of the time, saturated suction gas temperature and condensing temperature were significantly lower than at the design conditions.

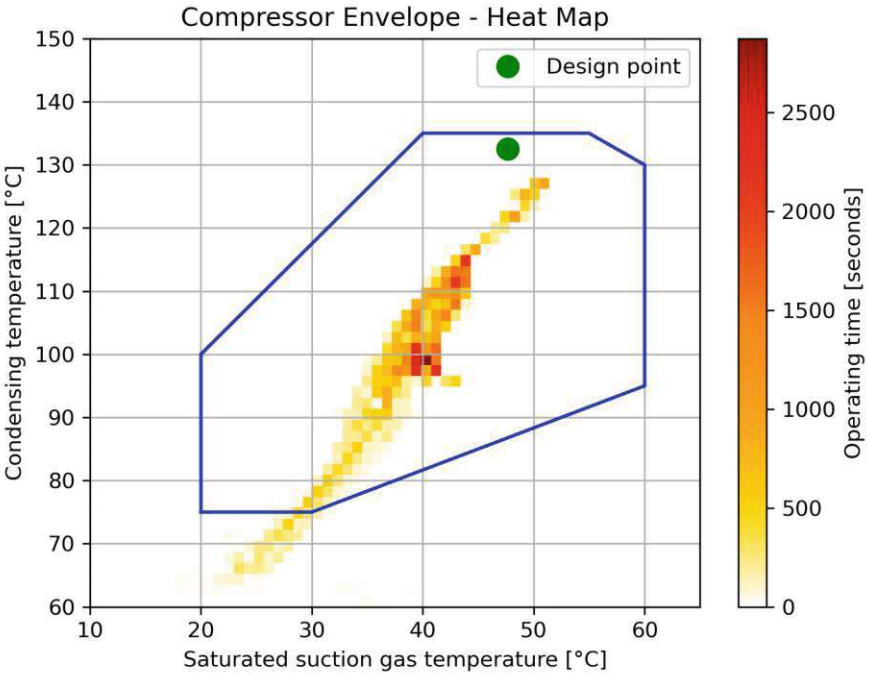

Figure 23: Overview of the operating conditions of the compressor. The light yellow area in the bottom left outside the compressor envelope is due to the startup process of the heat pump. (Created by the author.)

4.2 Standard Measurement Procedure

Fig. 24 shows selected data from June 5, 2024, which was a typical measurement day in regard to the heating behaviour of the heat pump. In order to reach the design conditions, the refrigerant was continuously heated up. However, at half past five when the heat pump was switched off, the pressure downstream of the condenser was still only about 14 bar instead of 20 bar.

In two of the pressure enthalpy diagrams in Fig. 24b the pressure lift performed by the

ejector is clearly visible. Fig. 24c shows how the different types of superheating[16] and subcooling[17] varied over time.

During the measurements, the electrical power consumption of the compressor (about 23.5 kW on June 5, 2024) was entered manually into the *OCH* log-file at irregular intervals. Usually, *OCH* reads the power consumption of the compressor for steady-state operating conditions only. During heating up and during transient phases, as with all measurements in this measurement campaign, the power consumption is not the primary focus, as relevant key figures such as the COP are normally only calculated for steady-state operating conditions. In the context of these measurements, however, this poses a problem because certain parameters such as the COP can only be determined at times when the electrical power consumption of the compressor is available. Due to the manual reading and irregular entry into the log file, the COP is furthermore subject to a temporal uncertainty that is difficult to quantify.

4.3 Semi-Steady-State Operation

Due to the continuous heating of the heat pump in the attempt to achieve the design conditions (about 20 bar refrigerant pressure and 150 °C at the inlet of the condenser), no steady-state conditions were reached during the measurements discussed in this thesis. This significantly complicates the evaluation of the data, as, for instance, energy balances over these non-steady-state periods must be interpreted with caution.

Nevertheless, this subsection aims to provide a brief overview of four semi-steady-state operating periods, which are described in Table 4. The observed variables were averaged for each period in order to minimise short-term fluctuations. The periods were selected on the basis of various characteristics, including the available power consumption of the compressor and the lowest possible fluctuation in the energy balance of the entire heat pump and individual components[18].

[16] The suction gas superheating, which is controlled automatically by the position of the three-way valve, is calculated from the temperature and pressure at the compressor inlet. The hot gas superheating corresponds to temperature and pressure of the refrigerant downstream of the compressor. The expansion valve automatically controls the superheating downstream of the evaporator, equivalent to the ejector suction nozzle.

[17] Three types of subcooling were studied: The subcooling at the condenser outlet was calculated using *AIT* sensors only, while the subcooling upstream of the motive nozzle of the ejector was calculated once from the temperature measured by *AIT* (T206) and once from the temperature measured by *OCH* (T106) due to the strong offset between the two temperature sensors.

[18] The superheating values were also taken into account: due to measurement uncertainties (see subsection 4.4), sometimes it appears as if there was, for instance, no hot gas superheating, which causes the pressure enthalpy diagram to become strangely distorted.

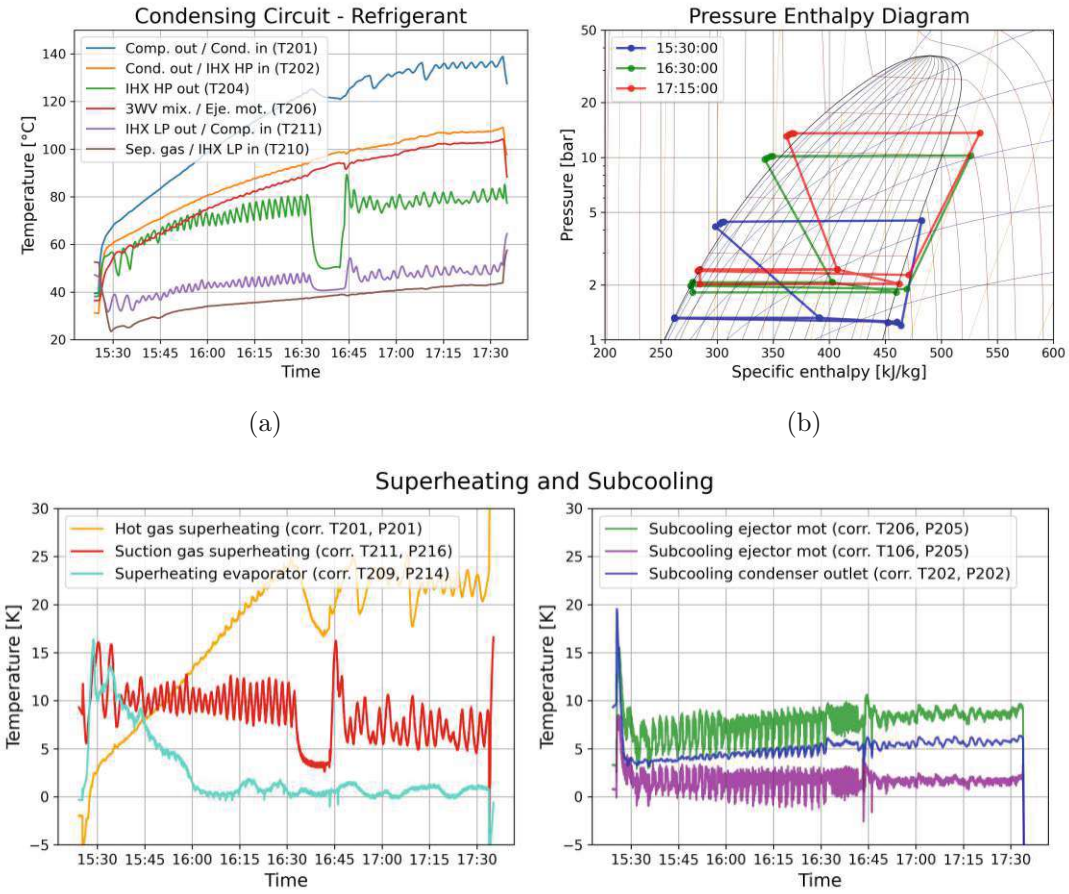

Figure 24: Typical measurement day: The temperatures and pressures slowly increase. Superheating and subcooling vary over time according to the automatic control of the three-way valve and the expansion valve. (Created by the author.)

4.3.1 Global Performance

Fig. 25 shows the averaged pressure enthalpy diagram of each of the four operating periods as well as the COP and the Carnot efficiencies. The error indicators in the bar chart visualise the range of the simple standard deviation, whereby the standard deviation only accounts for the fluctuations in the calculated values over the averaging period[19].

[19]The uncertainty of the measured values themselves, that is how precisely the COP is calculated by *OCH* at a certain point in time via the power consumption of the compressor and the sink side, is not included in the standard deviation shown here.

Table 4: Overview of the semi-steady-state periods analysed in this section. (Created by the author.)

Steady-State Period	**1**	**2**	**3**	**4**
Day	16.05.2024	27.05.2024	05.06.2024	10.06.2024
Start	16:30	15:30	17:15	17:00
Duration [min]	15	15	15	15
Compressor Electric Consumption [kW]	22.0	20.1	23.1	17.9
Heating Capacity [kW]	25.51 $\pm$ 0.79	27.03 $\pm$ 0.69	20.95 $\pm$ 1.46	32.82 $\pm$ 1.06

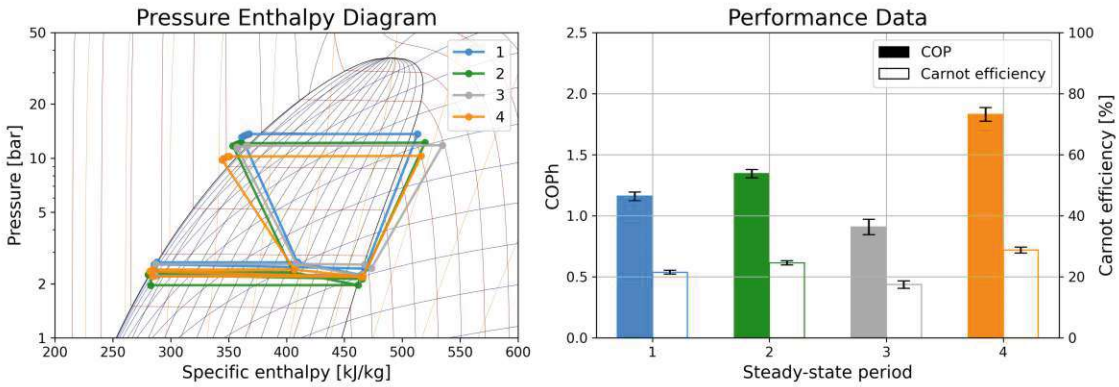

Figure 25: Pressure enthalpy diagram, COP and Carnot efficiency for the four semi-steady-state periods. (Created by the author.)

The total energy balance of the heat pump is estimated both in regard to the water-side and the refrigerant-side (see Fig. 26). On the water-side, the heat inflow consists of the heating capacity supplied to the heat pump via the water at the evaporator and the electrical power consumed by the compressor. The capacity supplied to the heat pump by the water in the evaporator is calculated as $\dot{W} = c_P \dot{m} \Delta T$ with the specific heat capacity at constant pressure c_P, the temperature difference over the evaporator ΔT (measured by OCH) and the mass flow rate $\dot{m} = \rho \dot{V}$, where ρ is the density of the water and $\dot{V}$ is the volume flow rate of the water (measured by OCH).

The outflow on the water-side is given by the heating capacity absorbed by the water at the condenser[20] and by how much heating capacity is released via the oil cooling system[21] that is integrated into the compressor.

On the refrigerant-side, the energy balance is calculated using the respective enthalpy differences ($\dot{W}_i = \Delta h_i \, \dot{m}_i$). The heat inflow consists of the heating capacity the refrigerant receives at the evaporator ($\dot{m}_{eva} = F202$) and the compressor ($\dot{m}_{comp} = F201$) and the outflow considers the heating capacity provided by the refrigerant at the condenser.

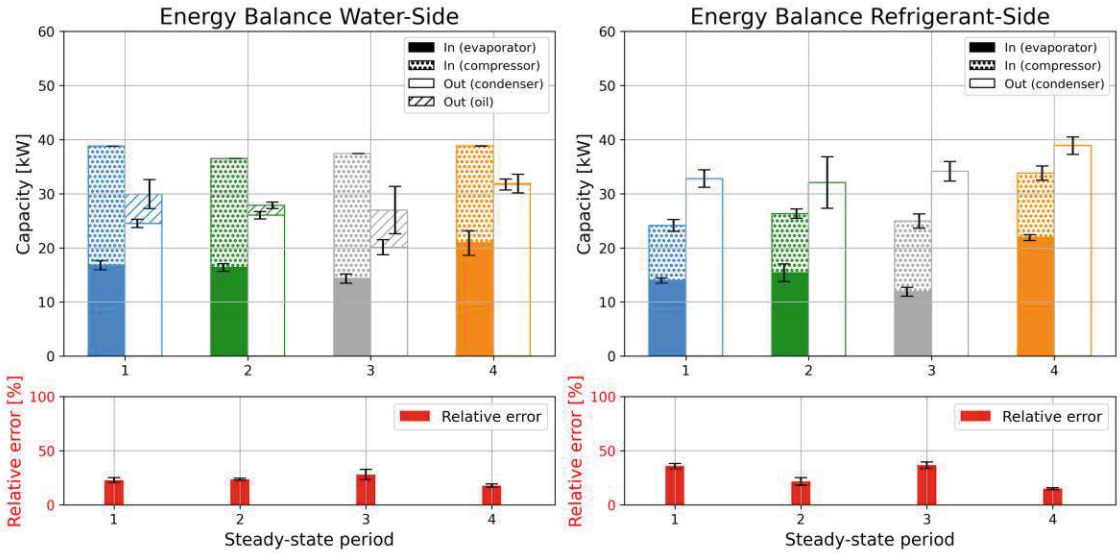

Figure 26: Total energy balance of the heat pump. The refrigerant-side is calculated using the enthalpy differences of the refrigerant at the evaporator, condenser and compressor, while the energy balance on the water-side takes the electrical power consumption of the compressor and the water temperatures and volume flow rates upstream and downstream of condenser and evaporator as well as the oil cooler into account. The relative error is calculated as $|\frac{E_{\text{in}} - E_{\text{out}}}{E_{\text{in}}}|$. (Created by the author.)

According to Fig. 26, on the water-side the energy input into the system is always larger than the output. This is plausible due to heat losses that are not considered in that energy balance. On the refrigerant-side, however, it appears as if the output was larger

[20] The heating capacity absorbed by the water at the condenser is calculated just as at the evaporator, only this time using the mass flow rate, the temperature difference and the specific heat capacity of the water at the evaporator.

[21] As the oil cooling repeatedly starts up and quickly stops again, it is difficult to calculate how much heating capacity it dissipates. A rough estimate is made using the time-fluctuating temperature difference between sensors T212 upstream and T116 downstream of the oil cooling, whereby the constant offset between these two sensors (see subsection 4.4) was subtracted beforehand.

than the energy input. Presumably, the heating capacity provided by the refrigerant in the condenser is calculated wrongly, due to the possibly erroneous assumption that the refrigerant condenses out completely in the condenser (see 4.3.4). If incomplete condensation is assumed, less heating capacity would be provided by the refrigerant, which would bring the energy balance more towards equilibrium.

4.3.2 Ejector

At five locations along the axis of the ejector, the pressure is measured with differential pressure sensors (P206-P210). Including pressure sensor P214 at the suction nozzle and P211 at the ejector outlet, the pressure profile inside the ejector can be visualised as shown on left side of Fig. 27. On the right side, the operating point of the ejector is depicted. In the selected semi-steady-state periods, the ejector lifts the pressure of the suction flow by about 10 to 20 %. A suction flow of up to half of the mass flow rate of the motive flow can be entrained by the motive flow.

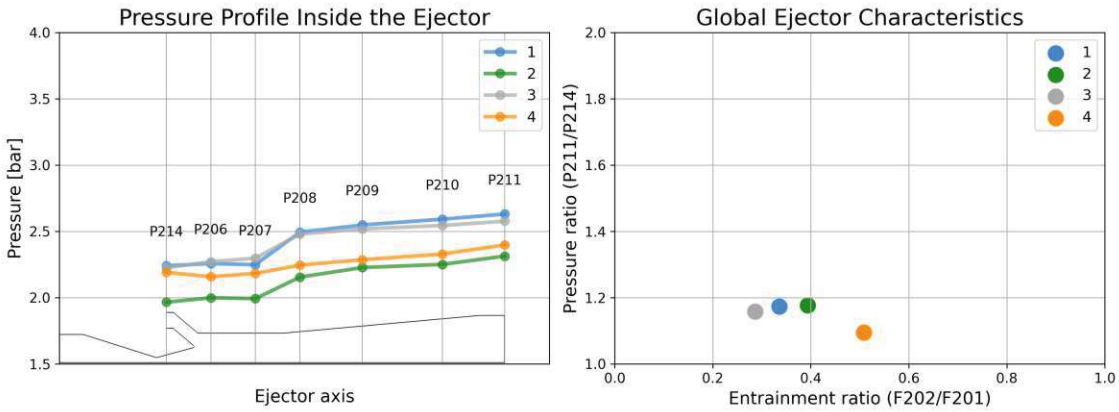

Figure 27: The pressure is measured along the axis of the ejector. Entrainment and pressure ratio characterise the performance of the ejector. (Created by the author.)

The vapour quality at the outlet of the ejector is not measured, but it can be estimated by comparing the enthalpy flow into the ejector with the enthalpy flow at the ejector outlet. On May 22, 2024, for instance, a vapour quality of about 0.55 fits the data well[22] (see Fig. 28).

[22]The vapour quality at the ejector outlet varies with time. By assuming $x = 0.55$, the enthalpy flow into the ejector is sometimes larger and sometimes smaller than the outflow, which is why this specific vapour quality was chosen as a representative example.

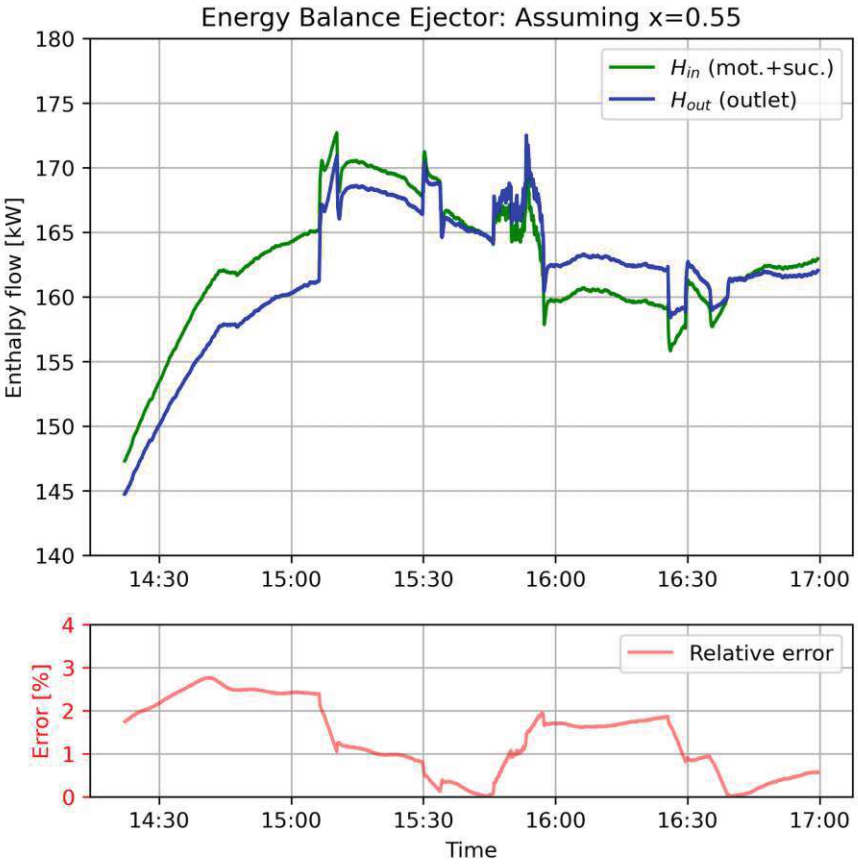

Figure 28: On May 22, 2024, assuming a vapour quality of 0.55 at the outlet, the enthalpy flow into the ejector (motive and suction nozzle) almost matches the enthalpy flow at the outlet of the ejector. The relative error is calculated as $|\frac{H_{\text{in}}-H_{\text{out}}}{H_{\text{in}}}|$. (Created by the author.)

4.3.3 Compressor

To analyse the performance of the compressor, three different efficiencies were calculated:

1. The volumetric compressor efficiency refers to the ratio of the actual volume of refrigerant compressed compared to the intake volume of the compressor under

ideal operating conditions[23].

2. The isentropic compressor efficiency is the ratio of the work required in an ideal isentropic process to the actual work required to compress the refrigerant, indicating the compressor's effectiveness in performing the compression with minimal energy losses. The actual work required for compression is calculated using the enthalpy difference of the refrigerant upstream and downstream of the compressor.

3. To calculate the effective isentropic efficiency, the work required in an ideal isentropic process is divided by the actual power consumption of the compressor - instead of using the enthalpy difference of the refrigerant - to account for the energy losses that occur when electrical energy is converted into mechanical work for compression.

In Fig. 29, these three compressor efficiencies as well as the operating points of the compressor inside the compressor envelope are displayed respectively for the semi-steady-state periods. The volumetric efficiency is only about 50 %, indicating that the compressor's delivery volume is only about half as large as it should be. The low effective isentropic efficiency shows that the compressors is not effectively converting the input energy into increased pressure of the refrigerant.

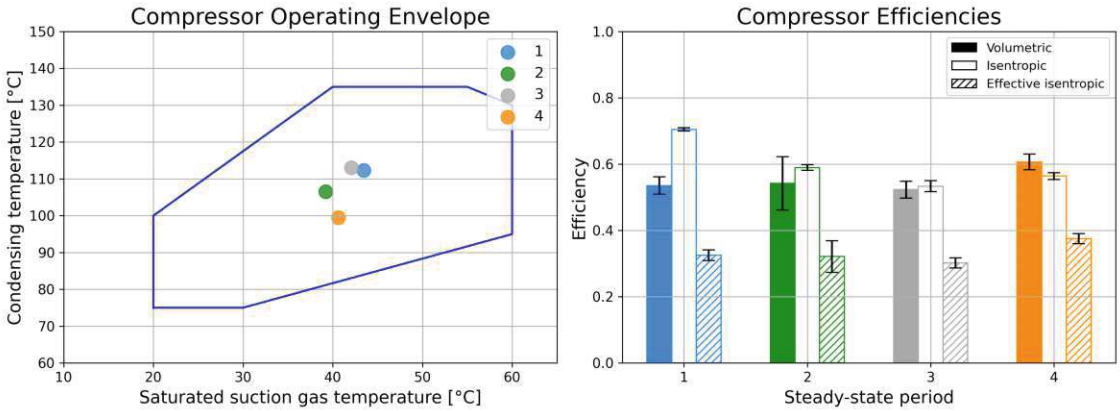

Figure 29: On the left, the operating points of the semi-steady-state periods are displayed in the compressor operating envelope. On the right, the volumetric, isentropic and effective isentropic compressor efficiencies are plotted. (Created by the author.)

[23]The ideal volume flow rate through the compressor was always assumed to be 118 m^3/h, corresponding to the maximum power input of the compressor. Consequently, the volumetric efficiency is only accurate for 100 % compressor capacity and should be disregarded during the process of starting the heat pump or when the power consumption of the compressor is adjusted manually.

The energy balance of the compressor is shown in Fig. 30. The compressor receives electrical energy that is either converted to mechanical energy for compressing the refrigerant or dissipated by the oil cooler.

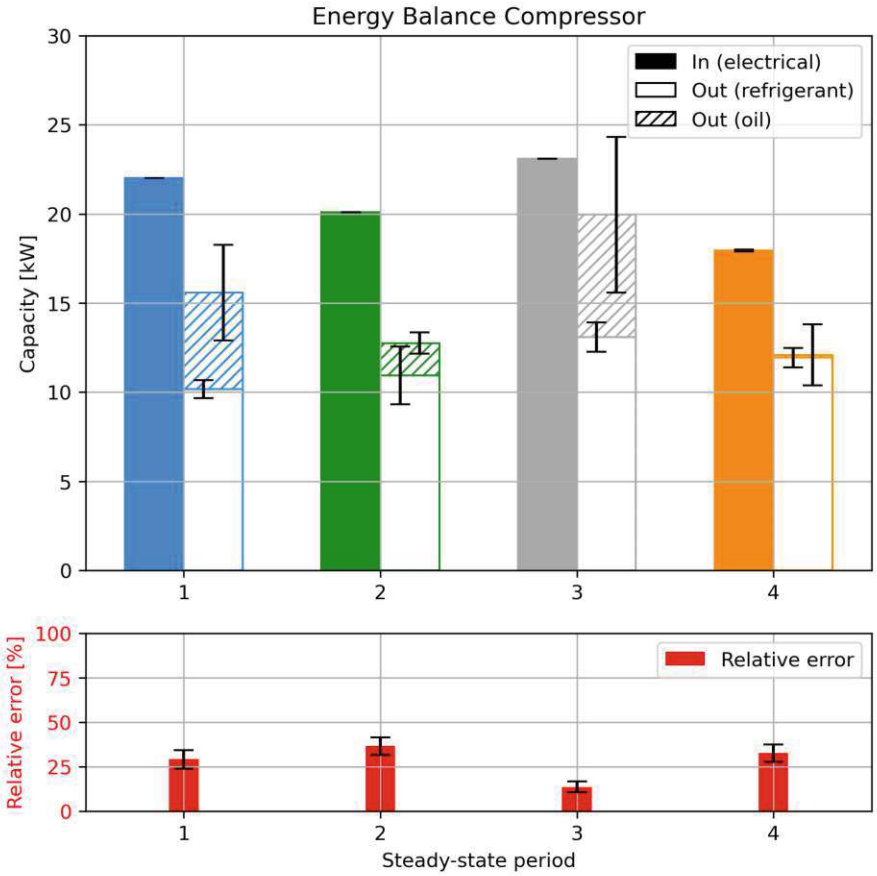

Figure 30: The electrical power consumption of the compressor is compared with the heating capacity absorbed by the refrigerant and the heating capacity dissipated by the oil cooler. The relative error is calculated as $|\frac{E_{\text{refr+oil}} - E_{\text{el}}}{E_{\text{refr+oil}}}|$. (Created by the author.)

4.3.4 Heat Exchangers

Condenser, evaporator and IHX play a crucial role in the refrigerant circuit. The energy balance of the evaporator is shown in Fig. 31, of the condenser in Fig. 32a. Both energy balances are not in equilibrium, however, while in the evaporator the heating capacity supplied by the water is not much larger than the heating capacity received by the refrigerant, the energy balance of the condenser is more out of balance.

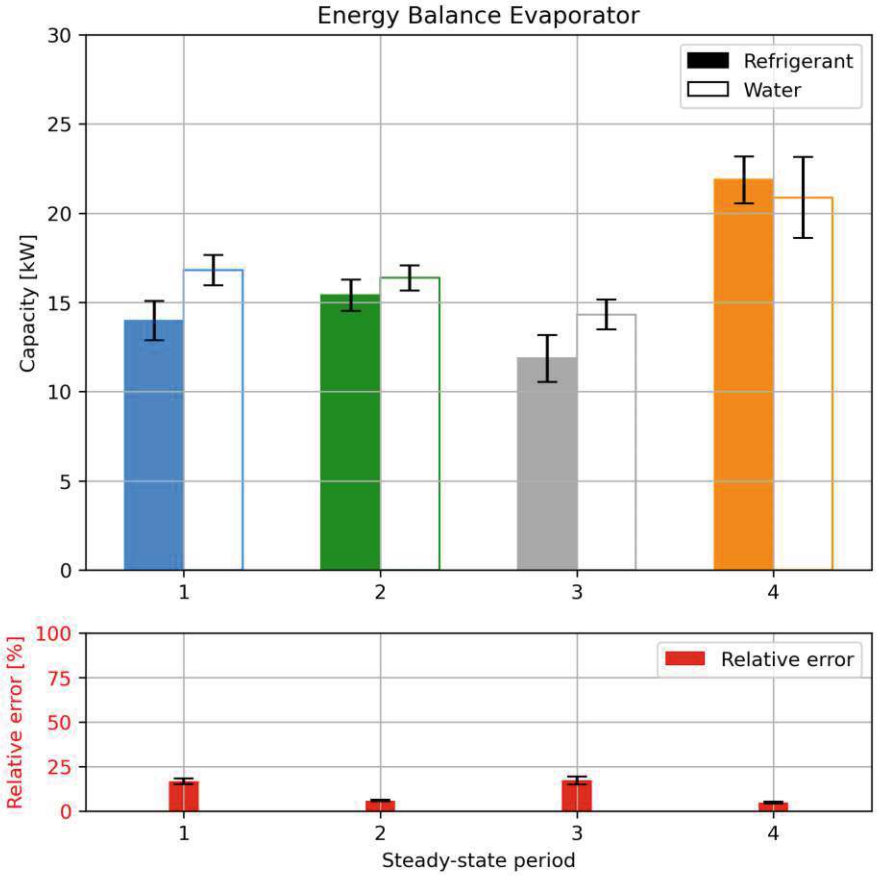

Figure 31: During most measurement days, including the selected semi-steady-state periods, the energy balance of the evaporator is approximately in equilibrium. The relative error is calculated as $|\frac{E_{\text{water}} - E_{\text{refr}}}{E_{\text{water}}}|$. (Created by the author.)

It appears that the condensing refrigerant releases significantly more heat than the water in the condenser absorbs (see Fig. 32a). This imbalance can be resolved by either assuming that the heat transfer in the condenser is very inefficient or that the refrigerant in the condenser does not fully condense, but exits the condenser in a two-phase state as

visualised in Fig. 32b, using the measurements from May 16, 2024, as an example.

The energy balance of the IHX is shown in Fig. 33a. Through calculating the enthalpy difference of the refrigerant at the IHX both on the high-pressure side downstream of the condenser and on the low-pressure upstream of the compressor, valuable insights into the heat transfer over the IHX can be gained. Mostly, the high-pressure side seems to provide less heat than the low-pressure side absorbs. By assuming that on the low-pressure side two-phase refrigerant enters the IHX of which about 0.5 % evaporates in the IHX[24], the relative error between high and low-pressure side decreases. For measurements where the high-pressure side of the IHX provides significantly more energy than the low-pressure side receives, post-condensation on the high-pressure side could be assumed[25].

[24] The enthalpy differences on both the high-pressure and the low-pressure side were both calculated using the pressures and temperatures upstream and downstream of the IHX. Changes in the vapour quality were not considered, so if post-condensation on the high-pressure or post-evaporation on the low-pressure side took place, it was not accounted for in the energy balance shown in Fig. 33a.

[25] For the sake of completeness, post-evaporation on the low-pressure and post-condensation on the high-pressure side could also take place simultaneously. Usually, the measured temperature and pressure values define, whether the refrigerant is in a liquid, gaseous or two-phase state. However, as discussed in subsection 4.4, the temperature values that we measured appear to have a large offset to the actual temperatures in the refrigerant circuit. Because of this reason and also taking into account that the vapour quality was not measured at any point within the refrigerant circuit, with the measurement data available the energy balance of the IHX still leaves room for speculation.

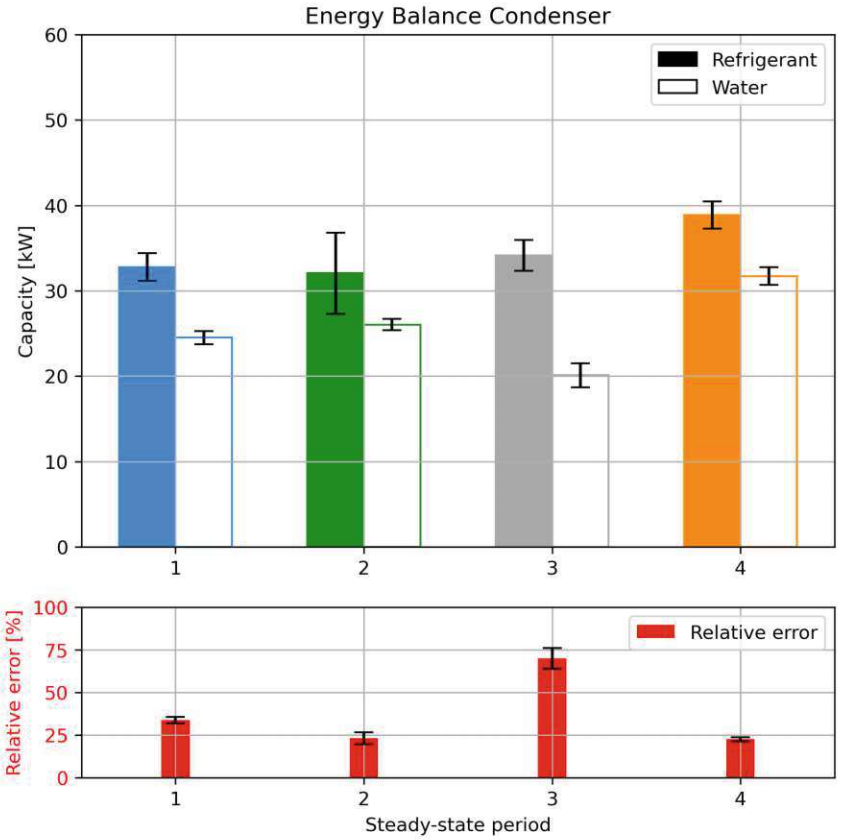

(a) Energy balance condenser

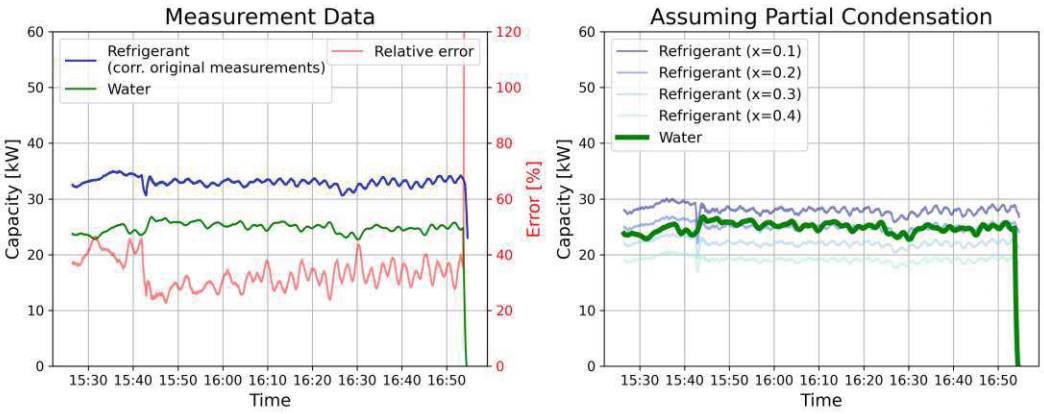

(b) Complete (measurement data) versus incomplete condensation (assumption)

Figure 32: (a) Comparison of the energy supplied by the refrigerant and received by the water in the condenser.
(b) On May 16, 2024, assuming that the refrigerant does not fully condense in the condenser, but a vapour quality of $x > 0$ still remains, improves the energy balance of the condenser significantly. The relative error is calculated as $|\frac{E_{\text{water}} - E_{\text{refr}}}{E_{\text{water}}}|$. (Created by the author.)

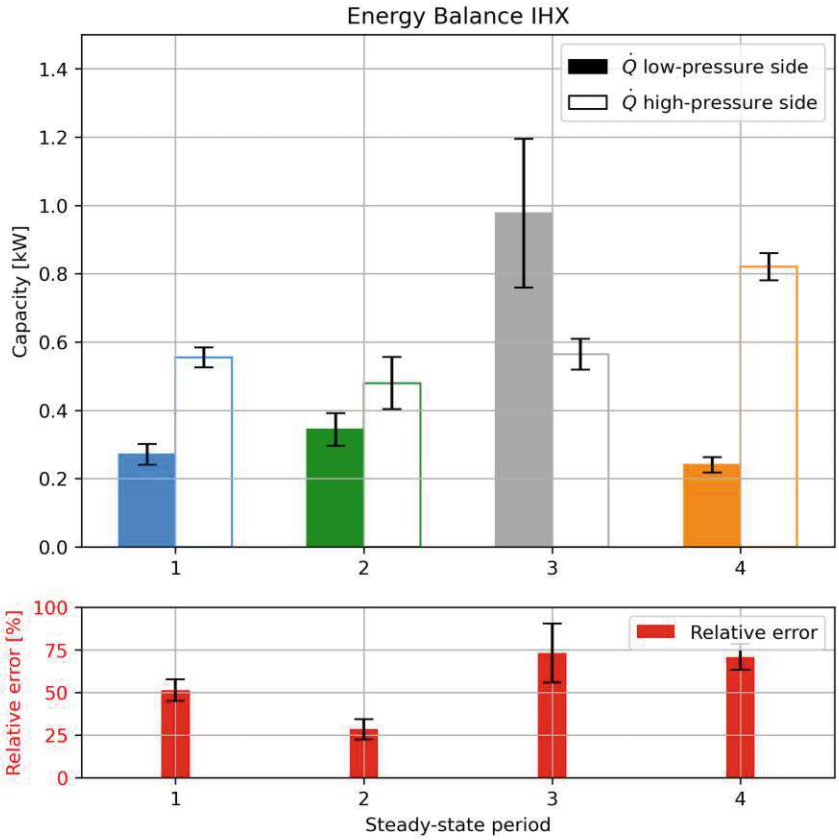

(a) Energy balance IHX

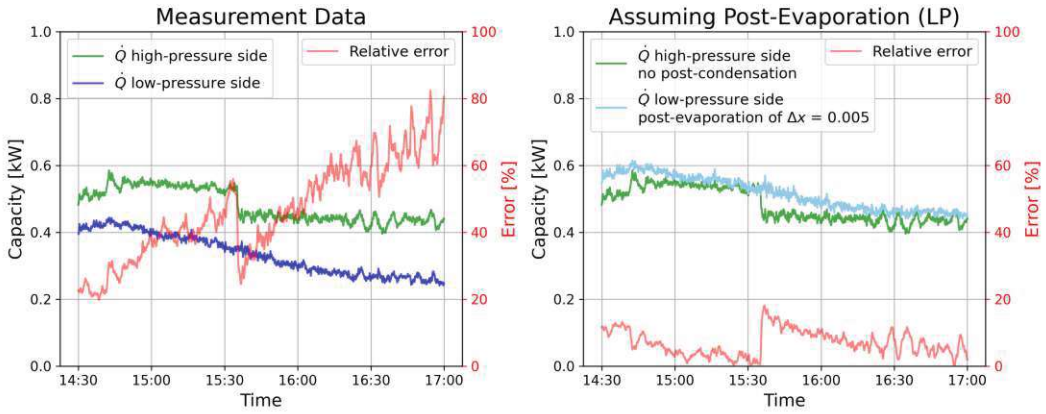

(b) Without (measurement data) versus with post-evaporation on the low pressure side (assumption)

Figure 33: If a post-evaporation of $\Delta x = 0.005$ is assumed on the low-pressure side of the IHX, on May 27, 2024, the energy balance improves. This indicates that on this day a small amount of liquid refrigerant from the separator was post-evaporating in the IHX. The relative error is calculated as $|\frac{\dot{Q}_{\mathrm{LP}} - \dot{Q}_{\mathrm{HP}}}{\dot{Q}_{\mathrm{LP}}}|$. (Created by the author.)

4.4 Measurement Errors and Uncertainties

The temperatures measured by *AIT* and *OCH* sensors differ strongly. Fig. 34 visualises the offset between two temperature sensors respectively which are located almost at the same positions on the heat pump. For most sensors, there appears to be an almost constant offset of about 5 K throughout the whole measurement day.

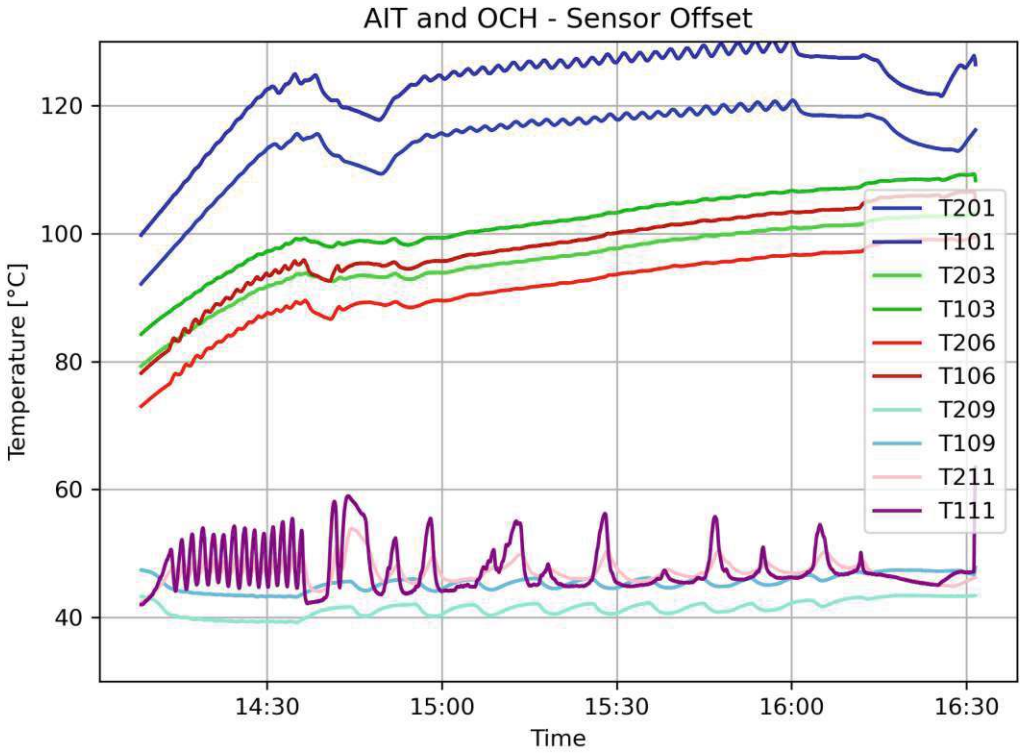

Figure 34: Sensor offset between *AIT* and *OCH* sensors on May 23, 2024. Almost all *OCH* sensors measure a higher temperature than the sensors from *AIT*. (Created by the author.)

An explanation for this effect might be, that the *OCH* sensors have lost calibration and measure about 5 K more than they should. While all the *AIT* temperature sensors were newly calibrated directly before the measurement campaign, according to *OCH*, their temperature sensors had not been re-calibrated for a longer time span of about one to three years.

Temperature sensors in immersive sleeves measure the temperature more accurately than thermal contact sensors. For instance, the temperatures measured by sensor T111 from *OCH* and T211 from *AIT* in Fig. 34 show this effect[26]. Sensor T111 is in an immersive sleeve and, therefore, adapts more quickly to temperature changes compared to the pipe contact sensor T211. Also, the rather thin *Armaflex* insulation on the pipes of the heat pump might not be ideally suitably for high-temperature applications and the installation of the pipe contact sensors using a conductive metal adhesive tape might not have provided the best thermal contact in comparison to immersive sleeves, which is why pipe contact sensors might systematically measure a lower temperature than the temperature sensors in immersive sleeves.

The following considerations determined how the measurement errors and uncertainties were evaluated and quantified within this thesis:

- There was no information available regarding the measurement uncertainties of the *OCH* sensors (temperature, volume flow, pressure). The results of these sensors, however, were used by *OCH* to calculate the COP and the heating capacity.

- The manual entry of the electrical power consumption of the compressor at irregular time intervals creates a temporal measurement uncertainty, which is difficult to quantify.

- Although the *AIT* pipe contact temperature sensors were newly calibrated before the measurements, as they only measure the surface temperature of the pipe, which seems to significantly differ from the refrigerant's temperature, their offset to the refrigerant's actual temperature is much larger than the measurement uncertainty of the sensors themselves.

As a results, it was decided to only calculate measurement uncertainties as well as error propagation for selected evaluations by applying a simplified method. This method is discussed below using the energy balance of the compressor for one semi-steady-state period (see Fig. 30) as a representative example.

1. For the duration of the semi-steady-state period, three arrays are created, which contain the power consumption of the compressor ("in"), the energy received by the refrigerant at the compressor ("out") and the energy dissipated by the oil cooler for each second ("out"). No measurement errors or uncertainties are considered up to this point.

[26] In Fig. 34, T111 from *OCH* and T211 from *AIT* do not have a large measurement offset relative to each other, compared to the other sensor pairs depicted in this figure. Either T111 is still well calibrated or it measures a smaller temperature than it should which cancels out with the higher temperature inside the immersive sleeve in comparison to the surface temperature of the pipe.

2. Then, the mean value and the standard deviation of the arrays are calculated and displayed using the error bars in the upper part of Fig. 30.

3. The standard deviation of the total heat outflow $\sigma_{E_{\text{out}}}$ was calculated according to Eq. 21 with σ_{refr} being the standard deviation of the refrigerant-array and σ_{oil} the standard deviation of the oil cooler-array.

$$\sigma_{E_{\text{out}}} = \sqrt{\sigma_{\text{refr}}^2 + \sigma_{\text{oil}}^2} \tag{21}$$

4. Finally, the standard deviation of the relative error $rr_{\text{rel}} = \frac{E_{\text{out}} - E_{\text{in}}}{E_{\text{out}}}$ was calculated using Eq. 22 and displayed with the error bar in the lower part of Fig. 30.

$$\sigma_{rr_{\text{rel}}} = rr_{\text{rel}} \sqrt{(\frac{\sigma_{E_{\text{in}}}}{E_{\text{in}}})^2 + (\frac{\sigma_{E_{\text{out}}}}{E_{\text{out}}})^2} \tag{22}$$

This simplified method provides an overview of the measurement uncertainties of the examined parameters within the semi-steady-state periods. It is sufficiently suitable for the analysis conducted within this thesis, especially as the data shown here are primarily intended to provide important qualitative findings to develop suggestions for improvements for future measurements rather than to precisely determine the exact efficiency of this heat pump prototype.

5 Comparison of the Experimental Results with the Design Conditions

This section draws a comparison between the results of the measurements and the simulated design point of the heat pump. It is analysed why the performance of the heat pump differs from the expected performance and suggestions for improvements and adaptions for the next measurements are discussed.

5.1 Refrigerant Mass Flow

At the design point, the refrigerant mass flow rate is expected to be 0.438 kg/s in the condensing and 0.209 kg/s in the evaporating circuit. On the one hand, the mass flow rate in the condensing circuit is essential to generate the desired heating capacity at the condenser. On the other hand, as the condenser mass flow corresponds to the ejector's motive flow, it should enable the proper entrainment of the suction flow into the ejector, thus establishing the mass flow in the evaporating circuit.

Throughout the measurements discussed in this thesis, the mass flow rates were significantly lower than expected, with the condenser mass flow rate mostly in the range of 0.2 to 0.3 kg/s and the mass flow rate over the evaporator often even lower than 0.1 kg/s.

Using to the compressor manufacturer data from *SRMTEC*, it was examined how the compressor should behave depending on the refrigerant's temperature and pressure upstream and downstream of the compressor as well as the electrical power consumption. Even after intensive discussion together with *OCH*, no compressor-related explanation was found as to why the swept volume of the compressor was mostly only half the expected amount, despite the expected power consumption according to the design conditions of the compressor.

5.2 Heating Capacity and Heat Losses

The heating capacity of the heat pump was designed to be about 60 kW, however, only half of the desired heating capacity was measured due to the low refrigerant mass flow in the condenser.

In order to reach a high sink temperature, the heat pump itself has to continuously heat up the sink water. Due to the low heating capacity, the process of heating up the sink took a long time, which is why the design temperatures on the high-pressure side were never reached during the measurements.

Also, the combination of a high sink temperature and a small heating capacity caused heat losses at the water-side of the sink to play a dominant role and slow down the warm-up process of the sink water even more. To minimise the heat losses over the water-side of the sink, between May 27, 2024, and June 5, 2024, *OCH* insulated some pipes on the water-side of the sink. However, among other pipes and valves, the flexible hoses between the heat pump and the *OCH* test rig remained uninsulated.

By examining the energy balance at the condenser after the insulation on the water-side of the sink had been applied, the heat losses still appeared to be about 7 kW. Nevertheless, a rough estimate conducted later yield that heat losses (radiation and convection) over the flexible hoses should only be about 1.5 kW:

The radiation losses were estimated using Stefan-Boltzmann's law $\dot{Q}_{\text{rad}} = \epsilon\,\sigma\,A\,(T_1^4 - T_2^4)$, with the Stefan-Boltzmann constant $\sigma = 5.67 \cdot 10^{-8}\ \text{W/m}^2\text{K}^4$. Assuming a surface temperature of the flexible hoses of $T_1 = 100\,°\text{C} = 373.15\,\text{K}$ and of the surrounding room of $T_2 = 25\,°\text{C} = 298.15\,\text{K}$, an emissivity ϵ of 0.7 and a surface area $A = 2\,r\,\pi\,L = 2\,0.05\,\text{m}\,\pi\,4\,\text{m} = 1.257\,\text{m}^2$, with radius r and length L of the hoses, the radiation losses are about 0.57 kW.

The heat losses caused by convection were estimated using the formula $\dot{Q}_{\text{conv}} = h_t\,A\,\Delta T$, with a heat transfer coefficient h_t of $10\,\text{W/m}^2\text{K}$, the same surface area $A = 1.257\,\text{m}^2$ and a temperature difference ΔT of 75 K, which yields about 0.94 kW.

Because of this imbalance between the measured and the calculated heat losses, it was considered whether it could be that instead the refrigerant does not completely condense in the condenser (see Fig. 32b).

5.3 Refrigerant Charge

According to the simulations, which did not take into account the piping, the sensors, the valves and the volume of the compressor, the optimal refrigerant charge was expected to be 36 kg.

The influence of varying refrigerant charge on condenser mass flow, heating capacity and COP is shown in Fig. 35. With 49 kg, a low heating capacity of only about 20 kW was observed, which prompted the reduction of the refrigerant charge directly to 32 kg. However, as even for the same refrigerant charge of 32 kg, the heating capacity varies strongly from day to day, the low heating capacity measured with 49 kg could just have been an outlier. The mass flow rate with 49 kg, however, was significantly larger than during all the other measurement days.

Retrospectively it might not have been necessary to decrease the refrigerant charge from 49 kg on May 22, 2024, to 32 kg on May 23, 2024, but instead more time could have been spent maintaining 49 kg and varying other parameters, like suction gas superheating or the water temperatures, instead. Due to the higher mass flow rate with 49 kg, it can be recommended to investigate the effect of an even higher refrigerant charge in future measurements.

The filling level in the separator was not continuously logged, but it appeared as if usually about half of the separator was filled with liquid refrigerant except for the measurement day with 49 kg where the filling level was almost 80 %. Therefore, if a refrigerant charge higher than 49 kg is tested, the filling level in the separator should be monitored even more carefully in order to prevent the compressor from liquid slugging.

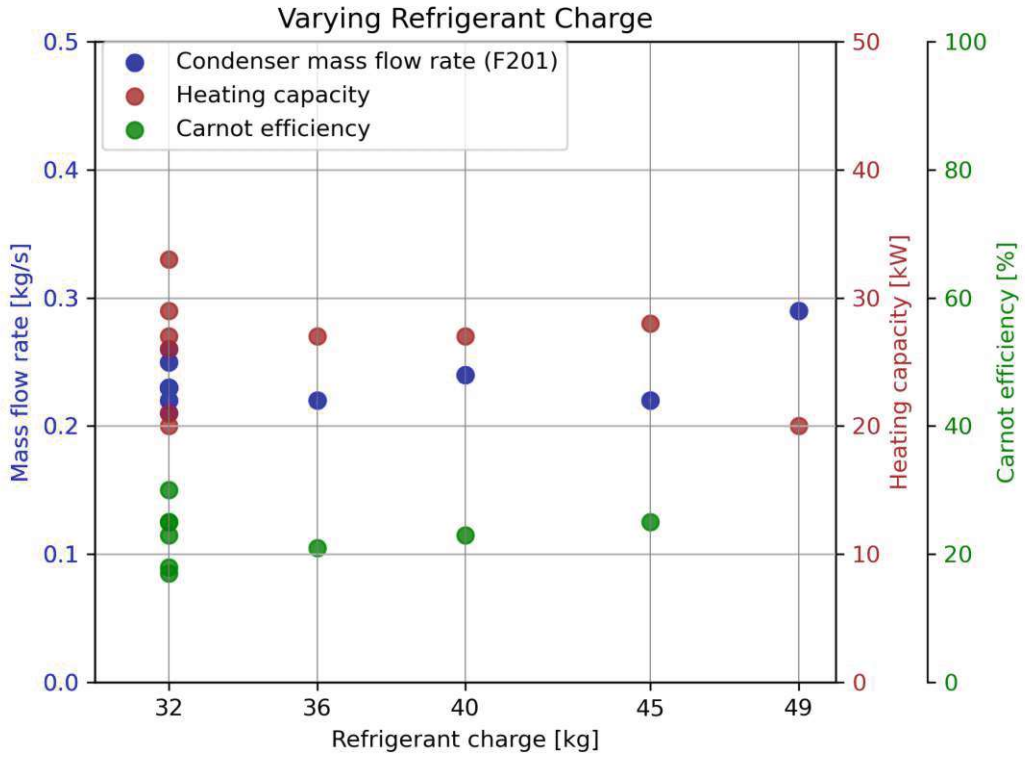

Figure 35: Impact of varying refrigerant charge on condenser mass flow, heating capacity and COP. The effect of a higher refrigerant charge might be worth investigating, despite the low heating capacity observed during the measurements with 49 kg. (Created by the author.)

5.4 Bubble Formation

There are sight glasses at five different locations within the refrigerant circuit: one upstream of the three-way valve, one between separator and IHX, one between separator and expansion valve, one between the evaporator and the ejector's suction nozzle and the especially large sight glass right upstream of the motive nozzle of the ejector. If bubble formation in visible in a sight glass, this indicates that the refrigerant is in a two-phase state at the location of the sight glass. Ideally, during operating of the heat pump only liquid refrigerant should be visible in all sight glasses except for the sight glass between separator and IHX, where only gaseous refrigerant should be present.

Figure 36: Although the pressures and temperatures mostly indicated subcooling at the motive nozzle of the ejector, in the sight glass upstream of the motive nozzle turbulent two-phase flow was visible. (Pictures taken by *OCH* and the author.)

During the measurements, however, most of the time many sight glasses displayed mild to severe bubble formation, except for the sight glass between separator and expansion valve, where mostly no bubble formation was visible. For example, although the temperature and pressure readings at the motive nozzle of the ejector indicated subcooling, which states that the refrigerant is fully liquid, the bubble formation in the large sight glass upstream of the motive nozzle showed a two-phase state, as visible in Fig. 36.

The mass flow meter upstream of the motive nozzle confirmed these observations by displaying a "severe two-phase warning". Initially, it was assumed that there was something wrong with the mass flow sensor and the warning was ignored. However, in combination with the energy balance of the condenser indicating incomplete condensation and the two-phase refrigerant in the sight glasses, the two-phase warning was subsequently classified as an important indicator.

As a result, considering the large measurement uncertainties of the temperature measurements (see subsection 4.4), it was decided to rather trust the sight glasses, the energy balance at the condenser (including the unexpectedly low heating capacity) and the two-phase warning instead of the measured subcooling.

Another challenge encountered during the measurements was that the suction gas superheating was difficult to control with the three-way valve. When the pressure drop in one path downstream of a valve is significantly higher than in the other path, this affects the proper distribution of the mass flow. Throughout most of the adjustment range of the three-way valve, there was almost no change in the distribution of the mass flow through its branches However, within a small adjustment range, for example between 79 and 80 %, there were significant differences in the distribution of the mass flow. Presumably, the missing control authority of the three-way valve was caused by two-phase refrigerant in the valve and the IHX, which increased the pressure drop at the IHX and thus led to a limited control range where the three-way valve could effectively regulate the flow.

5.5 Ejector Performance

Fig. 37 displays the simulated entrainment and pressure ratio as well as the pressure profile inside the ejector at the design conditions[27]. Ideally, the suction pressure should be lifted by almost 40 % at a suction mass flow rate of approximately half of the mass flow rate of the motive flow.

[27] The design conditions were not simulated within this thesis. Earlier during the course of the *ETHP* project, simulations regarding the whole refrigerant circuit were conducted in *Dymola* as well as separate simulations using *Ansys Fluent* that focused solely on the ejector. The pressure profile inside the ejector (P206 to P210) was plotted according to the ejector-simulations. The pressure value at the suction nozzle (P214) and the outlet (P211) were taken from the *Dymola* simulations and corrected by an offset to better fit the pressure values inside the ejector.

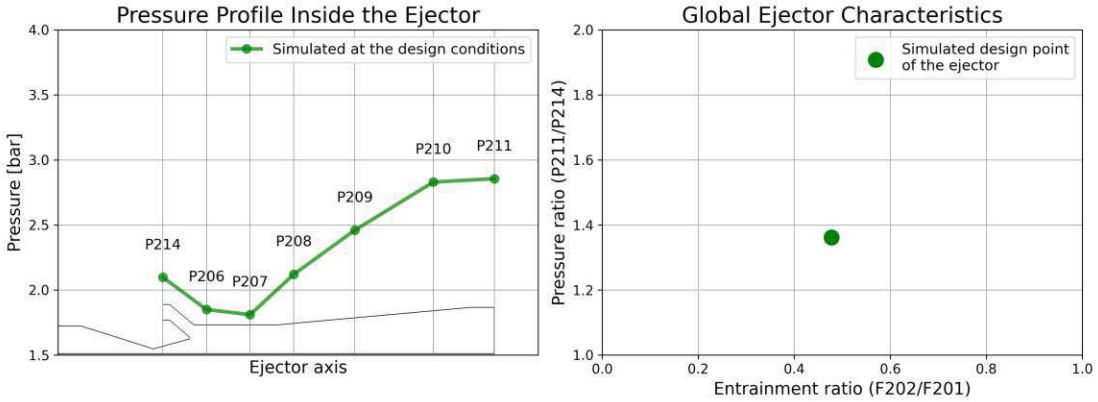

Figure 37: The simulations of the pressure profile inside the ejector, as well as the entrainment and pressure ratio at the design conditions, showed much better ejector performance than the initial measurement data from the first measurement campaign. (Created by the author.)

While during some measurements the measured entrainment ratio was close to the simulated one, the ejector only managed to create about half of the the simulated pressure lift because the diffuser did not seem to work properly. After intensive discussions and considerations, it was concluded that this was mainly due to the following three reasons:

1. The ejector was not operated at its design conditions. During the measurements, both the pressure and the mass flow rate at the motive nozzle were lower than at the design point.

2. In the large sight glass upstream of the motive nozzle, turbulent flow was visible, leading to the motive nozzle not being uniformly supplied with liquid refrigerant.

3. Refrigerant was entering the motive nozzle of the ejector in a two-phase state. Due to the higher density of the two-phase refrigerant compared to only liquid refrigerant, the maximum mass flow rate through the ejector was reduced[28].

Presumably, these reasons prevented the desired fluid velocities inside the ejector, including the ultrasonic conditions at the converging-diverging nozzle, from being reached

[28]The critical or maximum mass flow rate $\dot{m}_{\max}$ through the ejector was calculated by other members of the research group depending on the vapour quality. For a vapour quality of $x = 0$, the maximum mass flow was $\dot{m}_{\max}(x = 0) = 0.7232\,\mathrm{kg/s}$. With increasing vapour quality, $\dot{m}_{\max}$ decreases: $\dot{m}_{\max}(0.05) = 0.5178\,\mathrm{kg/s}$, $\dot{m}_{\max}(0.01) = 0.4233\,\mathrm{kg/s}$ and $\dot{m}_{\max}(1) = 0.1466\,\mathrm{kg/s}$. Although the specified maximum mass flow rates were only interpolated for a vapour quality of $0 < x < 1$, the dependency is clearly evident.

and the desired pressure lift was reduced. To improve the performance of the ejector, the large sight glass at the motive nozzle could be replaced with a pipe section to ensure uniform inflow into the ejector. Additionally, fully liquid refrigerant must enter the motive nozzle to enable a higher mass flow rate and the design conditions, especially the pressure of 20 bar at the motive nozzle, must be achieved.

The bypass of the ejector was designed to relief the ejector at high mass flow rates, by redirecting part of the suction flow directly to the end of the mixing zone. Due to the reduced suction flow in comparison to the design point, the bypass did not play an important role during the measurement campaign discussed in this thesis. Examining its effect will present an intriguing challenge in future measurements, once the dedicated mass flow rates have been established.

In summary, since the design conditions of the ejector, including pressure, mass flow rates and fully liquid and homogeneous refrigerant inflow into the motive nozzle, were not achieved, the ejector did not yet deliver significant improvements to the efficiency of the heat pump. However, the results provided valuable insights for preparing the next measurements with both this industrial high-temperature ejector heat pump and ejector heat pumps in general.

6 Conclusion and Suggested Changes

During the measurement campaign discussed in this diploma thesis, a prototype of an industrial high-temperature ejector heat pump was tested. Because of various experimental challenges, a heating capacity of only about 30 kW instead of 60 kW was achieved, which slowed down the process of heating up the heat pump and, in turn, lead to the design conditions not being reached at about 20 bar on the high-pressure side, a hot gas temperature of about 150 °C and a mass flow rate in the condensing circuit of approximately 0.438 kg/s. As a result, the ejector did not yet cause a significant improvement of the heat pump performance, necessitating further measurements.

Presumably, the refrigerant did not fully condense in the condenser leading to two-phase refrigerant in the three-way valve upstream of the IHX, which compromises the valve's control authority and makes precise control of the suction gas superheating difficult. Also, when the refrigerant enters the motive nozzle of the ejector in this two-phase state, the maximum mass flow rate through the motive nozzle and thus in the whole condensing circuit is reduced to only about half of the desired value. This also causes the observed reduction of the heating capacity of the heat pump. In addition, the ejector did not provide the desired pressure lift due to the unfavorable combination of the motive mass flow rate being too low, the refrigerant being in two-phase conditions at the motive nozzle and the lower inlet pressure at the motive nozzle compared to the design conditions.

The heat pump itself had to provide the heating capacity to warm up the sink to the desired temperature. This process of heating up the heat pump took many hours due to not only the reduced heating capacity but also large heat losses from the uninsulated water-side of the sink. Usually, the *OCH* test rig hosts heat pumps with heating capacities of up to 500 kW that are often not designed for high-temperature applications. In contrast, the prior experience with heat pumps like this one, combining a comparably small heating capacity with the high sink temperature of about 130 °C, was not extensive and the test rig not too well suited for the *ETHP* heat pump.

To improve the *OCH* test rig with regard to the *ETHP* heat pump, the heat losses were already slightly reduced by partly applying an insulation on the water-side of the sink. To further decrease the heat losses, the flexible hoses between the heat pump and the *OCH* test rig could also be insulated, which, in turn, would speed up the process of heating up the heat pump to better reach the design conditions within the available measurement time.

In order to ensure complete condensation of the refrigerant in the condenser, the temperature spread of the water inlet and outlet temperature on the sink side could be increased[29], and the thermal insulation on the liquid line[30] could be removed to enlarge the heat losses upstream of the motive nozzle of the ejector in order to guarantee that the motive nozzle is subjected to pure liquid refrigerant. In turn, this would increase the maximum mass flow rate through the ejector, and thereby the performance of the compressor and the heating capacity of the heat pump.

Replacing the large sight glass upstream of the motive nozzle of the ejector with a pipe would ensure a more even and less turbulent inflow into the motive nozzle. In addition, if the design conditions regarding pressure and mass flow rates are successfully met, the performance of the ejector is expected to improve.

Moreover, should the control authority of the three-way valve not be reestablished once pure liquid refrigerant enters the valve, a throttle valve could be installed on the branch without the IHX to manually equalise the pressure drop in both branches. To be independent from the performance of the IHX, an electrical heating tape could also be applied on the suction line upstream of the compressor to manually regulate the suction gas superheating.

The temperatures measured by the *OCH* sensors differ from the temperatures measured by *AIT* sensors. Before the next measurement campaign, therefore, it would be recommendable to recalibrate the *OCH* sensors to get more precise measurement data or to better understand the effect of different mounting options of the temperature sensors. In addition, the water temperature of the source and the sink could also be measured with *AIT* sensors for improved real-time analysis. It can be suggested to put these temperature sensors as close to the heat exchangers as possible to reduce the measurement errors caused by heat losses between the water temperature at the inlet or outlet of the respective heat exchanger and the position, where the water temperature is measured. Another improvement would be to put as many temperature sensors as possible into immersive sleeves to further improve the precision of the temperature measurements. Since this would require major modifications to the refrigeration circuit of the heat pump, this step should be considered for future prototypes of the heat pump rather than for the current model.

Once the design conditions are reached, another suggestion would be to try to maintain steady-state operating points for a longer time span. In combination with monitoring the electrical power consumption of the compressor at shorter intervals, this would enhance the quality of the energy balances, thereby helping to identify potential sources of error

[29] Instead of a temperature spread of about 5 K, which was mostly tried during the measurements, a larger temperature difference of about, for instance, 15 K could help to ensure that the refrigerant leaves the condenser in a fully liquid state.

[30] The term "liquid line" describes the pipes between the condenser and the ejector's motive nozzle.

more clearly and allowing for more precise assessments of the heat pump's performance.

To conclude, to improve the performance of the industrial high-temperature heat pump and the ejector, further measurement campaigns are required, where the design conditions are reached. By ensuring complete condensation in the condenser, only liquid refrigerant will enter the three-way valve and the ejector, enabling better control of the suction gas superheating and an increased mass flow rate in the condensing circuit as well as a higher heating capacity of the heat pump.

Looking ahead, achieving these improvements and meeting the design conditions of the heat pump will pave the way for enhanced performance and a better understanding of this industrial high-temperature ejector heat pump. In the future, implementing ejectors into refrigerant circuits could contribute to more efficient and environmentally-friendly designs for the next generation of high-temperature heat pumps.

List of Figures

List of Tables

Acknowledgements

This research was conducted within the project *ETHP*, which was funded by the *Austrian Research Promotion Agency* (FFG) under grant no. 40165847 (program line Energieforschung 7. Ausschreibung, project Ejektortechnologien für Wärmepumpen).

During the course of this diploma thesis, *ChatGPT* was utilised as a tool for structural suggestions, translations and programming support (OpenAI, 2023).

References

Cordin Arpagaus. Hochtemperatur Wärmepumpen - Literaturstudie zum Stand der Technik, der Forschung, des Anwendungspotenzials und der Kältemittel. 2017.

Cordin Arpagaus and Stefan Bertsch. Experimenteller Vergleich von R1224yd(Z) und R1233zd(E) in einer Hochtemperatur-Wärmepumpe. Wissenschaft. Kältemittel, 2020. URL https://www.google.com/url?sa=t&rct=j&q=&esrc=s&source=web&cd=&ved=2ahUKEwi3nfHr-t6HAxW2IxAIHeZPALYQFnoECCIQAQ&url=https%3A%2F%2Fwaermepumpe-izw.de%2Fwp-content%2Fuploads%2F2020%2F05%2F200300-KI-s.-46-Exp.-Vergl.-R1224ydZ-u.-R1233zdE-HTWP.pdf&usg=AOvVaw35bos6SmwYCoZTzjwOQmHl&opi=89978449.

Ian H. Bell, Jorrit Wronski, Sylvain Quoilin, and Vincent Lemort. Pure and Pseudo-pure Fluid Thermophysical Property Evaluation and the Open-Source Thermophysical Property Library CoolProp. *Industrial & Engineering Chemistry Research*, 53(6):2498–2508, February 2014. ISSN 0888-5885. doi: 10.1021/ie4033999. URL https://doi.org/10.1021/ie4033999. Publisher: American Chemical Society.

Giorgio Besagni, Riccardo Mereu, and Fabio Inzoli. Ejector refrigeration: A comprehensive review. *Renewable and Sustainable Energy Reviews*, 53:373–407, January 2016. ISSN 1364-0321. doi: 10.1016/j.rser.2015.08.059. URL https://www.sciencedirect.com/science/article/pii/S1364032115009223.

Damien Bobelin, Dr Ali Bourig, and Jean-Louis Peureux. Experimental results of a newly developed very high temperature industrial heat pump (140°C) equipped with scroll compressors and working with a new blend refrigerant. 2012.

Energie Mobilität Innovation und Technologie (BMK) Bundesministerium für Klimaschutz, Umwelt. Energie in Österreich - Zahlen, Daten, Fakten. Technical report, Wien, 2022.

Jaroslav Chlubny. *Heat Pumps. Energy Saving and Renewable Energy in Vocational Education. ENERSOL EU project.* 2004.

Clayton Crowe, Donald Elger, Barbara Williams, and Johan Roberson. *Engineering Fluid Mechanics - 9th edition.* John Wiley & Sons, Inc., 2009. ISBN 13: 978-0470-25977-1.

Wolfgang Demtröder. *Experimentalphysik 1: Mechanik und Wärme.* Springer-Lehrbuch. Springer, Berlin, Heidelberg, 2015. ISBN 978-3-662-46414-4 978-3-662-46415-1. doi: 10.1007/978-3-662-46415-1. URL https://link.springer.com/10.1007/978-3-662-46415-1.

Stefan Elbel and Pega Hrnjak. Experimental validation of a prototype ejector designed to reduce throttling losses encountered in transcritical R744 system operation. *International Journal of Refrigeration*, 31(3):411–422, May 2008. ISSN 0140-7007. doi: 10.1016/j.ijrefrig.2007.07.013. URL https://www.sciencedirect.com/science/article/pii/S0140700707001508.

Stefan Elbel and Neal Lawrence. Review of recent developments in advanced ejector technology. *International Journal of Refrigeration*, 62:1–18, February 2016. ISSN 0140-7007. doi: 10.1016/j.ijrefrig.2015.10.031. URL https://www.sciencedirect.com/science/article/pii/S0140700715003266.

Gregor Erbach. European Climate Law - EU Legislation in Progress. 2021. URL https://www.europarl.europa.eu/RegData/etudes/BRIE/2020/649385/EPRS_BRI(2020)649385_EN.pdf.

ETHP. FFG, 2022. URL https://projekte.ffg.at/projekt/4174819.

Brian E. Faulkner and F. Marty Ytreberg. Understanding Bernoulli's principle through simulations. *American Journal of Physics*, 79(2):214–216, February 2011. ISSN 0002-9505. doi: 10.1119/1.3533216. URL https://doi.org/10.1119/1.3533216.

Thomas Fleckl, Veronika Wilk, and Michael Hartl. Effiziente Abwärmenutzung durch Hochtemperaturwärmepumpen in der Industrie, Energietag 2015, Temperaturdifferenzen als Energiequellen, Arbeitskreis Energie der Österreichischen Physikalischen Gesellschaft. 2015.

Norman H. Gay. Refrigerating system, December 1931. URL https://patents.google.com/patent/US1836318A/en.

Walter Grassi. *Heat Pumps. Fundamentals and Applications*. Green Energy and Technology. Springer International Publishing, Cham, 2018. ISBN 978-3-319-62198-2 978-3-319-62199-9. doi: 10.1007/978-3-319-62199-9. URL http://link.springer.com/10.1007/978-3-319-62199-9.

Jana Hanova and Hadi Dowlatabadi. Strategic GHG reduction through the use of ground source heat pump technology. *Environ. Res. Lett*, 2, October 2007. doi: 10.1088/1748-9326/2/4/044001.

Stephan Kling, Edith Haslinger, Michael Lauermann, Henk Witte, Christoph Reichl, Alexander Steurer, Constantin Dörr, Dragisa Pantelic, and Robin Friedrich. GeoFit: Experimental investigations and numerical validation of shallow spiral collectors as a basis for development of a design tool for geothermal retrofitting of existing buildings. 2022.

Masafumi Nakagawa, Ariel R. Marasigan, and Takanori Matsukawa. Experimental analysis on the effect of internal heat exchanger in transcritical CO2 refrigeration cycle with two-phase ejector. *International Journal of Refrigeration*, 34(7):1577–1586, November 2011. ISSN 0140-7007. doi: 10.1016/j.ijrefrig.2010.03.007. URL https://www.sciencedirect.com/science/article/pii/S0140700710000629.

Herbert Oertel. *Prandtl - Führer durch die Strömungslehre: Grundlagen und Phänomene*. Springer, Göttingen, Germany, 13 edition, 2012. ISBN 978-3-8348-2315-1. URL https://link.springer.com/book/10.1007/978-3-8348-2315-1.

OpenAI. ChatGPT (Nov 2023 to Aug 2024, version 4) [Large language model], 2023. URL https://chat.openai.com/chat.

Florian Reißner. Development of a Novel High Temperature Heat Pump System. 2015. URL https://open.fau.de/handle/openfau/6715.

René Rieberer, Gerald Zotter, David Hannl, Harald Moser, Oleksander Kotenko, Andreas Zottel, Thomas Fleckl, and Ivan Malenkovic. IEA Heat Pump Programme Annex 35: Anwendungsmöglichkeiten für industrielle Wärmepumpen. Nachhalt. Berichte aus Energie- und Umweltforsch. 2015.

Manuel Schieder. Characterization and Optimization of Ejectors using Numerical Fluid Dynamics. 2023. doi: reposiTUm.10.34726/hss.2023.108420.

Andreas Schröder. *Analyse einer industriellen CO2-Kälteanlage mit Ejektor*. PhD thesis, Fakultät für Maschinenbau der Technischen Universität Carolo-Wilhelmina zu Braunschweig, Cuxhaven, 2020.

Stuart J. Self, Bale V. Reddy, and Marc A. Rosen. Geothermal heat pump systems: Status review and comparison with other heating options. *Applied Energy*, 101:341–348, January 2013. ISSN 0306-2619. doi: 10.1016/j.apenergy.2012.01.048. URL https://www.sciencedirect.com/science/article/pii/S0306261912000542.

SRM-Technology. User and Maintenance Manual RS3. MUM006 rev. 01. 2021.

Peter Stephan, Karlheinz Schaber, Karl Stephan, and Franz Mayinger. *Thermodynamik: Grundlagen und technische Anwendungen Band 1: Einstoffsysteme*. Springer-Lehrbuch. Springer, Berlin, Heidelberg, 2013. ISBN 978-3-642-30097-4 978-3-642-30098-1. doi: 10.1007/978-3-642-30098-1. URL https://link.springer.com/10.1007/978-3-642-30098-1.

Appendix

The Appendix contains information regarding the design conditions of the heat pump, as well as the calibration data of the temperature sensors, an abstract for the annual meeting of the Austrian Physical Society (ÖPG) in Linz (Austria) for the Energy and Sustainability Committee and a brief overview of the project documentation at *AIT*.

A.1 Design Conditions

In Fig. 38, the simulated temperatures, pressures and mass flow rates in the refrigerant circuit at the simulated design conditions are shown.

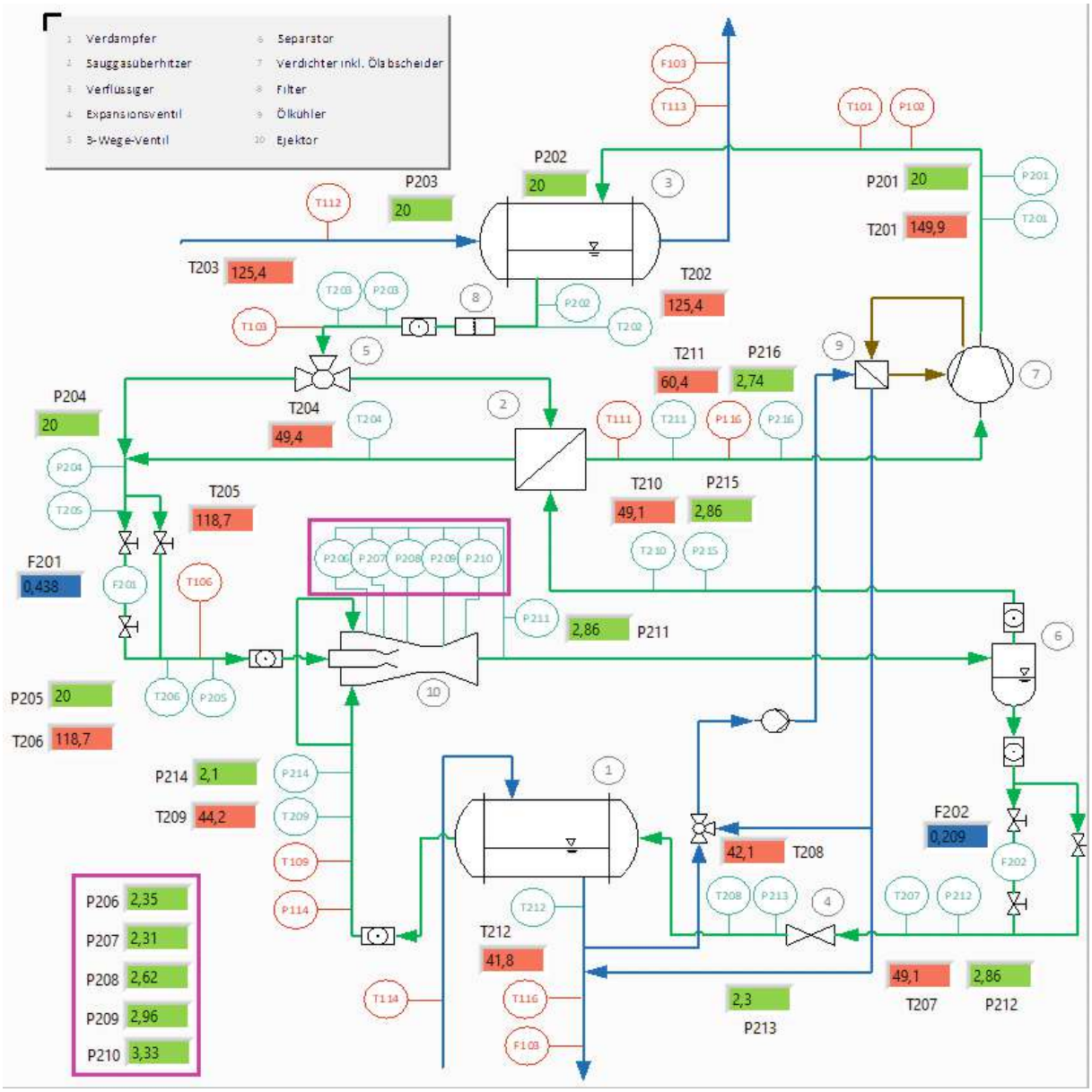

Figure 38: Design conditions of the heat pump. (Created by the author according to the simulation results of the *ETHP* research group.)

A.2 Temperature Sensor Calibration

The Appendix contains the calibration data of the temperature sensors (see subsection 3.3) and the calculated calibration coefficients. The *Jupyter Notebook* that was used to automatically find the stationary temperature values during the calibration process is presented in the project documentation at *AIT*.

Temperature sensor calibration for ETHP - March 2024 - 1/5

T201 - T2012 … sensors for measurements

BU1 - BU3 … backup sensors

calibration oven [°C]	T201		T202		T203	
	T_ref [°C]	T_meas [°C]	T_ref [°C]	T_meas [°C]	T_ref [°C]	T_meas [°C]
-10	-10	-9,94	-10	-9,81	-10,01	-9,95
-10	-10	-9,96	-10	-9,96	-10,01	-9,96
0	0	0,05	0	0,14	0	0,03
0	0	0,04	0	0,04	-0,01	0,03
10	10	10,08	10	10,14	10	10,06
10	9,99	10,07	9,99	10,07	9,99	10,05
20	20	20,07	20	20,11	20	20,04
20	19,99	20,07	19,99	20,07	19,99	20,04
30	30	30,09	30	30,11	30	30,06
30	29,99	30,09	29,99	30,09	29,99	30,06
40	40	40,08	40	40,08	40	40,04
40	39,99	40,07	39,99	40,07	40	40,03
50	50	50,08	50	50,06	50	50,02
50	49,99	50,07	49,99	50,07	50	50,02
60	60	60,07	60	60,03	60	60,02
60	59,99	60,07	59,99	60,07	60	60,01
70	70	70,04	70	69,98	70	69,98
70	69,99	70,04	69,99	70,04	70	69,98
80	79,99	80,05	79,99	79,96	80	79,97
80	79,99	80,04	79,99	80,04	80	79,97
90	89,99	90,02	89,99	89,92	90	89,94
90	89,98	90,02	89,98	90,02	90	89,95
100	100	100,01	100	99,9	100	99,9
100	99,99	100,01	99,99	100,01	99,99	99,93
110	110	109,96	110	109,85	110	109,88
110	109,99	109,98	109,99	109,98	109,99	109,89
120	120	119,94	120	119,81	120	119,86
120	119,98	119,94	119,98	119,94	120	119,85
130	130	129,92	130	129,79	130	129,81
130	129,98	129,94	129,98	129,94	129,99	129,83
140	140	139,91	140	139,73	140	139,77
140	139,99	139,9	139,99	139,9	139,99	139,78
150	149,98	149,87	149,98	149,87	150	149,74

calibration coefficients	**T201**	**T202**	**T203**
a2	**-0,00002**	**-0,00001**	**0,00002**
a1	**0,9989**	**1,0005**	**0,9998**
d	**-0,062**	**-0,1115**	**-0,0527**

Temperature sensor calibration for ETHP - March 2024 - 2/5

T201 - T2012 … sensors for measurements

BU1 - BU3 … backup sensors

calibration oven [°C]	T204		T205		T206	
	T_ref [°C]	T_meas [°C]	T_ref [°C]	T_meas [°C]	T_ref [°C]	T_meas [°C]
-10	-10,01	-9,81	-10,02	-9,94	-10,02	-9,94
-10	-10,01	-9,96	-10,01	-9,94	-10,01	-9,94
0	0	0,1	-0,02	0,03	-0,02	0,02
0	-0,01	0,03	-0,01	0,04	-0,01	0,04
10	10	10,07	9,98	10,03	9,98	10,02
10	9,99	10,05	9,99	10,07	9,99	10,07
20	20	20,02	19,98	20,02	19,98	20
20	19,99	20,04	19,99	20,05	19,99	20,05
30	30	30,01	29,98	30,03	29,98	30
30	29,99	30,06	29,99	30,06	29,99	30,06
40	40	39,96	39,98	40,01	39,98	39,97
40	40	40,03	39,99	40,04	39,99	40,04
50	50	49,92	49,98	50	49,98	49,95
50	50	50,02	50	50,02	50	50,02
60	60	59,89	59,98	59,98	59,98	59,93
60	60	60,01	59,99	60,01	59,99	60,01
70	70	69,83	69,98	69,94	69,98	69,89
70	70	69,98	69,99	69,97	69,99	69,97
80	80	79,79	79,98	79,93	79,98	79,87
80	80	79,97	79,99	79,96	79,99	79,96
90	90	89,74	89,99	89,9	89,99	89,84
90	90	89,95	89,99	89,92	89,99	89,92
100	100	99,72	99,97	99,87	99,97	99,82
100	99,99	99,93	99,99	99,9	99,99	99,9
110	110	109,68	109,96	109,82	109,96	109,77
110	109,99	109,89	109,98	109,85	109,98	109,85
120	120	119,63	119,96	119,78	119,96	119,73
120	120	119,85	119,98	119,81	119,98	119,81
130	130	129,61	129,95	129,76	129,95	129,7
130	129,99	129,83	129,98	129,79	129,98	129,79
140	140	139,55	139,95	139,71	139,95	139,66
140	139,99	139,78	139,97	139,73	139,97	139,73
150	150	149,74	149,96	149,68	149,96	149,68

calibration coefficients	**T204**	**T205**	**T206**
a2	**0,000003**	**0,00001**	**0,00001**
a1	**1,0024**	**1,0003**	**1,0008**
d	**-0,0926**	**-0,067**	**-0,0641**

Temperature sensor calibration for ETHP - March 2024 - 3/5

T201 - T2012 … sensors for measurements

BU1 - BU3 … backup sensors

calibration oven [°C]	T207		T208		T209	
	T_ref [°C]	T_meas [°C]	T_ref [°C]	T_meas [°C]	T_ref [°C]	T_meas [°C]
-10	-10,01	-9,97	-10,01	-9,86	-10,01	-10,03
-10	-10,01	-9,99	-10,01	-9,99	-9,99	-10,03
0	-0,02	-0,04	-0,02	0,01	-0,02	-0,06
0	0	0	0	0	0,01	-0,03
10	9,98	9,98	9,98	10,02	9,98	9,96
10	9,99	10,03	9,99	10,03	10	9,99
20	19,98	19,98	19,98	19,98	19,98	19,96
20	19,99	20,02	19,99	20,02	20	19,99
30	29,98	29,99	29,98	29,97	29,98	29,98
30	30	30,03	30	30,03	30	30
40	39,98	39,98	39,98	39,94	39,98	39,97
40	40	40,02	40	40,02	39,99	39,99
50	49,97	49,97	49,97	49,92	49,98	49,96
50	49,99	50,01	49,99	50,01	49,99	49,98
60	59,97	59,96	59,97	59,9	59,98	59,96
60	59,99	60	59,99	60	59,99	59,98
70	69,97	69,93	69,97	69,85	69,98	69,93
70	69,99	69,98	69,99	69,98	69,98	69,95
80	79,96	79,92	79,96	79,82	79,98	79,93
80	79,99	79,97	79,99	79,97	79,98	79,95
90	89,96	89,9	89,96	89,78	89,98	89,91
90	89,99	89,94	89,99	89,94	89,97	89,92
100	99,96	99,88	99,96	99,76	99,98	99,9
100	99,98	99,93	99,98	99,93	99,97	99,91
110	109,95	109,84	109,95	109,71	109,94	109,83
110	109,98	109,89	109,98	109,89	109,96	109,87
120	119,95	119,81	119,95	119,67	119,93	119,8
120	119,97	119,86	119,97	119,86	119,96	119,84
130	129,95	129,79	129,95	129,65	129,93	129,78
130	129,97	129,85	129,97	129,85	129,95	129,82
140	139,95	139,75	139,95	139,6	139,94	139,75
140	139,96	139,79	139,96	139,79	139,95	139,78
150	149,95	149,73	149,95	149,73	149,94	149,73

calibration coefficients	**T207**	**T208**	**T209**
a2	**0,00001**	**0,000006**	**0,00001**
a1	**0,9995**	**1,0012**	**0,999**
d	**-0,0153**	**-0,0495**	**0,0256**

Temperature sensor calibration for ETHP - March 2024 - 4/5

T201 - T2012 … sensors for measurements

BU1 - BU3 … backup sensors

calibration oven [°C]	T210		T211		T212	
	T_ref [°C]	T_meas [°C]	T_ref [°C]	T_meas [°C]	T_ref [°C]	T_meas [°C]
-10	-10,01	-9,86	-10	-9,9	-10	-9,82
-10	-9,99	-10,03	-10,03	-9,93	-10,03	-9,93
0	-0,02	0,11	-0,03	0,04	-0,03	0,07
0	0,01	-0,03	-0,02	0,09	-0,02	0,09
10	9,98	10,09	9,98	10,05	9,98	10,07
10	10	9,99	9,98	10,1	9,98	10,1
20	19,98	20,08	19,98	20,06	19,98	20,06
20	20	19,99	19,99	20,12	19,99	20,12
30	29,98	30,08	29,98	30,07	29,98	30,06
30	30	30	30	30,13	30	30,13
40	39,98	40,05	39,98	40,06	39,98	40,03
40	39,99	39,99	40	40,12	40	40,12
50	49,98	50,06	49,98	50,07	49,98	50,03
50	49,99	49,98	50	50,13	50	50,13
60	59,98	60,03	59,98	60,06	59,98	60
60	59,99	59,98	60	60,12	60	60,12
70	69,98	70	69,98	70,04	69,98	69,97
70	69,98	69,95	70	70,1	70	70,1
80	79,98	79,98	79,98	80,03	79,98	79,93
80	79,98	79,95	80	80,09	80	80,09
90	89,98	89,95	89,98	90	89,98	89,9
90	89,97	89,92	90	90,06	90	90,06
100	99,98	99,93	99,98	99,99	99,98	99,89
100	99,97	99,91	100	100,05	100	100,05
110	109,94	109,86	109,98	109,96	109,98	109,85
110	109,96	109,87	110	110,02	110	110,02
120	119,93	119,83	119,98	119,93	119,98	119,82
120	119,96	119,84	119,99	119,99	119,99	119,99
130	129,93	129,8	129,98	129,92	129,98	129,79
130	129,95	129,82	129,99	129,98	129,99	129,98
140	139,94	139,77	139,98	139,89	139,98	139,75
140	139,95	139,78	139,99	139,93	139,99	139,93
150	149,94	149,73	149,98	149,87	149,98	149,87

calibration coefficients	**T210**	**T211**	**T212**
a2	**0,00001**	**0,00001**	**0,000009**
a1	**0,9998**	**0,9993**	**1,0006**
d	**-0,0514**	**-0,0982**	**-0,1255**

Temperature sensor calibration for ETHP - March 2024 - 5/5

T201 - T2012 … sensors for measurements

BU1 - BU3 … backup sensors

calibration oven [°C]	BU1		BU2		BU3	
	T_ref [°C]	T_meas [°C]	T_ref [°C]	T_meas [°C]	T_ref [°C]	T_meas [°C]
-10	-10,02	-9,91	-10,02	-9,82	-10,03	-9,87
-10	-10,03	-9,94	-10,03	-9,94	-10,03	-9,95
0	-0,03	0,03	-0,03	0,1	-0,04	0,04
0	-0,02	0,07	-0,02	0,07	-0,02	0,06
10	9,97	10,07	9,97	10,1	9,97	10,08
10	9,98	10,1	9,98	10,1	9,99	10,09
20	19,98	20,06	19,98	20,09	19,97	20,1
20	19,99	20,1	19,99	20,1	19,99	20,09
30	29,98	30,09	29,98	30,11	29,98	30,12
30	30	30,12	30	30,12	30	30,12
40	39,99	40,08	39,99	40,09	39,98	40,12
40	40	40,1	40	40,1	40	40,11
50	49,99	50,07	49,99	50,07	49,99	50,12
50	50,01	50,11	50,01	50,11	50,01	50,13
60	59,99	60,07	59,99	60,05	59,99	60,13
60	60,01	60,1	60,01	60,1	60,01	60,13
70	69,99	70,04	69,99	70,02	69,99	70,11
70	70,01	70,08	70,01	70,08	70,01	70,1
80	79,99	80,04	79,99	80	80	80,11
80	80,01	80,08	80,01	80,08	80,01	80,11
90	89,99	90,01	89,99	89,98	90	90,08
90	90,01	90,06	90,01	90,06	90,01	90,09
100	99,99	100	99,99	99,96	100	100,06
100	100	100,05	100	100,05	100,01	100,08
110	110	109,98	110	109,93	109,99	110,03
110	110,01	110,01	110,01	110,01	110,01	110,06
120	119,99	119,94	119,99	119,9	119,99	120
120	120	119,98	120	119,98	120,01	120,06
130	129,99	129,92	129,99	129,88	130	129,98
130	130	129,97	130	129,97	130,01	130,05
140	140	139,89	140	139,85	140	139,94
140	140	139,93	140	139,93	140,01	140,02
150	150	149,87	150	149,87	150	149,92

calibration coefficients	**BU1**	**BU2**	**BU3**
a2	**0,00001**	**0,000009**	**0,00001**
a1	**0,9994**	**1,0004**	**0,9989**
d	**-0,0959**	**-0,1293**	**-0,1049**

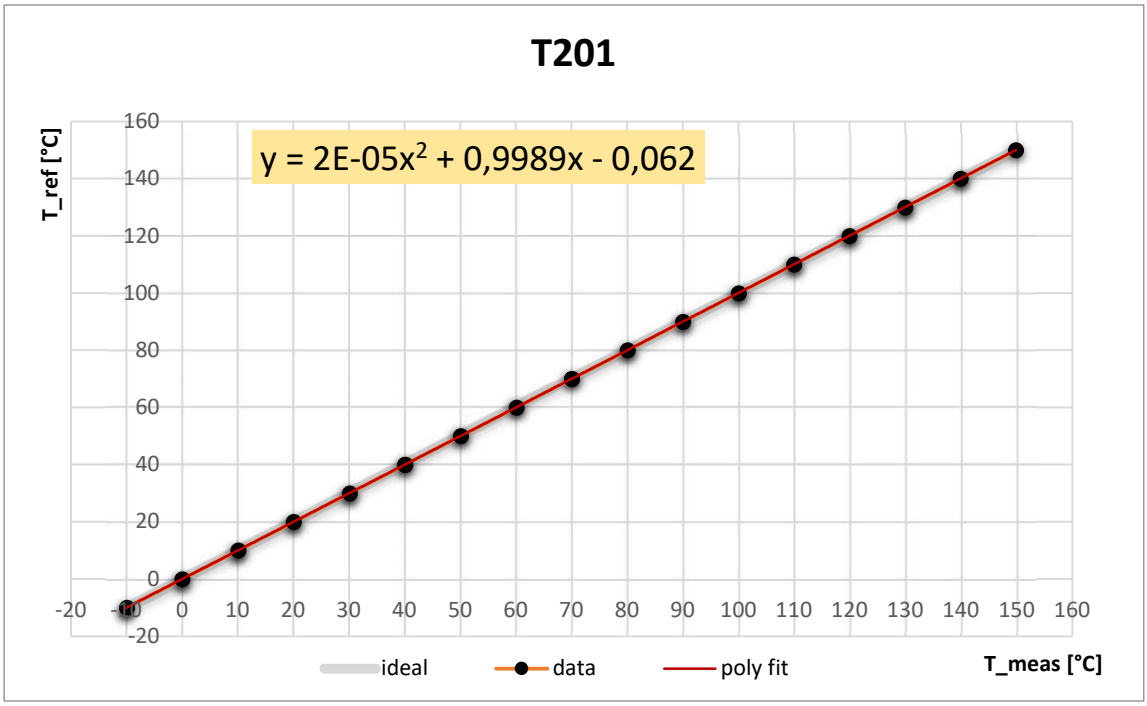

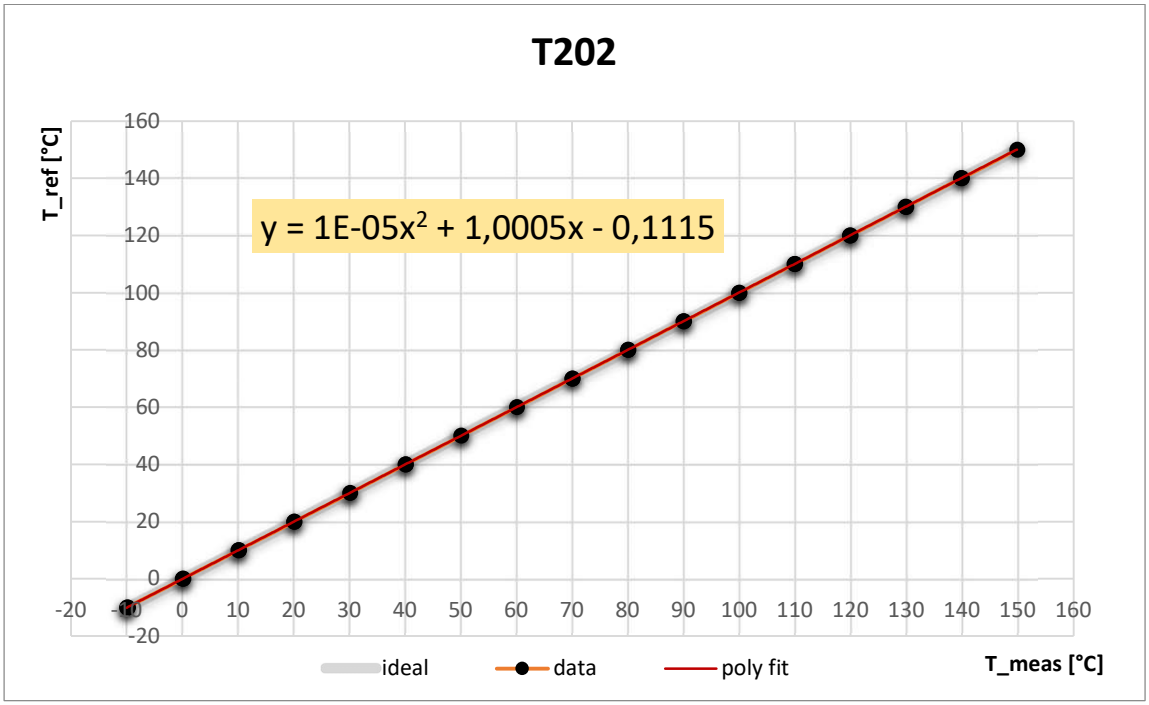

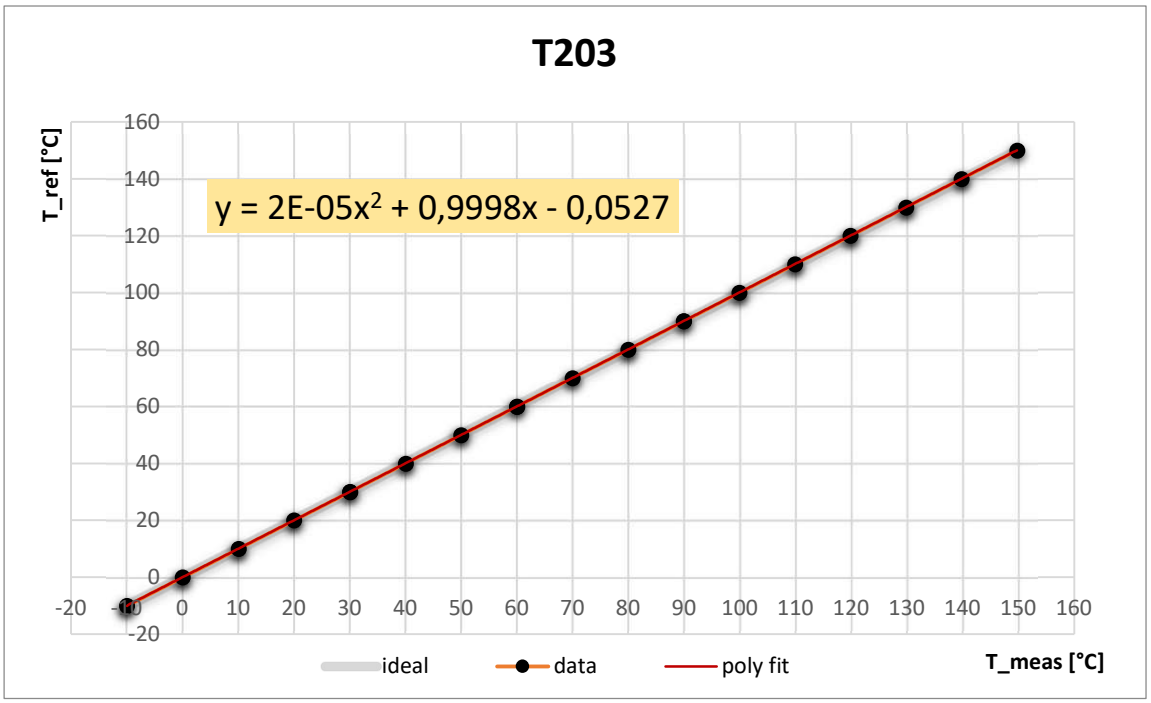

A.3 Abstract ÖPG

The abstract that was submitted to the annual meeting of the ÖPG in the field of Energy and Sustainability is also included in the Appendix.

OePG Division: ENS
Poster or Talk preferred: Talk

Design and Characterization of a High Temperature Heat Pump with Ejector

L. Stöger[1,2], M. Schieder[1], C. Illich[3], T. Königsecker[3], M. Mair[3], J. Unterluggauer[1], S. Kling[1], V. Sulzgruber[1], A. Stingeder[3], M. Lauermann[1], T. Ciepiela[3], C. Reichl[1, 4]

[1]*Sustainable Thermal Energy Systems, Center for Energy, AIT Austrian Institute of Technology, Wien, Austria*
[2]*Institute of Applied Physics, Technische Universität Wien, Austria*
[3]*OCHNSER Energietechnik GmbH, Haag, Austria*
[4]*Institute of Fluid Mechanics and Heat Transfer, Tecchnische Universität Wien, Austria*

Email Corresponding Author: christoph.reichl@ait.ac.at

Heat pumps offer a highly efficient alternative to fossil fuels like coal and gas by utilizing waste heat with minimal use of electricity. Industrial heat pumps are especially pertinent to the manufacturing sector. However, in the expansion valves used in traditional heat pumps an irreversible dissipation process occurs.

An innovative component inserted into the refrigeration circuit, the ejector, has the potential to decrease these losses significantly and improve the Coefficient of Performance of heat pumps by up to 26% in comparison to conventional systems.

An ejector normally is a passive component without moving parts consisting of three openings – the suction, motive and outlet nozzle: The high-pressure motive flow induces a suction flow from the low-pressure side, resulting in a higher pressure at the compressor inlet. This process reduces the electrical power required for compressor operation.

Within the FFG's research project “ETHP – Ejector Technologies for Heat Pumps”, an industrial high-temperature heat pump featuring an ejector was designed. The system was optimized for a source temperature of approximately 45°C and a sink temperature of around 130°C. Various ejector geometries were simulated and compared until an optimal ejector design with a variable inner geometry was identified.

The heat pump and ejector were manufactured and put into operation. Over 30 sensors were installed to gather measurement data on pressure, temperature gradients, and refrigerant mass flow at various points within the refrigerant circuit. The collected data were analyzed and visualized in real-time using LabVIEW, focusing particularly on the impact of the ejector. The data provide the foundation to validate the three-dimensional simulation models of the ejector.

A.4 Project Documentation at *AIT*

The project documentation contains information primarily relevant for *AIT* in regard to the next *ETHP* measurements. It is not included in this Appendix, but mentioned for the sake of completeness. The project documentation includes extracts from various data sheets as well as *Jupyter Notebooks*, which were used to analyse the measurement data.

Data Sheets

The following data sheets, or extracts from them, are listed in the project documentation at *AIT*:

- TR4TP-1001 temperature sensors (*SONTEC*),
- Cerabar PMC21 absolute pressure sensors (*Endress+Hauser*),
- micro-change (M12) connectors for the Cerabar PMC21 pressure sensors (*molex*),
- Deltabar M PMD55 differential pressure sensors (*Endress+Hauser*),
- mass flow meters Micro Motion F-Serie F050 (*Emerson*),
- I-7561 converter module and I-7017 and I-7033 modules (*ICP DAS*) and
- PTC-155 calibration oven (*JOFRA calibration AMETEK*).

Data Synchronisation

In the project documentation, the *Jupyter Notebook* is presented, which was used to synchronise the measurement data from *AIT* and *OCH* in regard to their respective starting time.

Data Analysis

Another *Jupyter Notebook* is shown in the project documentation, which was used to process the measurement data and create various charts and figures. For instance, pressure and temperature time series were plotted and pressure enthalpy diagrams calculated for specified times.